

VU Research Portal

Lensless imaging with high-harmonic sources

de Beurs, Anne Christiaan Cornelis

2023

DOI (link to publisher)
[10.5463/thesis.313](https://doi.org/10.5463/thesis.313)

document version
Publisher's PDF, also known as Version of record

[Link to publication in VU Research Portal](#)

citation for published version (APA)

de Beurs, A. C. C. (2023). *Lensless imaging with high-harmonic sources*. [PhD-Thesis - Research and graduation internal, Vrije Universiteit Amsterdam]. <https://doi.org/10.5463/thesis.313>

General rights

Copyright and moral rights for the publications made accessible in the public portal are retained by the authors and/or other copyright owners and it is a condition of accessing publications that users recognise and abide by the legal requirements associated with these rights.

- Users may download and print one copy of any publication from the public portal for the purpose of private study or research.
- You may not further distribute the material or use it for any profit-making activity or commercial gain
- You may freely distribute the URL identifying the publication in the public portal ?

Take down policy

If you believe that this document breaches copyright please contact us providing details, and we will remove access to the work immediately and investigate your claim.

E-mail address:
vuresearchportal.ub@vu.nl

VRIJE UNIVERSITEIT

LENLESS IMAGING WITH HIGH-HARMONIC SOURCES

ACADEMISCH PROEFSCHRIFT

ter verkrijging van de graad van Doctor of Philosophy
aan de Vrije Universiteit Amsterdam,
op gezag van de rector magnificus
prof.dr. J.J.G. Geurts,
in het openbaar te verdedigen
ten overstaan van de promotiecommissie
van de Faculteit der Bètawetenschappen
op donderdag 16 november 2023 om 11.45 uur
in een bijeenkomst van de universiteit,
De Boelelaan 1105

door

Anne Christiaan Cornelis de Beurs

geboren te Delft

promotoren:

dr. S.M. Witte
prof.dr. K.S.E. Eikema

promotiecommissie:

prof.dr.ir. E.J.G. Peterman
dr. L.V. Amitonova
dr. D. van Oosten
prof.dr. W.M.J. Coene
prof.dr. M.P. van Exter

The work described in this thesis was carried out at the Advanced Research Center for Nanolithography (ARCNL), a public-private partnership between the University of Amsterdam (UvA), the Vrije Universiteit Amsterdam (VU), the University of Groningen (RUG), the Netherlands Organisation for Scientific Research (NWO), and the semiconductor equipment manufacturer ASML. Funding for this research was provided by the European Research Council (ERC Starting Grant LENSLESS, 637476)

COLOPHON

Cover: A phaselocked pair of high-harmonic beams scatter from a sample and a diffraction pattern is recorded on a camera located in the far-field of the sample.

This thesis was printed by ridder print:

www.ridderprint.nl

CONTENTS

I	THESIS	1
1	INTRODUCTION	3
1.1	Imaging and microscopy	3
1.2	High-resolution imaging	3
1.2.1	Diffraction limit	3
1.2.2	Super-resolution imaging	4
1.2.3	Lens-based short-wavelength imaging	5
1.3	Coherent diffractive imaging	6
1.4	Comparison of short-wavelength sources	9
1.5	Multiplexed imaging	10
1.5.1	Phase-contrast imaging	10
1.5.2	Imaging spectrometry	11
1.5.3	Outline of thesis	12
2	ELECTROMAGNETIC WAVES AND DIFFRACTION	15
2.1	Scalar Diffraction theory	15
2.1.1	The scalar wave equation	15
2.1.2	Angular spectrum method (Fourier space representation)	16
2.1.3	Rayleigh-Sommerfeld theory (Real-space representation)	18
2.1.4	Fresnel and Fraunhofer approximations	18
2.1.5	Tilted plane diffraction	21
3	LENSLESS IMAGING	25
3.1	The Phase Problem	25
3.2	Single shot phase retrieval methods	25
3.2.1	Holography	25
3.2.2	Coherent Diffractive Imaging	27
3.2.3	Object priors in cCDI	28
3.2.4	cCDI Algorithms	29
3.3	ptychography	31
3.3.1	Solving the phase problem through transverse scanning	31
3.3.2	Wigner-distribution deconvolution method	33
3.3.3	Ptychographic CDI	33
3.3.4	PIE-type algorithms	34
3.3.5	Convergence acceleration through momentum acceleration in ptychography	38
3.4	Spectrally resolved imaging through Fourier-transform spectroscopy	40
3.4.1	Diffractive shear Interferometry	43
3.4.2	FTS-Fourier Holography	44

3.5	Coherence and sampling requirements in diffractive imaging	44
3.5.1	Sampling Requirements	44
3.5.2	Coherence requirements	46
4	EXTREME ULTRAVIOLET LASER SYSTEM AND IMAGING SETUPS	49
4.1	The high-harmonic generation process	49
4.1.1	Three-step model	49
4.1.2	Phase matching for HHG	52
4.2	Laser and amplification system	53
4.2.1	The Ti:Sa oscillator seed laser system	53
4.2.2	The Nd:YAG pump laser system	54
4.2.3	The non-collinear optical parametric chirped-pulse amplifier system (OPA)	59
4.2.4	Generating EUV pulse pairs through high-harmonic generation	63
4.3	Generating Extreme Ultra-Violet pulse pairs	64
4.3.1	Fourier-transform spectroscopy and infrared pulse pairs	64
4.4	EUV imaging setups	66
5	DIFFRACTIVE SHEAR INTERFEROMETRY	69
5.1	Abstract	69
5.2	Introduction	70
5.3	Spatial shearing interferometry of diffraction patterns	71
5.3.1	Interference of diffraction patterns	71
5.3.2	Image reconstruction	73
5.3.3	Comparison between DSI and single-beam CDI	74
5.4	Experimental demonstration of diffractive shear interferometry using high-harmonics	76
5.4.1	Fourier-transform holography	78
5.4.2	DSI reconstruction	79
5.4.3	DSI imaging of complex objects	80
5.5	Conclusions	81
6	ROTATIONAL DIFFRACTIVE SHEAR INTERFEROMETRY	83
6.1	Abstract	83
6.2	Introduction	84
6.3	Rotational Diffractive shearing interferometry	85
6.3.1	Diffractive Shearing interferometry	86
6.3.2	Rotational diffractive shearing interferometry	87
6.4	Numerical simulations of rotational DSI	88
6.5	Experimental demonstration of rotational DSI	90
6.5.1	Setup and measurement procedure for DSI with a HHG source	90
6.5.2	Measurement results and rotational DSI reconstructions	92
6.6	Conclusion	94

6.7	supplementary material	94
7	APIE: AN ANGLE CALIBRATION ALGORITHM FOR REFLECTION PTYCHOGRAPHY	97
7.1	Abstract	97
7.2	Introduction	98
7.3	Backward mapping vs Forward mapping	99
7.4	Algorithm	100
7.5	Discussion and Conclusion	104
	BIBLIOGRAPHY	107
II	APPENDIX	123
A	APPENDIX A	125
A.1	complex real calculus	125
B	SUPPLEMENTARY MATERIAL FOR CHAPTER 7 (APIE)	127
B.1	Derivation of the inverse Transformation	127
B.2	Ensuring numerical accuracy	129
B.3	Illustration of mapping procedures	130
B.4	Error convergence with and without tilt-angle refinement	131

SUMMARY

Coherent diffractive imaging (CDI) is a family of computational imaging techniques that uses iterative reconstruction algorithms to decipher the information encoded in one or more interference patterns to reconstruct a complex image of an object located in another propagation plane. The lensless nature of these techniques makes them well-suited for imaging with coherent extreme ultraviolet (EUV) or x-ray illumination as refractive optics are limited at these wavelengths. Imaging at such short wavelengths can enable imaging resolutions that can not be obtained by a conventional visible light microscope.

In particular, this work investigates the use of CDI techniques in combination with high-harmonic generation. High-harmonic generation (HHG) sources can generate EUV illumination beams with a high degree of spatial coherence in a compact tabletop setup. In the high-harmonic generation process, intense laser light is upconverted to photons with frequencies that are high harmonics of the frequency of the driving laser. As these sources produce very broad spectra, typically some form of spectral filtering is required to meet the temporal coherence requirements for CDI experiments. Such filtering processes are highly inefficient, leading to sub-optimal use of the available EUV radiation. In this work we use Fourier-Transform spectroscopy (FTS) to separate a set of nearly monochromatic diffraction patterns from a broadband HHG diffraction pattern. These monochromatic diffraction patterns can be used to reconstruct spectrally resolved images through reconstruction methods that are similar to those applied in conventional CDI. This approach has the added benefit of adding spectral resolution to diffractive imaging, so that it might be possible to identify spectral features in a sample's optical properties.

To generate these high-harmonic pulse pairs for FTS, we generate infrared pulses with 25 fs pulse duration, 10 mJ pulses with a central wavelength of approximately 800 nm. These driving laser pulses were generated with the noncollinear optical parametric chirped pulse amplifier system described in Chapter 4. These infrared pulses were subsequently converted into phase-locked pulse pairs using a common-path interferometer that is based on two pairs of birefringent wedges and a thin film polariser. This interferometer is described in detail in Sec. 4.3. Then, in order to obtain phase-locked harmonics, the resulting infrared driving laser pulses are focused at slightly separated locations in a noble gas jet to upconvert them into a pair of almost identical high-harmonic pulses.

In FTS-based imaging experiments, we illuminate a sample with the HHG pulse pairs and record the far-field diffraction pattern as a

function of pulse-to-pulse time delay. The spatial separation of our two harmonic beams results in spatial interference between two laterally sheared copies of the diffraction pattern. As a consequence of our two beam harmonic-generation geometry, the far-field electric field is formed by the interference between two laterally sheared copies of the field that would be generated in a single beam geometry. As a consequence, the spectrally separated diffraction patterns obtained in these measurements are similar, but not identical to the standard CDI case.

In Chapter. 5, we demonstrate an algorithm, called diffractive shear interferometry (DSI), to reconstruct images from such diffraction patterns, based on phase retrieval from the intensity information combined with an object support. As a single diffraction pattern alone does not contain sufficient information for a unique reconstruction, the DSI reconstruction algorithm attempts to find a complex electric field that satisfies a finite object support prior, while simultaneously satisfying the measurement data. This approach is similar to the approach used in most single-shot CDI experiments. Compared to CDI, the DSI measurement signal contains information about the phase derivatives in the direction of the shear at the cost of information about the amplitude of the single beam field. In simulations, we found that DSI image reconstruction would converge more robustly than traditional CDI measurement at comparable signal-to-noise-ratios. Using DSI, we were able to reconstruct images at 5 different wavelengths simultaneously. However, like single-shot CDI, unless the object is both finite size and has relatively well defined edges, the basic DSI method requires significant prior knowledge about the sample structure to sufficiently constrain the field solution to be unique, which can be limiting for some applications. In Chapter. 6 we demonstrate that it is possible to reconstruct complex images of a sample without using an finite support prior from a set of DSI measurements by scanning the relative orientation between the sample and the lateral shear between the beams instead. A single DSI measurement contains information about the phase derivatives of the single beam electric field on the detector and by rotating the shear with respect to the object, the phase derivatives in other direction become constrained as well. In this work it was demonstrated that this extra information can be sufficient to find a solution for the object without constraining the object size.

One of the advantages of coherent diffractive imaging techniques is that they reconstruct the full complex electric field at the sample. In reflection mode, such phase difference can be easily attributed to height differences of the reflecting surface. However, at research in diffractive imaging, including the work in the previously mentioned sections, has focused on transmission mode imaging. At the EUV wavelengths generated by HHG sources transmission coefficients tend

to be small. This limits applications of transmission mode imaging with HHG sources to thin layers. While normal incidence reflection coefficients are vanishingly small, towards grazing incidence the reflection coefficients approach one. This makes tilted-plane reflection mode imaging a particularly promising candidate to extend imaging with HHG beyond thin layers.

Such a geometry does come at a cost of added experimental and computational complexity. While far-field diffraction between colinear planes can be described by a straight forward Fourier transform of the electric field, for the propagation between non-collinear planes, an additional non-linear coordinate transformation is required. This coordinate transformation depends on the tilt angle of the fields and becomes very sensitive to the exact tilt-angle towards grazing incidence.

While CDI itself requires accurate knowledge of the wave propagation, a technique known as ptychography offers more flexibility. One of the main strengths of ptychography is the ability to solve for extra parameters other in addition to the complex sample and illumination beam due to the diverse information present in the measurement set. In Chapter. 7 we use that property to demonstrate an auto-calibration algorithm that can calibrate the tilt-angle during a ptychographic reconstruction. This algorithm adjusts the tilt-angle iteratively during reconstruction using an randomised search inspired by the Luus-Jakoola algorithm. Using this approach we were able to refine the tilt angle close to the correct value even when the initial estimates were off by more than 5 degrees, greatly improving flexibility in reflection-mode lensless imaging.

DANKWOORD

Tijdens mijn promotietraject zijn er een aantal mensen geweest zonder wie het niet was gelukt om dit proefschrift af te ronden. En zonder wie het ook een veel minder leuke tijd was geweest. Daarom wil ik hier een aantal van hen bedanken.

Als eerste wil ik mijn eerste promotor en begeleider bedanken. Stefan, ik heb echt mazzel gehad met jou als begeleider, weinig mensen hebben jouw optimisme en geduld. Dat zijn dingen die ik hard nodig heb gehad. Je was altijd duidelijk en to the point met je feedback. Maar je luisterde ook echt als ik dacht dat dingen anders zaten.

Dan mijn andere promotor. Kjeld, bedankt voor je advies en de gezelligheid, vooral toen ons lab zich nog op de vu bevond. Omdat Stefan zijn aanwezigheid moest verdelen tussen het lab aan de VU aan de ene kant en de labs op ARCNL aan de andere kant was het heel fijn dat we vaak op jou konden terugvallen voor advies met het lasersysteem. Bedankt dat je ons ook welkom liet voelen in jullie groep, ik heb zeer genoten van de koffiepauzes, conferenties, etentjes en dergelijke.

Then I would like to thank the colleagues that directly contributed to the work in this thesis.

Kevin, my lab-partner. You only started a couple of months after I started my thesis, so we have really gone through this PhD journey together. Almost any experiment I have done was in some way a co-operation with you, and as such most of my projects really have been a group effort. You solved so many problems on our experimental setup that would have been harder to solve if you hadn't been there. And you were always there to listen when I had to complain about personal stuff as well. Love you, man!

Matthijs, bedankt voor alles wat je me geleerd hebt toen ik als groentje aan dit project begon. Ik had tijdens mijn master wat ervaring hebben met het uitleinen van een kleine laser. Echter, dat bereidde me nog in het geheel niet voor om te kunnen werken met onze complex hoge harmonische generatie opstelling. Daarin heb je me ontiegelijk veel bijgebracht. We hebben je gemist nadat je na je promotie bent vertrokken, zowel in het lab als bij de spelletjesavonden.

Lars, I have alot to thank you for. Without your help the last paper in this thesis probably wouldn't have materialised. The fact that I managed to positively contribute in building your tiny house, as a person with two left hands, is something that I wear as a personal mark of pride. Your a great person to hang out with and a ridiculously smart scientist.

Maisie, not only do I owe you for setting up the laser setup for the infrared experiment, I also really appreciated the discussions we had if I had a conceptual problem or when I needed a second opinion on some idea, you were always very open to spending some time to help me out to think things through. Hope you are doing well and I would like to find some time to visit you and Randy in the United States sometime.

Realigning our complicated high harmonic generation setup after we moved it from the VU to ARCNL was no small task. A task that took significantly longer than anticipated. I would like to thank Patrick and Antonios for their help in getting the setup back and running after we moved the setup from the VU to ARCNL.

Then, I would like to thank the rest of the ARCNL group: Denis, Randy, Antonios, Jan, Zeudi, Alesandro, Lars Freisem, Tiago, Amelie, Aneta, Maxsym, and Matthijs (Velsink). Thank you for your help, advice and company. I loved hanging out and going out to get all sorts of food or play games with you guys, and have fond memories of the conferences we shared.

Ik wil onze technici bedanken, Rob Kortekaas aan de Vrije Universiteit en Nik Noest at ARCNL, het scheelt veel als je voor mechanische problemen de hulp kan inschakelen van iemand die dicht bij de groep of sectie staat.

During and after corona I frequently found myself feeling demotivated, and, especially during the writing of my thesis, there were a couple of people who's support was instrumental in helping me keep my motivation to finish the process of writing. Especially as days seemed to be blending together working on writing my thesis from home every day.

Daarin wil ik mijn ouders bedanken. Jullie boden mij altijd een warm nest waar ik naar terug kon keren tijdens het schrijven van mijn thesis, iets wat regelmatig nodig was om verder te komen. Ik heb het onvoorstelbaar goed getroffen met ouders die wat ik ook doe voor de volle honderd procent achter me staan. Ik houd onvoorstelbaar veel van jullie.

I would like to thank Charlaine. You're not only a great person to spend time with, organise Nerd Nite with, play board games or cycle with, and talk about or eat food with. But you have also spent a significant amount of time to help me with the planning of my thesis and let me use your office at the VU so that I didn't have to work from home. Whenever I have some problems or difficulties, you always spontaneously offer to help, you are amazing .

Kay en Tineke, jullie zijn fantastisch lieve vrienden en het betekent veel voor me dat jullie spontaan aanboden dat ik bij jullie thuis aan mijn thesis kon schrijven op een moment dat ik er op mijn kamer niets meer uit mijn handen kwam.

I would like to thank my other colleagues and friends at the VU: Maarten, Elmer, Laura, Ruud, Yuri, Julian, Meissa, Frank, Joël, Oleksiy, Andres, Maxime, Kees, Matthieu and Robert. For the skating sessions coffee breaks, board games nights, climbing sessions, spinning sessions, nights at 'het genootschap der geneugten', you'r all lovely people.

Christos, Vasco, Dirk, Ruslan for your company and the interesting discussions at journal club.

I would like to thank the rest of the Nerd Nite Crew: Ning, Sandrine, Stella, Huyen, Whitney, organising these with you was incredibly fun. Joost, voor de potten magic op afstand, zeker niet onbelangrijk toen ik tijdens corona een tijd lang bijna geen collega's of vrienden meer zag.

Jasper, voor de emotionele steun als het tegen zit in prive sfeer, je empathie is hardverwarmend. Peter, Gijs en Christiaan, voor de jarenlange trouwe vriendschap, Ik ken jullie al van het begin van mijn studie en jullie betekenen heel veel voor me.

Part I
THESIS

INTRODUCTION

1.1 IMAGING AND MICROSCOPY

Improvements in imaging technology have frequently been a driver of the advancement of scientific knowledge of the natural sciences. For example, the discoveries of bacteria, blood cells, and microbes by Antonie van Leeuwenhoek, were made possible by his skill in improving the quality and magnification of microscopes of that time. Pasteur was able to correlate bacteria with illnesses through the use of microscopes, which was vital to our knowledge of epidemiology. In addition, innovations in imaging techniques have seen various diagnostic applications in medicine [1, 2]. In industry, advanced imaging techniques can be used as inspection tools for sub-micron sized structures, such as those produced in the semiconductor industry [3, 4]. The main goal of this thesis is to extend capabilities for imaging with high-harmonic sources, which generate at wavelengths where the availability of high quality traditional optics is limited. To this end, we have investigated several potential extensions of coherent diffractive imaging (CDI) methods [5]. In CDI, images are reconstructed with information present in the diffraction patterns, which are generated by illuminating the sample with coherent light instead of using optics. The information in these diffraction patterns can often be decoded computationally through iterative optimisation algorithms based on knowledge of the propagation of coherent electric fields. In particular, our goal is to combine the high resolution and phase sensitivity offered by more conventional CDI methods with ways to obtain spectral resolution, despite the coherence requirements set by CDI. This would enable spectrally resolved imaging at wavelengths where such capabilities have traditionally been limited. In this chapter we will describe the challenges these imaging techniques might solve and the advantages and limitations of various alternative imaging methods.

1.2 HIGH-RESOLUTION IMAGING

1.2.1 *Diffraction limit*

The smallest possible feature that any conventional microscope can resolve is limited by a fundamental resolution limit. When a circular lens is used to image a point source to the smallest possible spot, its intensity profile will exhibit a pattern of bright and dark diffraction

rings, a phenomenon named Airy disks after George Biddell Airy [6], who found a theoretical explanation in 1835. If two of those point sources are spaced too closely, the disks in the focal plane will overlap, and it will become impossible to distinguish them. In general, the smallest separation between two point sources that can still be distinguished with a conventional microscope is determined by the so-called diffraction limit. This limit, which was formally derived as an interference effect by Ernst Karl Abbe [7] in 1873. This Abbe limit can be expressed as

$$\Delta_x = \frac{\lambda}{2NA}, \quad (1)$$

where Δ_x is the maximum achievable lateral resolution and $NA = n \sin(\theta)$ is the numerical aperture, which is determined by the half-angle of a cone of light imaged to a spot and the refractive index n of the imaging medium. While the NA of conventional visible light microscopes has steadily increased over the centuries, it is physically impossible for the focusing light cone to have a full angle that is larger than 180 degrees. Even when using immersive oils, which raise the refractive index of the imaging medium, and thus the NA, by around a factor of 1.5, the maximum resolution of conventional visible light microscopes are limited to about 170 nm.

1.2.2 Super-resolution imaging

A number of so-called super-resolution techniques have been developed to improve on this limit using light at optical wavelengths [8]. The most common of these can be split in two groups: Near-field techniques and super-localisation techniques. The first of these groups use the information contained in evanescent waves [9] such as wave-guided or total internal-reflection modes. These type of waves travel along interfaces and do not propagate perpendicular to the interface (instead they decay exponentially in the direction of the normal. As their phase does not propagate in the direction of the surface normal, these waves are not diffraction limited and contain high resolution information that is not present in propagating waves (see Sec. 2.1.2) for a more detailed explanation).

Super-localisation methods, such as PALM [10] and STORM [11], have been very successful in reaching resolutions beyond the NA of the imaging system, often reaching sub-single digit nanometer resolutions with illumination in the optical regime. In these techniques fluorescent point emitters are attached to a specimen. After these emitters are activated through photo-excitation, the fluorescent light is imaged into diffraction-limited spots onto a detector. A series of measurements is recorded in which only a fraction of the point emitters are active and localisation methods are used to attribute spots to

isolated point sources. The location of those point sources can be determined by finding the center of the diffraction-limited spot, which can be fitted with the accuracy of a fraction of the diffraction limit. A point-wise high resolution image is subsequently build up through a series of measurements in which different emitters are switched on or off. While these techniques have been highly successful for various applications in biological imaging, they can be time intensive and require chemical staining of specimen with point emitters that bind to the specimen, something that is not possible for many other applications.

1.2.3 *Lens-based short-wavelength imaging*

As the diffraction limit (Eq. 1) scales with the wavelength, shorter-wavelength illumination offers an alternative path to improve beyond the resolution offered by conventional imaging microscopes. In addition to enabling higher imaging resolution compared to optical microscopes, x-rays have the additional benefit of deeper penetration into samples that are opaque in the visible. For this reason, x-ray microscopes are highly suitable for transmission imaging of thick samples at the cost of the amplitude-contrast of images. Since both the real and the imaginary part of refractive indices are close to unity for large parts of the extreme ultra-violet (EUV) and x-ray regimes [12], there is a lack of high NA refractive focusing optics. Fresnel zone plates are commonly used as alternatives to refractive lenses. These grating-like structures are designed to create a focus located at one of their first diffraction orders [13]. The relationship between the field at the zone plate and the field at one of its Fresnel diffraction planes can be described by a Fourier transform (see Ch. 2). Therefore, the smallest possible focal spot in the imaging plane is determined by the width of the illuminated part of the zone plate (as it determines its band-limit). However, binary absorption-based zone plates have very limited efficiency, as only the +1st diffraction order is focused and half of the intensity is absorbed in the grating structure, the theoretical maximum on the efficiency is limited to 10%. It is possible to improve on these numbers through the use of asymmetric, phase-modulating structure profiles that suppress one of the first orders. By making use of blazed gratings, focusing efficiencies of more than 50% have been reported with 0.2 nm light [14]. For any zone plate design, the size of the zone plate is limited by the smallest features that are possible to fabricate and due to the increased complexity of these high efficiency zone plates, their NA is typically $\ll 1$. However, due to their shorter wavelengths these microscopes still offer a large resolution improvement on conventional microscopes, while hard x-ray microscopes can offer better resolution than our methods can achieve with EUV illumination. Sub-100 nm resolutions have been reported with full field x-ray

transmission, using soft X-rays from lab-scale plasma sources [15, 16]. Scanning transmission x-ray microscopes (STXM) [17] create an image through point-scanning of an object in the focal plane of a zone plate, while recording the intensity at a scan position. The resolution of the images generated with these methods is limited by the spot size of the illumination. As advantage when compared to the full field method described above, these methods only require a single zone plate, as opposed to a combination of both a condenser and an imaging lens. In addition, the combination of a point scanning imaging formation process that is not sensitive to the spatial distribution on the detector enables a straightforward way to record spatially resolved fluorescent signal excited by the illumination beam, this additional chemical specificity can be highly beneficial to applications in material science. However, as a trade-off these methods require dense point scanning, depending on the desired resolution. As a result, depending on the field of view, measurement times are typically orders of magnitudes larger, and its resolution is likewise limited by the diffraction-limited spot size of the focusing optics.

1.3 COHERENT DIFFRACTIVE IMAGING

The main subject of study in this thesis are coherent diffractive imaging (CDI) methods [5, 18]. This is a group of computational imaging techniques that try to reconstruct the so-called 'exit wave', which is the complex wave scattering from a sample, from one or more diffraction patterns, by solving the inverse scattering problem through iterative optimisation. As focusing elements are not used for image formation, these techniques can avoid the resolution degradation induced by poor optics, which makes them especially appealing in imaging fields where quality lenses are not available. The NA of such imaging systems is determined by the largest scattering angle θ_s between rays of light that are collected on the camera, as illustrated in Fig. 1.

CDI of non-periodic samples is usually subdivided into two main groups of methods: In the first group, which we will refer to as conventional CDI (cCDI), the so-called 'exit wave', which is the field scattering from a sample, is reconstructed from a single diffraction pattern. These methods extract the phase information that is encoded in an over-sampled diffraction pattern through iterative algorithms [19], finding a solution that satisfies both the measurement and one or more constraints on the object. In particular, Fienup's hybrid-input output algorithm [20] has been highly successful in reconstructing real objects, illuminated with plane-wave illumination. However, in the case of complex objects strong prior knowledge of the specimen structure is typically necessary for successful image reconstruction in cCDI.

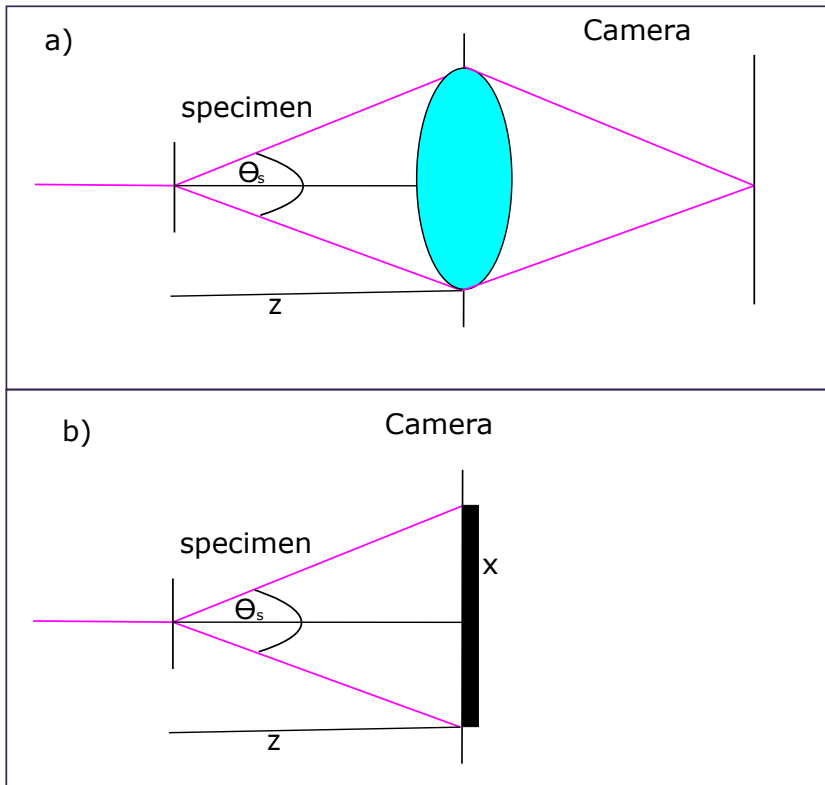


Figure 1: Illustration to explain the NA of a CDI imaging system by comparison to a simple conventional imaging system. a) The resolution of a perfect lens based imaging system is determined by the largest scattering angle that can be collected by its collector lens. b) In the case of CDI, if the field on the camera can be perfectly reconstructed, the information content (and thus the resolution) is identical as if the same light was collected by a lens with the same aperture as the camera and imaged through a perfect imaging system. Thus the highest NA that can be achieved is determined by the light with the largest scattering angle θ_s that can be detected on the camera, as opposed to the largest scattering angle θ_s that collected by the lens and reimaged without loss of information.

The issues with the reconstruction of complex objects have led to the development of ptychographic CDI (pCDI) by Rodenburg in 2004 [21]. In pCDI, a series of diffraction plane intensity images is captured on a camera. By scanning the transverse position of the sample (or less commonly the illumination with respect to the object), the area of the object that is illuminated by a confined illumination beam is changed at each camera exposure. If the overlap in area between different scan positions is sufficient, a data set is generated that is rich in 'diverse' information, relaxing the need in cCDI for strong object priors to constrain the problem. This information is one of the biggest features of ptychography as it makes it possible to solve for more variables than just the 2D exit wave, as the inverse problem for standard ptychography is highly overconstrained. Almost all modern ptychography algorithms are able to reconstruct the complex specimen image and complex illumination function separately, following the approach of the extended ptychographic iterative engine algorithm [22]. Not only does this decouple the specimen image quality from spherical aberrations in the illumination function, this also enables the use of ptychography as a wavefront sensing tool with a resolution that matches its imaging resolution, which was recently demonstrated in our group [23]. In addition to solving for the complex illumination and object functions, recent ptychographic algorithms have shown to be able to simultaneously solve for a stack of 2D object layers [24, 25], to deal with partial coherence by solving for mutually incoherent spatial illumination modes [26, 27], or to solve for different spectral components [28, 29] and various other experimental parameters. In transmission electron microscopy, a near-diffraction-limited resolution of 0.39 Å has been demonstrated. This is a significant improvement compared the resolution currently obtainable with aberration-corrected conventional microscopes [30].

Fourier-ptychography [31] is a related lens-based technique that records a series of images using a low-NA, wide field-of-view, while scanning the angular spectrum sampled by the lens is scanned by changing the illumination angle. These methods have shown high NA and very wide field-of-view simultaneously.

While the advantages of ptychography over conventional CDI outweigh the disadvantages for most applications if acquisition time and exposure times are not limiting factors, traditional CDI methods are still a common technique for applications where these factors are limiting such as the x-ray or electron imaging of degradable biological structures [18].

Different types of coherent diffractive imaging techniques have seen applications in various fields of microscopy where the use of optics have traditionally been limited, such as electron and x-ray imaging [27, 30]. Or in imaging with optical or terahertz illumination [32],

for the phase contrast that these methods offer at wavelengths where many materials are transparent.

Related computational methods have also found widespread applications in the fields of near infrared and radio astronomy. While the waves measured by these telescopes are incoherent, interferometric methods can be applied in order to obtain a signal that is the spatial Fourier spectrum of the celestial object, which is identical to relationship that exist between the far-field intensity pattern and an object in coherent imaging. In fact, the first practical iterative phase retrieval algorithms, applicable to the far-field CDI imaging problem were developed by Fienup for radio astronomy [20, 33]. Recently, such methods were used successfully to reconstruct an image of a black hole with the event horizon telescope [34, 35].

1.4 COMPARISON OF SHORT-WAVELENGTH SOURCES

Most photon-based CDI experiments so far have been performed using large scale x-ray facilities, such as synchrotrons [26, 36] or free electron lasers [37, 38]. Such facilities offer very high photon flux at very short wavelengths, and wavelength tunability through monochromators. While the light produced from synchrotrons does not satisfy the stringent coherence requirements of CDI, due to the very high brightness of these sources it is feasible to make use of spatial and spectral filtering to generate beams that have coherence properties that are sufficient for diffractive imaging, especially when combined with algorithms that model the source as a sum of incoherent modes [26, 27]. The high brightness these sources provide can enable sufficiently low single-acquisition exposure times to combine diffractive imaging methods with tomographic methods to produce nanoscale resolution 3D images of various objects [39]. Such methods have been used to image complex structures such as computer chips [40], as shown in Fig. 2. However, these facilities are expensive to operate and access, thus measurement time is typically limited. Furthermore, these measurements usually have to be planned and approved months in advance, in strong contrast with how microscopes are typically used for most applications. In recent years, high-harmonic generation (HHG) has shown to be a promising lab-scale alternative to these large-facility sources [41–43]. In such a source, photons from a high intensity driving laser are up-converted inside a medium into a broad spectrum of harmonics of the fundamental frequency through the highly non-linear processes described in Sec. 4.1. Wavelengths produced by these sources can range from photons in the ultra-violet regime to soft x-rays with cut-off frequencies in the water window [44].

While these sources are low in flux (typical energy-conversion efficiencies with infrared driving lasers range from 10^{-5} to 10^{-8} for gen-

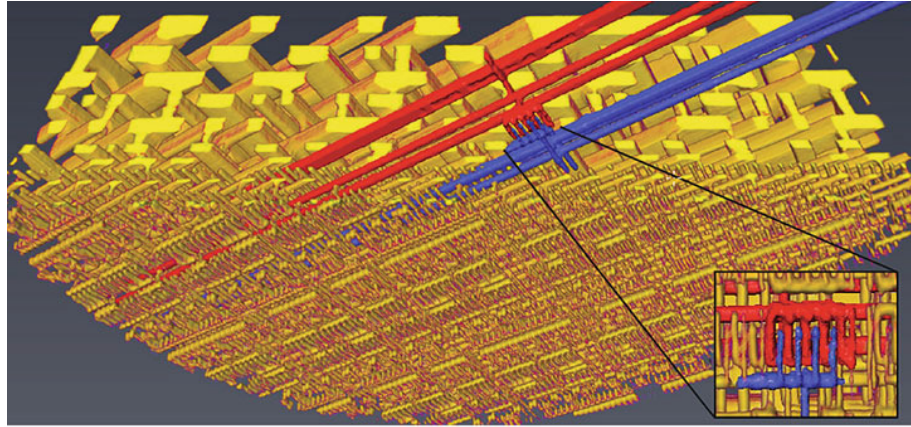


Figure 2: Ptycho-tomographic reconstruction of an Intel microprocessor, taken from Holler et al. [40]. Authors achieved a resolution of 14.6 nm in all directions.

eration in noble gases [45]), they have the excellent intrinsic spatial coherence properties needed for coherent diffractive imaging. Coherent diffractive imaging experiments with high harmonics frequently achieve a resolution in the order of the illumination wavelength, and in recent years resolutions down to 12 nm have been reported [46, 47].

1.5 MULTIPLEXED IMAGING

At its core, imaging techniques are tools to obtain information about the spatial distribution of a specimen. For a conventional imaging system with a detection scheme that is insensitive to wavelength, this information is limited to the wavelength-averaged, depth-integrated absorption or reflection coefficients of the sample. While this information is sufficient for many applications, it can be beneficial to obtain signals that contain different types of spatially-resolved information, especially if more than one signal can be obtained simultaneously.

1.5.1 Phase-contrast imaging

As a wave phenomenon, light is characterised by both amplitude and phase. Like its amplitude profile, the spatial phase profile of scattered light contains structural information of the scattering object. Light waves propagating through different parts of a specimen experience varying amounts of phase delay depending on the refractive index distribution of the traversed material. Furthermore, imaging phase distributions offer a way to resolve structures that offer no absorption contrast. A significant breakthrough in the field of phase sensitive imaging occurred in 1935, when Frits Zernike invented the phase-contrast microscope [48] as a way to image tiny refractive in-

dex variations in transparent samples. These microscopes image both the unscattered and the diffracted light from the specimen plane to an image plane. However, the geometry of these phase-contrast microscopes is set up in a way that induces a $\frac{\pi}{2}$ radian relative phase shift between the scattered and the non-scattered light before they arrive at the image plane. After attenuation, the unscattered light interferes destructively (for a positive phase contrast microscope) with the diffracted light at the image plane. As these two fields cancel almost entirely, small variations in phase can be visible as significant amplitude variations in the image plane. Since their invention, these types of microscopes have been a commonly used tool in biology [49]. While these microscopes offer a contrast mechanism that can detect even small phase curvatures, they are not suitable for more quantitative phase reconstructions as they suffer from inherent imaging artefacts. For example, as low-spatial frequency components of the scattered field tend to follow the same delay path as they unscattered field, their phase is not reconstructed, which results in amplitude halos at the edge of slowly varying features in the image. Another big step forward in the application of phase to imaging was made in 1948, when Gabor [50] discovered holography. In holographic imaging methods the interferometric signal of a scattered field with a known reference wavefront is measured on a photographic plate or camera. The phase difference between the scattered and the reference field is encoded in their interferometric cross-terms, which can be isolated from the recorded signal to measure the phase through various read-out mechanisms, some of which are described in Sec. 3.2.1. The main advantage of holographic methods compared to the phase-contrast microscope is that the phase reconstruction is quantitative.

The CDI-like methods explored in this thesis can solve for the full electric field at the specimen plane, therefore they offer many of the same phase-contrast benefits offered by the methods described above. Compared to holography, CDI imaging methods have less complex optics and alignment challenges due to either the difficulty of isolating the cross-terms for on-axis holography or the experimental complications that are associated with the requirement of a well-known reference wavefront for off-axis holography, at the cost of more computational complexity, and in the case of pCDI longer acquisition times.

1.5.2 *Imaging spectrometry*

Spectral resolution offers an additional channel to add information to imaging modalities. Such information can be used in various imaging applications to distinguish the scattering contribution of different chemical components. For example, spectrally resolved imaging techniques have been in use at optical and infrared wavelengths for appli-

cations such as earth remote sensing, where it is used to distinguish vegetation as well as different mineral components and environmental monitoring [51, 52]. In medical diagnostic applications such measurements can be used to delineate healthy tissue from cancer tissue [53]. In astronomy it is used to detect spatially resolved chemical abundances to understand evolutionary processes in stars and galaxy formations [54, 55]. In x-ray imaging experiments, K, L and M absorption edges are used to enhance chemical contrast. At those wavelengths spectrally resolved imaging can be achieved in various ways such as tunable monochromators [56], or specialized detectors that can measure single x-ray photon energies [57]. However, such capabilities have been lacking for imaging with high-harmonic sources. Spectrally resolved imaging detectors such as those that are used in the x-ray regime are currently not yet available, and using tunable monochromators can lead to impractically long measurement times due to the low flux of these sources.

In some cases it is possible to use the diverse information present in data sets used in ptychographic CDI to solve for the spectral weights of different spectral components with multiplexed ptychography [28]. While these methods have been used to solve for broadband high harmonic spectra [29, 58], it is typically only possible to reconstruct the different spectral components in specific conditions: 1) spectra that are well described with a limited number of narrow peaks (which holds for lower order harmonics, but is less applicable to higher harmonic orders), with considerable additional prior information about spectral components and/or very strong object priors. In the work of Ch. 5 and 6 we have investigated an alternative method that combines Fourier-transform spectroscopy (FTS) [59] with diffractive imaging methods, which in principle should be able to resolve even very broad harmonic spectra. It turns out that these methods bear a strong conceptual similarity to a group of techniques in astronomy, which is called double Fourier interferometry [60], in which the stellar signal of different baseline telescopes is interfered through FTS interferometry to build a spectrally resolved Fourier-plane signal of the object.

1.5.3 *Outline of thesis*

In the work underlying this thesis several methods were investigated to further extend lensless imaging with high harmonic sources. The main part of this work is described in chapters 5-7, which are based on published papers that were the result of these investigations. Chapters 2-4 are intended to give more context and explanation to the methods and experimental setups in these experiments. In Ch. 2, scalar diffraction theory is discussed, which describes the propagation of coherent light through free space. In particular, Sec. 2.1 discusses how quantitative relations for the propagation between paral-

lel planes can be obtained, which forms the basis for most conventional CDI algorithms. In Sec. 2.1.5, the theory of propagation between non parallel planes is considered, which is used as a basis for our tilt-plane ptychography algorithm in Ch. 7.

Then, in Ch. 3, an overview is given of the working principles of difference types of lensless imaging. First the phase problem is introduced in Sec. 3.1. Then in Sec. 3.2 a number of methods and algorithms are discussed that reconstruct the electric field at the detector from a single diffraction pattern, for these methods either significant object priors or reference waves are required. Next, in Sec. 3.3, ptychographic methods are discussed. In Sec. 3.4, the working principles of the DSI algorithms used in our EUV experiments is explained. Then, in Sec. 3.5 the sampling and coherence requirements in CDI-like methods are discussed.

Chapter 4, describes the experimental setups for the EUV DSI experiments. First, in Sec. 4.1, it is briefly explained how HHG can be understood in a simplified semi-classical picture, in which the interaction of the driving field with the medium is described classically after a tunnel-ionisation event. This is followed by a description of the infrared driving laser system used to generate harmonics in our EUV experiments in Sec. 4.2. Then, an experimental description is given of the interferometry setup used to generate infrared pulse pairs from this driving laser and the HHG generation setup that is used to up-convert these infrared pulses to phase-locked high harmonic pulse pairs Sec. 4.3.

The experimental work in this thesis can be subdivided in two computational imaging approaches: 1) Diffractive shear interferometry, which is a method we have developed to combine the spectral resolving power of Fourier-transform spectroscopy with the lensless imaging qualities of coherent diffractive imaging methods to enable hyperspectral diffractive imaging. This method is the basis of the articles described in Ch. 5, in which strong object priors are used to solve the inverse scattering problem and Ch. 6, in which the sample is rotated through an asymmetric illumination profile in order to obtain a more diverse data set, constraining the inverse problem to an extent that a finite object support is unnecessary. Both of these experiments were preformed with the high-harmonic generation setup described in Ch. 4. 2) In the work described in Ch. 7, we have developed a new image reconstruction algorithm for ptychographic CDI, that can calibrate the tiltangle for ptychography in a tilted-plane reflection geometry.

2.1 SCALAR DIFFRACTION THEORY

The computational imaging methods described in this work require a direct quantitative link between the electric field at the imaged specimen and the field at the detector. In the first part of this chapter, it is described how this link can be obtained from scalar diffraction theory.

2.1.1 *The scalar wave equation*

In the absence of charged particles, the electric-field component $E(\mathbf{r}, t)$ of monochromatic light, with an optical frequency ν , that is traveling through a linear, homogeneous, and isotropic medium can be described as a scalar wave,

$$E(\mathbf{r}, t) = \mathbb{R} (E(\mathbf{r}) \exp[-2i\pi\nu t]), \quad (2)$$

where $E(\mathbf{r})$ (apart from a spatially invariant phase-factor) is the instantaneous field at $t = 0$ and satisfies the scalar wave equation, which is given by

$$\nabla^2 E(\mathbf{r}, t) - \frac{n^2}{c^2} \frac{\partial^2 E(\mathbf{r})}{\partial t^2} = 0. \quad (3)$$

Where, n is the refractive index. It follows from applying the wave equation on Eq. 2 that the field $E(\mathbf{r})$ needs to satisfy the Helmholtz equation, which is given by,

$$\nabla^2 E(\mathbf{r}) + k^2 E(\mathbf{r}, t) = 0, \quad (4)$$

where $k = 2\pi\nu \frac{n}{c}$, is the wavenumber of the optical wave.

There are two common approaches for finding a solution for Eq. 4 in the case of free space propagation.

The first approach, which was developed by Kirchhoff [61] and Sommerfeld [62], makes use of Green's functions to derive a real-space representation of wave propagation from a 2D aperture to a point behind the aperture.

In the second approach, the angular spectrum method (ASM), the field in a plane is effectively described as collection of planewaves propagating in different directions from one plane to a parallel plane. This approach treats the propagation of the field in terms of its 2D Fourier components.

In the next section, we will follow the angular spectrum method to derive diffraction integrals, as the derivation is less mathematically involved compared to the derivation with Green's functions (and both methods have been shown to produce identical results [63]).

2.1.2 Angular spectrum method (Fourier space representation)

In the angular spectrum method, the instantaneous electric field $E(\mathbf{r})$ is expanded over two orthogonal directions x and y to obtain a 2D Fourier spectrum:

$$E(x, y, z) = \iint_{-\infty}^{\infty} \hat{E}(k_x, k_y, z) e^{i(k_x x + k_y y)} dk_x dk_y. \quad (5)$$

This expansion can simplify calculations if the Fourier components of the field at an area of interest (such as the surface of a detector) in some target plane can be accurately described with only a limited amount of spatial frequency components in the source plane. This is the case when either the spatial frequency spectrum at the source plane is band-limited (which suggests a smooth real-space field distribution) or if only a limited number of spatial frequency components reach the area of interest at the target plane (which suggests that this area of interest only collects a small range of scattering angles). If this expression is inserted into the Helmholtz equation, the problem of finding a solution for the electric field distribution can be simplified to solving the following differential equation in z :

$$(k^2 - k_x^2 - k_y^2)E(k_x, k_y, z) + \frac{\partial^2 E(k_x, k_y, z)}{\partial z^2} = 0, \quad (6)$$

for which we can find a wave-like solution of the form:

$$\hat{E}(k_x, k_y, z) = \hat{E}(k_x, k_y, 0) \hat{H}(k_x, k_y, z), \quad (7)$$

where,

$$\hat{H}(k_x, k_y, z) = e^{\pm i k_z z}, \quad (8)$$

which is known as the propagator in reciprocal space or the optical transfer function (OTF) in real space, and $k_z = \sqrt{k^2 - k_y^2 - k_x^2}$. For high transverse spatial frequency components $k_y^2 + k_x^2 > k^2$, k_z will be imaginary, in which case the multiplicative factor is a real negative exponential function of z . After propagation over macroscopic distances, these components will have decayed to a point that they can be neglected. Thus the information about the fastest varying features in the source plane is spatially low-pass filtered to $\sqrt{k_x^2 + k_y^2} < k = \frac{2\pi}{\lambda}$ while propagating to the target plane.

If equation Eq. 8 is inserted into Eq. 5 and solutions propagating in the positive z direction are considered, we obtain the following expression for the time-dependent field at a plane at a distance z :

$$E(x, y, z, t) = \iint_{-\infty}^{\infty} \hat{E}(k_x, k_y, 0) e^{i(\mathbf{k} \cdot \mathbf{r} - 2\pi\nu t)} dk_x dk_y. \quad (9)$$

Instead of as a Fourier decomposition, this expression can also be interpreted as a superposition of plane waves propagating in real space at different angles with wavevector $\mathbf{k} = (k_x, k_y, k_z)$. This is illustrated in Fig. 3.

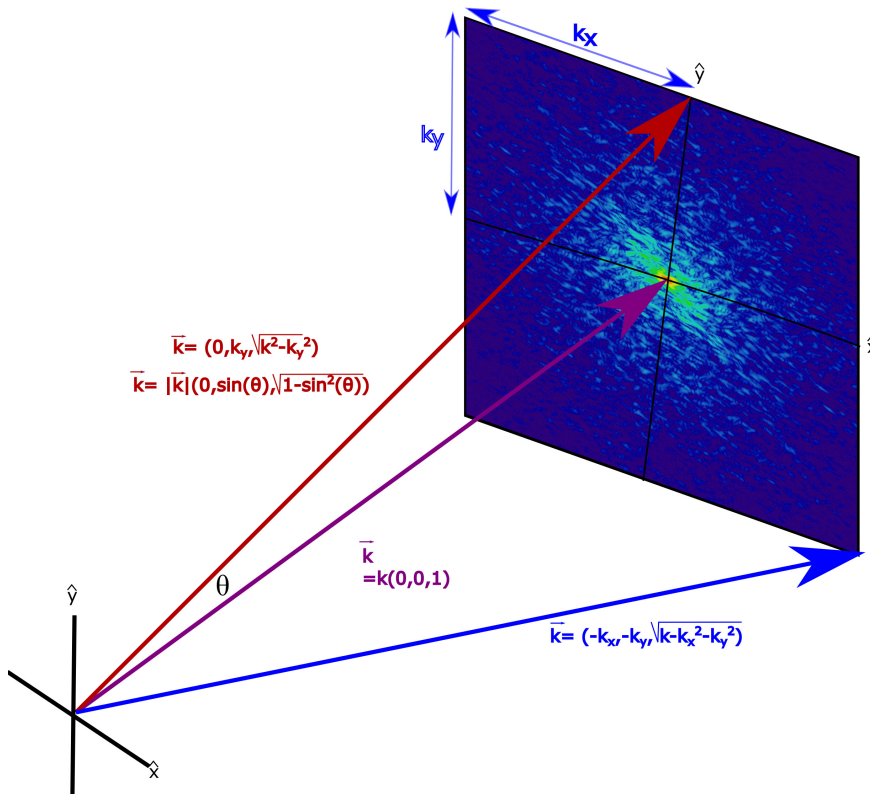


Figure 3: Illustration of propagation of spatial frequency components. The purple vector shows the propagation direction of a component ($k_x = 0, k_y = 0$) of the field that is constant over the origin ($= x, y$) plane. The red vector shows the propagation direction of the component that is oscillating with spatial frequency k_y at an angle of $\theta = \arcsin(k_y/k)$ with the incident beam. Finally blue shows the propagation direction of a spatial frequency component for which both k_x and k_y are non zero.

Using this relation (Eq. 9), numerical propagation of the field from one plane at $z = z$ to a parallel plane at some other position $z = z'$ can be accomplished through the following steps:

1. An inverse 2D Fourier transformation of the field in the object plane to calculate the Fourier spectrum.

2. Multiplication of the Fourier coefficients with phase factors $\hat{H}(k_x, k_y)$ to propagate the field.
3. 2D Fourier transformation of the propagated Fourier spectrum to find the field at a parallel plane.

Or, when written as an equation:

$$E(x, y, z') = \mathcal{F} \left(\mathcal{F}^{-1} (E(x, y, z)) \hat{H}(k_x, k_y, z - z') \right), \quad (10)$$

where \mathcal{F} denotes a 2D Fourier-Transformation over x and y .

2.1.3 Rayleigh-Sommerfeld theory (Real-space representation)

While the derivation of the real space representation is beyond the scope of this thesis (see Ch. 3 of Goodman [64] for an excellent treatise), we will discuss the result briefly as it is used as a starting point for calculating propagation between non-parallel planes that is discussed in Sec. 2.1.5 (which we have used as a theoretical basis for the work of Ch. 7). Sommerfeld [62] derived two so-called Rayleigh-Sommerfeld solutions. These solutions describe the propagation through free space of a field at points P_1 , located at the surface of a planar aperture at $z = 0$, to observation points P_0 (under the assumption that all contributing waves are travelling outwards from the aperture to the observation points). Under the additional assumption the separation between P_0 and P_1 is much larger than the wavelength, the first Rayleigh-Sommerfeld solution can be approximated by the following relationship (see Eq. (3-51) of Goodman [64]):

$$E(P_0) = \iint_{\Sigma} \frac{E(s_x, s_y, 0) \exp^{ik|\vec{r}_{01}|}}{|\vec{r}_{01}|} \cos(\theta) ds_x ds_y, \quad (11)$$

where \vec{r}_{01} is the vector that points from $P_0(x, y, z)$ to $P_1(s_x, s_y, 0)$, the integral is over all the points (s_x, s_y) on the surface of the aperture, and θ is the angle between the surface normal and \vec{r}_{01} . This configuration is shown in Fig. 4. As there is no bound on the size of the surface of the aperture, this relationship can also be used to describe the propagation through free space.

Eq. 11 can be interpreted as a mathematical formulation of the Huygens-Fresnel principle. This principle states that all points on a wavefront behave like secondary point sources emitting (hemi-)spherical waves radiating in the direction of propagation.

2.1.4 Fresnel and Fraunhofer approximations

For many optical problems, it is possible to make additional approximations to these diffraction integrals in order to greatly simplify diffraction calculations. For most problems the optical geometry of

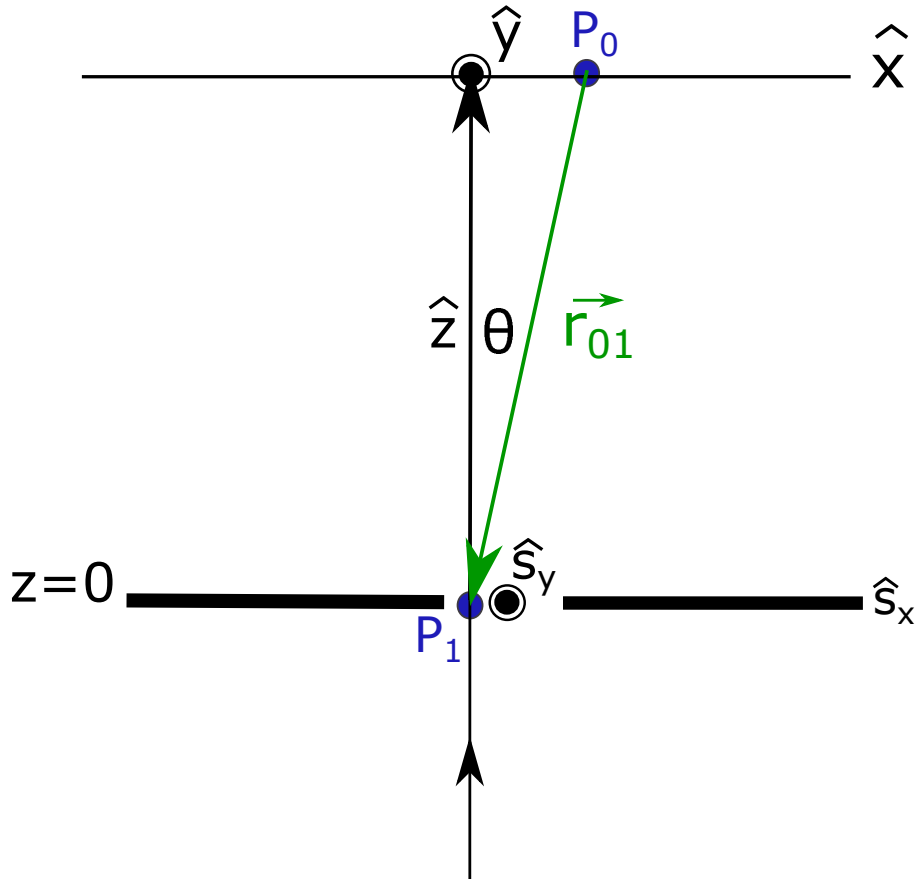


Figure 4: Illustration of scalar diffraction. Light incident from infinity, indicated by the black vector, scatters from points (P_1) on an aperture (with aperture plane coordinates $(s_x, s_y, 0)$) to the points on a co-linear plane with planar coordinates (x, y, z) located at a distance z from the aperture plane. r_{01} is the green vector pointing from a observation point (P_0) to P_1 . Adapted from chapter 3 of Goodman [64]

the problem is such that only a small range of propagation angles travel from the source plane to the area of interest at the observation plane, so that the z -components of the wave vectors arriving in that area are much larger than their lateral components $k_z^2 \gg k_x^2 + k_y^2$. In such situations, k_z can be approximated by means of a 1st-order Taylor-expansion: $k_z \approx k - \frac{k_x^2 + k_y^2}{2k}$, which can be inserted in the reciprocal space propagator (Eq. 8) to obtain,

$$\hat{H}_F(k_x, k_y, z) = e^{ikz} e^{-i \frac{k_x^2 + k_y^2}{2k} z}. \quad (12)$$

While it is possible to use this relation to numerically propagate fields in a way that is similar to how fields are propagated in the angular spectrum method, an expression can be derived in the real-space representation that is less expensive to calculate. To this end, Eq. 12 can be Fourier-transformed analytically to find a propagator in real space given by,

$$H_F(x, y, z) = e^{ikz} \iint dk_x dk_y e^{-i \frac{k_x^2 + k_y^2}{2k} z} e^{i(k_x x + k_y y)} \quad (13)$$

$$= e^{ikz} \frac{-i\pi k}{2z} e^{ik \frac{x^2 + y^2}{2z}} \quad (14)$$

Next, if we use this function to write Eq. 8 as a convolution in real space, we recover the following real-space diffraction integral:

$$E(x, y, z) = E(x, y, 0) \otimes H_F(x, y, z), \quad (15)$$

$$= e^{ikz} \frac{-i\pi k}{2z} \iint_{\Sigma} ds_x ds_y E(s_x, s_y, 0) e^{ik \frac{(x-s_x)^2 + (y-s_y)^2}{2z}}, \quad (16)$$

where s_x/y are the transverse coordinates of the field at $z = 0$. This result is called the Fresnel diffraction integral. This expression shows that in the paraxial approximation the field at an observation plane is the Fourier transform of the product of a quadratic phase curvature and the field at $z = 0$, which can be made more explicit by rewriting Eq. 16,

$$E(x, y, z) \propto e^{ikz} e^{ik \frac{x^2 + y^2}{2z}} \iint_{\Sigma} ds_x ds_y \left\{ E(s_x, s_y, 0) e^{ik \frac{s_x^2 + s_y^2}{2z}} \right\} e^{-i2\pi(u s_x + v s_y)}, \quad (17)$$

Where $u = \frac{kx}{2\pi z}$ and $v = \frac{ky}{2\pi z}$ are the spatial frequencies of the aperture-plane field. An identical expression can also be derived starting from Eq. 11 under the assumption that $\frac{(x-s_x)^2 + (y-s_y)^2}{z^2} \ll 1$ as is shown in Ch. 4.2 of Goodman [64]. As Eq. 17 only requires a single Fourier-transformation to calculate the diffraction-plane field, numerical implementation through fast Fourier-transform algorithms are computationally inexpensive, and under the relative far-field conditions in

which the paraxial approximation is valid, have sampling conditions than are typically less restrictive than those of the angular spectrum method.

In the optical far-field $\frac{k(s_x^2 + s_y^2)_{\max}}{2z} \ll 1$, the diffraction integral can be simplified further, in this case the quadratic phase term under the integral varies sufficiently slowly to be treated as constant. which is called the Fraunhofer or far-field approximation. This approximation leads to the following Fraunhofer diffraction integral:

$$E(x, y, z) \propto e^{ikz} e^{ik \frac{x^2 + y^2}{2z}} \iint_{\Sigma} ds_x ds_y \{E(s_x, s_y, 0)\} e^{-i2\pi(us_x + vs_y)}. \quad (18)$$

As the the pre-factor phase terms do not influence the measured far-field intensities, but only the beam divergence, they are often neglected in far-field propagation calculations. While the true far-field conditions are quite stringent, Fraunhofer propagation formulas can often still be used to predict diffraction intensities with good accuracy, even when strict far-field conditions do not apply, given that the phase curvature is small: $\left(\frac{k(s_x^2 + s_y^2)_{\max}}{2z} < 1\right)$. The error induced by not taking this phase curvature into account in such cases is mostly limited to misjudging the degree of convergence/divergence of the field, which is not relevant for all applications.

2.1.5 Tilted plane diffraction

The angular spectrum method as well as the Fraunhofer and Fresnel diffraction integrals only describe the propagation of light between parallel planes. However, for some applications, it can be beneficial to do imaging in a geometry in which the object and the detector planes are non-colinear. In particular, for imaging with illumination at extreme-ultraviolet wavelengths such as those emitted by high-harmonic sources. In that spectral range most materials tend to be opaque and normal incidence reflection coefficients are low, while reflectivities for scattering angles that tend towards grazing incidence are close to unity. Such a tilted-plane reflection geometry is illustrated in Fig. 5. In the work of Ch. 7, we have developed a tool that helps calibrate the scattering angle in such a geometry.

As the Rayleigh-Sommerfeld formulation of Eq. 11 describes the propagation from a planar screen to a point in 3D space, it could in principle be directly implemented to calculate propagation of the field from a screen to all points on a tilted surface separately, however, using direct integration, such calculations are much slower than the Fast Fourier Transform methods used in the angular spectrum method or for calculating Fresnel diffraction. As the iterative algorithms used in CDI need to repeatedly propagate the field in between planes, calculations with the Rayleigh Sommerfeld integral would be

prohibitively slow. However, it is possible to use a coordinate transformation to far-field intensities measured on the detector to find the Fourier-space intensities of the specimen field, as they would have been measured in a colinear geometry.

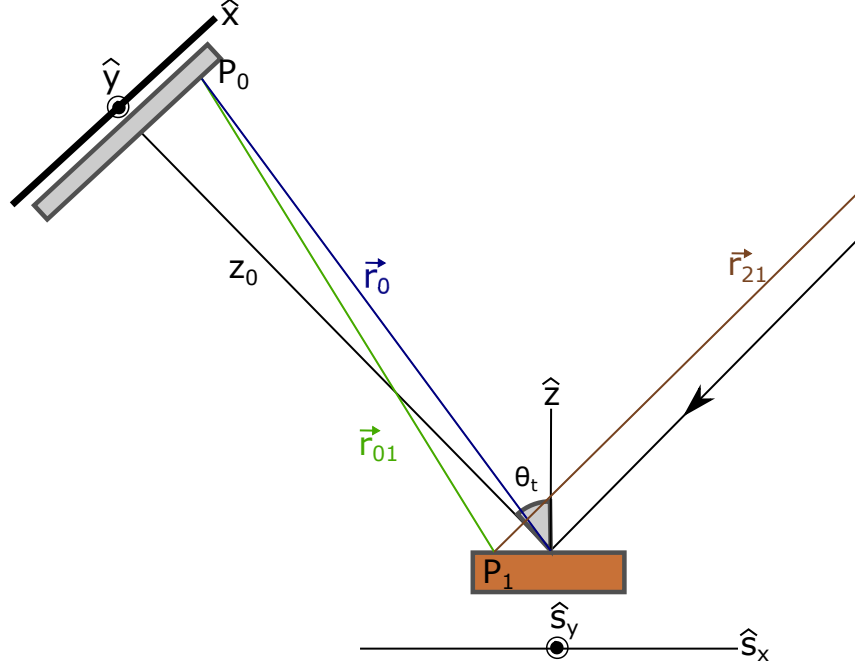


Figure 5: Tilted-plane reflection geometry. A beam incident from infinity (propagating in direction \vec{r}_{21}) reflects from a sample surface and scatters from a point P_1 on the sample to a point P_0 on a detector. \vec{r}_{10} denotes the vector pointing from P_1 to P_0 , while \vec{r}_0 is the vector from P_0 to the origin of the sample coordinates and z_0 is the distance between the origin sample coordinates and the origin of the detector coordinates. θ_t is the tilt angle between the incident beam and the normal (\hat{z}) of the surface of the specimen. The sample plane axes are denoted by (\hat{s}_x, \hat{s}_y) , while (\hat{x}, \hat{y}) denote the the detector plane coordinates.

Here we will follow an approach that is based on the pioneering work of Patorksi [65] and Rabal [66]. In this approach, Fraunhofer-like approximations are made to the Rayleigh-Sommerfeld diffraction integral to find a simple map from tilted-plane coordinates to spatial frequency coordinates of the object. In later work, this problem has also been treated with Fresnel-like approximations [67], and with an angular spectrum approach [68].

Consider the Rayleigh-Sommerfeld integral (Eq. 11) for a field that scatters from a point P_1 on a reflection surface to point P_0 at a non-colinear detector plane. The detector normal is assumed parallel to the incident beam in our configuration. The distance between a point P_1 on the reflective surface to a point P_0 on the detector is given by

$$r_{01} = \sqrt{(z_0 - s_x \sin \theta_t)^2 + (x - s_x \cos \theta_t)^2 + (y - s_y)^2}, \quad (19)$$

where θ_t is the angle of between the two planes. s_x and s_y are object-plane coordinates, x and y are detector-plane coordinates, z_o is the distance from the origin of the object plane to the origin of the detector plane, r_{01} is the distance between points P_1 and P_0 , and r_o is the distance from the origin of the object-plane to point P_0 . r_{01} can be rewritten as a function r_o instead of z_o , which gives the following expression,

$$r_{01} = \sqrt{r_o^2 + (s_x^2 + s_y^2) - 2s_y y - 2s_x \left[x \cos(\theta_t) + \sin(\theta_t) \sqrt{r_o^2 - x^2 - y^2} \right]}. \quad (20)$$

As long as the r_o^2 is much larger than the other terms, a first order Taylor expansion of the form $\sqrt{1 + \epsilon} = (1 + \frac{\epsilon}{2})$ can be used to expand the root of Eq. 20, which we can use to derive the following equation:

$$r_{01} \approx r_o + \frac{(s_x^2 + s_y^2) - 2s_y y - 2s_x \left[x \cos(\theta_t) + \sin(\theta_t) \sqrt{r_o^2 - x^2 - y^2} \right]}{2r_o}. \quad (21)$$

Next, this expression for r_{01} can be filled in the Rayleigh-Sommerfeld diffraction integral to obtain a Fresnel-like tilted-plane diffraction integral. For calculating the amplitude factor that depends on r_{01} , all terms beside r_o can be dropped with little loss of accuracy under the conditions where the first order Taylor approximation is valid, while for the phase term all terms must be kept (as relatively small changes in phase can result in significant differences in diffraction intensities). This results in the following expression:

$$E(P_0) \propto e^{ikr_o} e^{ik \frac{x^2+y^2}{2r_o}} \iint_{\Sigma} ds_x ds_y E(s_x, s_y, 0) e^{ik \frac{s_x^2+s_y^2}{2r_o}} e^{-i \left(s_y \frac{ky}{r_o} + s_x \frac{k \left[x \cos(\theta_t) + \sin(\theta_t) \sqrt{r_o^2 - x^2 - y^2} \right]}{r_o} \right)}. \quad (22)$$

This equation has an almost identical form to Eq. 17. However, it contains the following re-scaled spatial frequencies

$$u = \frac{\left[x \cos(\theta_t) + \sin(\theta_t) \sqrt{r_o^2 - x^2 - y^2} \right]}{\lambda r_o} \quad (23)$$

$$v = \frac{ky}{\lambda r_o}. \quad (24)$$

These two equations form the basis of the forward coordinate transformation used in Ch. 7.

LENSLESS IMAGING

3.1 THE PHASE PROBLEM

The relationship between a coherent 2D field scattering from a sample, which is frequently referred to as the *exit wave*, and the same field propagated to a parallel detector plane, separated by a distance z , can be described by,

$$E(x_d, y_d) = \mathcal{P}_z \psi(x, y). \quad (25)$$

Here, $E(x_d, y_d)$ and $\psi(x, y)$ are the detector and sample plane fields respectively, \mathcal{P}_z is a function describing the propagation between the two planes (see Ch. 2), x and y are the 2D sample plane coordinates, while x_d and y_d are detector plane coordinates.

When the complex electric field at the detector is known, it is typically possible to recover a high resolution image of the object field through numerical back propagation with the inverse of \mathcal{P}_z . However, photon detectors only capture intensity signals and do not directly measure the phase of the electric field, and the amplitude signal does not contain sufficient information to calculate the field in the source plan as the phase gradients encode the local propagation direction of the light.

A intensity measurement does impose the following constraint on valid solutions for the far-field electric field,

$$I(x_d, y_d) = |E(x_d, y_d)|^2. \quad (26)$$

Extracting the full complex electric field from its intensity alone is an ill-posed problem: Any field with the same amplitude pattern as the true solution satisfies the measurement constraint of Eq. 26. This chapter will discuss a number of ways to retrieve the phase and thus solve this so-called ‘phase problem’ for the purpose of imaging.

3.2 SINGLE SHOT PHASE RETRIEVAL METHODS

3.2.1 Holography

One way to measure the phase of a field is by recording the interference with a known reference wavefront. In this case, the phase-difference of the field with respect to reference is encoded in the intensity through their interference terms. This hologram can be read out by using numerical or optical propagation to separate out the signal from one of the interference terms from the other intensity

terms. Techniques based on this idea are known as *holography*, a term introduced by Gabor [50] when he pioneered the first method to reconstruct the field based on this principle in 1948. He recorded the interference of a weakly scattering object and a unscattered spherical reference wave on a photographic plate located in a Fresnel plane. The intensity signal at the detector for any holographic interference can be described by,

$$I_{\text{holo}} = |\mathbf{R} + \mathbf{O}|^2 = |\mathbf{R}|^2 + |\mathbf{O}|^2 + \mathbf{O}\mathbf{R}^* + \mathbf{R}\mathbf{O}^*, \quad (27)$$

where \mathbf{R} is the known reference wave, while \mathbf{O} is the field scattered by the object, both located at a detector plane at a distance z of the specimen. After exposure, the photographic plate's transmission function $t(x_d, y_d)$ scales approximately linearly with the exposing intensity signal. A recorded hologram can be read-out by illuminating the photographic plate with an optical wave that resembles the reference wave. The result is a field with an amplitude proportional with I_{holo} , and a phase that is that of the reference. After propagation of this field with a distance z , a twin image of the scattered field is generated, associated with the cross terms of I_{holo} : An in-focus image with a real focus at a distance z , and an out of focus background image with a virtual focus at a distance $-z$. The original method was limited by poor signal-to-background ratios due to the defocused twin image. However, holographic methods gained prominence since due to a number of improvements during the course of the last century. Off-axis holography [69], where a separate non-collinear reference is used to record a hologram, enables spatial separation of the twin images, greatly improving signal to background. Improvements in computing power and information theory led to the adaptation of digital holographic methods [70, 71], where the hologram is recorded digitally on a camera, and the propagation of a field with an amplitude scaling with I_{holo} is done computationally instead of optically. Of special importance to this work is Fourier holography, a special form of off-axis digital holography, in which the reference wave is generated by the illuminating beam itself diffracting on a pinhole in the plane of the specimen and the intensity is measured in a Fourier plane. Then, the interferometric intensity of Eq. 27 is Fourier transformed, which will give rise to the following complex signal:

$$\hat{I}(x, y) = \hat{\mathbf{O}} \otimes \hat{\mathbf{R}}^* + \hat{\mathbf{R}} \otimes \hat{\mathbf{O}}^* + \hat{\mathbf{R}}^* \otimes \hat{\mathbf{R}} + \hat{\mathbf{O}}^* \otimes \hat{\mathbf{O}}, \quad (28)$$

where the hats indicate the Fourier transforms of the corresponding detector plane fields and \otimes denotes a convolution. As the diffraction patterns in Fourier-holography are measured in a Fourier plane of the specimen, these are equivalent to the object and reference waves in the specimen plane. The autocorrelations of \mathbf{R} and \mathbf{O} in this expression are centered around zero, and will be spatially separated from the cross-correlation terms, which are centered on plus or minus the

real space separation between the object and the pinhole. These cross terms produce a pair of mirrored twin images both convolved with the pinhole wave. Compared to off-axis holography this method does not require a carefully aligned and calibrated reference beam. However, unlike other holographic methods there is a trade-off between resolution and signal strength that both scale with the size of the pinhole.

3.2.2 Coherent Diffractive Imaging

As an alternative way to recover the phase, it is possible to make the inverse problem well-posed by constraining the solution at multiple diffraction planes (usually the object and detector planes). This can be achieved either through an additional measurement or through additional priors. The complex field can then be reconstructed through iterative optimisation. The group of methods that employ this strategy are known as Coherent diffractive imaging or CDI [5, 18]. This type of approach was first introduced in the field of x-ray crystallography by Hoppe and Gassman [72, 73]. However, due to the different challenges for periodic crystal and non-periodic objects, it was not immediately apparent that these methods could be applied for general imaging, especially due to the difficulties in constraining the phase problem sufficiently to obtain unique solutions. Not only do the crystallographic algorithms use constraints that apply specifically to crystals, but the periodic structures of crystals also generate very bright Bragg orders and thus their diffraction signal has a very good signal-to-noise ratio. However, the solution to the non-periodic diffractive phase problem was already identified, in 1952 [74] by Sayre who remarked that in principle, based on Shannon's sampling theory, the crystallographic phase problem could in most cases be solved uniquely if the intensity of the diffraction pattern halfway between Bragg peaks could be determined. While these measurements are not possible for crystallographic structures, they can be measured for confined imaging objects. The first iterative imaging algorithm that would be applied to non-periodic objects was introduced in 1972 by Gerchberg and Saxton. They developed an algorithm [75] that uses simultaneous intensity measurements at both an image plane and its far-field diffraction plane and uses iterative optimisation algorithms to find a solution that fits both data sets. However, these type of measurements are often impractical for 2-dimensional imaging and, as Fienup demonstrated in 1978 [20], it is often possible to reconstruct the field from the Fourier-modulus of an object alone if constraints based on prior knowledge of the finite *support* of the specimen plane are applied instead of measured image plane intensities. While he developed these methods for radio-astronomy, the inverse scattering problem for the far field diffraction patterns of isolated objects is identical.

Work by Bruck and Sodin [76], Bates [77, 78] and others in the early 80s showed that the inverse problem for non-periodic, real-valued objects is almost unique, as long as the Fourier-space intensity pattern is sampled at at-least twice the Nyquist-Shannon sampling rate (which mirrors Sayre’s earlier observation). Bates argued that for such diffraction patterns the field at a sample point is the the sum of the fields in the neighbouring sample points, which generates a phase solution that is unique aside from reflection and translation symmetries, and that for real-valued objects, this solution is always the most compact object allowed by the measurement. This realisation explains the effectiveness of the finite object size priors introduced previously by Fienup. While transmission functions are typically nearly pure phase objects in hard x-ray and electron microscopy, the refractive index can act as a real-valued object instead of the transmission function for pure phase modulating specimen under a weak phase approximation [18]. These developments led to the first single-shot x-ray CDI experiment in 1999 by Miao [79].

This approach, in which the object field is reconstructed with only a single intensity measurement, will be referred to here as *conventional coherent diffractive imaging* (cCDI) to distinguish them from *ptychographic CDI* (pCDI) methods. cCDI experiments work under a thin sample assumption. This is the assumption that the scattering can be described as a single two dimensional transmission or reflection function acting on the illumination. This assumption only holds if the specimen is thin enough for the following two requirements to be satisfied: 1) Multiple scattering contributions need to be negligible. 2) Propagation effects on the beam profile inside the sample need to be negligible. The sample thickness for which this second assumption holds depends on the degree of wavefront curvature. It is common practice in these single-shot experiments to refer to the sample-plane exit wave as the object, as the object transmission function is non-separable from the exit wave with single shot data sets. We will follow this convention in the following section, but not in the sections about pCDI.

3.2.3 Object priors in cCDI

The most commonly used object source of prior in cCDI experiments is the assumption that the object transmission function is real and only has non zero-values within some known area [20], within the so-called finite object *support*,

$$o_{i+1}(\vec{r}_s) = \begin{cases} 0 & \vec{r}_s \notin S \\ o_i(\vec{r}_s) & \vec{r}_s \in S \end{cases}, \quad (29)$$

where $\vec{r}_s = (x, y)$ is the distance from the sample origin to a different point on the sample plane, o_i is the i -th object update, and $S(x, y)$

is the support. The shape and size of the support are often based on low resolution images of the sample [20]. Alternatively, as long as the object transmission is approximately binary and the exit wave can be described as a real-valued object, the support itself can be iteratively refined based on a threshold value in the reconstruction, using a method called shrink-wrap [80]. For measurements in the far-field regime a first support can be extracted from the autocorrelation of the sample plane field, which is obtained from the Fourier transform of the intensity at the detector. As discussed in the previous section, the solution for such real-valued finite size objects must be the most compact object that is consistent with the measurement.

In crystallography [81], good support information is typically not readily available due the repeating nature of the crystal lattice. Instead, in crystallography, it can often assumed that the scattering of the object can be fully attributed to the sum of a known amount of well-separated point particles, a property that is sometimes referred to as *atomicity* [82]. For real-valued objects, such as for holes in plates or other objects that induce a homogeneous phase delay, a positive real valued object is usually enforced. This prior is called the *positivity* constraint [82]. This constraint uses the following update step,

$$o_{i+1}(\vec{r}_s) = \begin{cases} \mathbb{R}\{o_i(\vec{r}_s)\} & \mathbb{R}\{o_i(\vec{r}_s)\} > 0 \\ 0 & \mathbb{R}\{o_i(\vec{r}_s)\} < 0. \end{cases} \quad (30)$$

This constraint is often applied in combination with a support or atomicity constraint [82], which can increase the rate of convergence of the reconstruction, as the space of approximate solutions is greatly reduced. For the experimental results described in Ch. 6, an update step was implemented that constrains the solution for the object in a similar way, through replacing the object by its absolute value,

$$o_{i+1}(\vec{r}_s) = \beta |o_i(\vec{r}_s)| + (1 - \beta) o_i(\vec{r}_s), \quad (31)$$

Where β is a relaxation parameter, with a value close to one, that slightly eases the constraint. So that small phase curvatures are still allowed. The differences between these methods are subtle, in both cases a positive real valued object is the only real solution. Eq. 30 is a distance-minimising projection on the set of positive real numbers, while Eq. 31 is not distance minimising. However, unlike Eq. 30, this constraint conserves the size of the transmission function.

3.2.4 cCDI Algorithms

The goal in iterative cCDI reconstructions is to find a (hopefully unique) solution for the complex field that satisfies both these object priors and the measurement constraint of Eq. 26. A straightforward method

to do this, called the error reduction algorithm [20], applies alternating projections on the constraint sets in object space and detector space. This general approach is illustrated in Fig. 6.

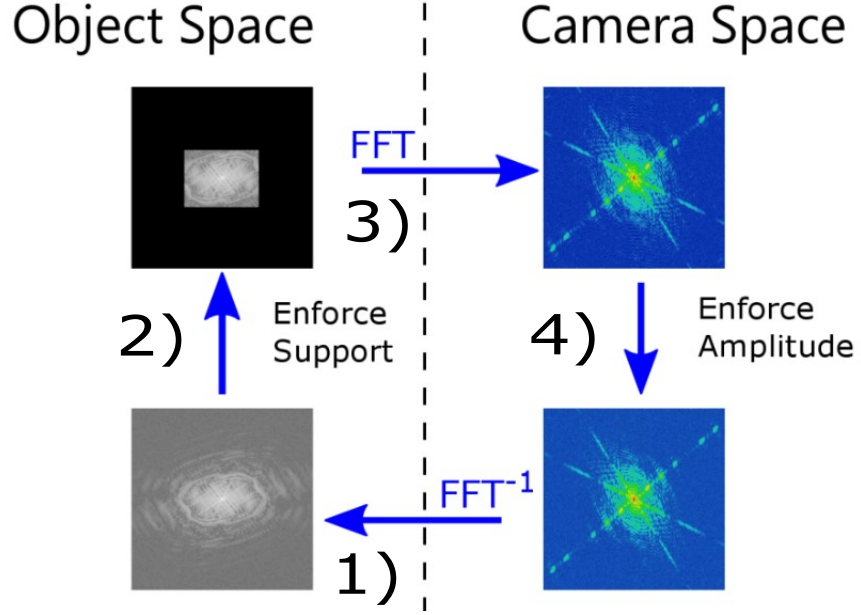


Figure 6: Schematic depiction of the error reduction algorithm.

- 1) A guess for the detector field with incorrect phases is propagated to the object plane numerically through a fast Fourier transformation (FFT).
- 2) The object support, based on prior specimen knowledge, is enforced by setting all pixel values outside the support region to zero.
- 3) The updated object field is propagated back to the detector to obtain a new guess for the detector plane field with incorrect amplitudes.
- 4) Finally, the amplitudes measured by the detector replace the amplitudes in this guess, completing a single iteration of the algorithm.

After starting with an initial guess for the electric field in detector plane with a random phase distribution, the field can be propagated to the sample plane by means of a fast Fourier transform (FFT), assuming the camera is located in the far-field (see Eq. 18). This will generate a first guess for the object transmission function. Next, the object-space constraints are applied, and the field is propagated back to the diffraction plane through inverse FFT. Subsequently, the field guess is projected on the measurement constraint set by replacing the far-field amplitudes with the measurement amplitudes, while keeping the phases from the object update

$$E_i(x_d, y_d) = \frac{\mathcal{F}[o_i(x, y)]}{|\mathcal{F}[o_i(x, y)]|} \cdot \sqrt{I(x_d, y_d)}. \quad (32)$$

Here $E_i(x_d, y_d)$ is the i -th update of the electric field and \mathcal{F} denotes a Fourier transform. Originally interpreted as a method of projections on constraint sets, it was shown by Fienup [19] that the error-reduction algorithm can also be interpreted as a gradient-descent method. While in many cases this error-reduction algorithm can recover a good image of the object, it is known to be sensitive to stagnation in local minima, instead of converging to a global optimum [19]. In 1982 [33], Fienup proposed an adjusted approach to find a solution. In this approach, the problem is described as a system where the input g_i generates an output g'_i by applying the detector constraint in Fourier space to the input, followed by a Fourier transformation of the resulting camera-space field to object space. As the object space output satisfies the measurement constraint by definition, an output that satisfies the object-space constraints is a solution to the phase retrieval problem. The difference with respect to the error reduction method is that the input is no longer required to satisfy the object constraint itself, which provides additional freedom for the algorithm to find a solution. Fienup proposed three so-called input-output algorithms, the most successful of which is the hybrid-input-output (HIO) algorithm and the update step for this algorithm is given by

$$g_{i+1}(\vec{r}_s) = \begin{cases} g'_i(\vec{r}_s) & \vec{r}_s \in C \\ g_i(\vec{r}_s) - \beta g'_i(\vec{r}_s) & \vec{r}_s \notin C \end{cases}, \quad (33)$$

where C is the set of points in which output $g'_i(\vec{r}_s)$ already satisfies the object constraints and β is a feedback parameter with value that is smaller than one. In the places that the output satisfy the object space support the solution is not adjusted, while in those points where the output does not satisfies the constraints the input is driven to decrease until the output goes to zero.

3.3 PTYCHOGRAPHY

3.3.1 Solving the phase problem through transverse scanning

While the cCDI approach often works well for isolated real-valued objects or for objects with known periodicity, it requires significant prior knowledge about the specimen to reconstruct objects that do not fulfil these criteria. For many applications this kind of information might not be available. In recent decades, *ptychographic CDI* (pCDI), has emerged as a successful alternative [83] that overcomes these limitations. Ptychography is used to denote a group of methods to solve the phase problem, in which (paraphrased from [84]):

1. There is an optical component that can be shifted laterally relatively to the illumination.

2. A detector located in another plane records the interference pattern for at least two relative positions.
3. There must be sufficient overlap between the illuminated areas at different recorded positions.
4. The illumination source is sufficiently coherent to be modelled accurately as coherent or as an incoherent sum of a limited amount of coherent modes.
5. An object transmission or reflection function is recovered numerically from these measurements.

It turns out that a unique solution for the phase problem exists, if instead of the inverse problem for a single diffraction pattern the inverse problem for a set of diffraction patterns is considered in which the sample is laterally scanned through a localised beam with overlapping illuminated areas. This further constrains the single diffraction pattern problem, as solutions for the illuminated part of the object at one scan location must comply with data generated at neighbouring scan positions.

For example, a specimen and a specimen in a mirrored orientation would result in identical diffraction intensities at the detector. However, if another diffraction pattern is recorded, while the specimen is shifted with some fraction of the beam, then the incorrect mirrored solution for the first measurement is not consistent with either the solution for the second measurement or the mirrored image of the solution for the measurement, unless the object is periodic with the periodicity of the scan grid steps. The idea that the phase problem in far field diffraction measurements can be solved through transverse scanning of the illumination function is based on the pioneering theory work of Hoppe [85], who showed that for periodic structures the ptychographic phase problem has a unique solution, while later it was shown to also hold for non-periodic structures [83].

In ptychography, like in cCDI, the exit wave of a single measurement is usually described as the multiplication of the probe and a thin sample. For each measurement the object is shifted with respect to the illumination which leads to the following forward model

$$\psi_j(\mathbf{r}) = P(\mathbf{r})O(\mathbf{r} - \mathbf{R}_j), \quad (34)$$

$$I(x_d, y_d)_j = |\mathcal{P}_z \psi_j(x, y)|^2, \quad (35)$$

where \mathbf{R} indicates the real-space displacement and the subscript j indicates the values of a variable at the j -th scan position. The ptychographic configuration is schematically shown in Fig. 7. Here the red circles indicate the areas illuminated by the illumination for a single scan position.

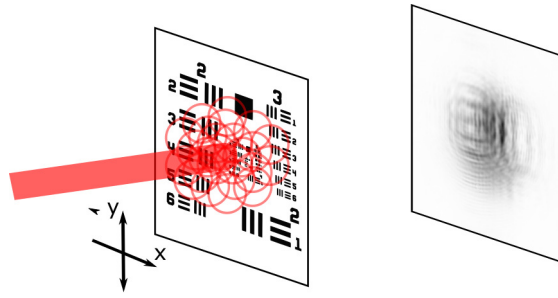


Figure 7: Ptychographic measurement scheme in transmission. A thin specimen is illuminated by a confined probe and the resulting diffraction pattern is recorded at a detector, then the specimen is laterally translated by a fraction of the size of the probe, illuminating a partially overlapping area. The red circles indicate an area that is illuminated by the probe at a single position of the sample, adopted from my co-worker M. Du [86].

3.3.2 Wigner-distribution deconvolution method

In the 90's, the first practical implementation using the information of ptychographic data sets was developed by Rodenburg and Bates, to reconstruct crystallographic structures [87, 88]. This method, the so-called *Wigner-distribution deconvolution method* (WDDM), is different from later ptychographic CDI methods and finds an analytical solution to phase problem by applying a Fourier transform on the measured intensities over both the detector coordinates and the probe positions in order to fully separate the contributions of the exit wave of the probe and object functions in the resulting integral [89]. However, the contributions of the probe and the object are only separable up to the highest spatial frequency present in the scan grid raster, and therefore the acquisition of very large data sets is required to achieve a combination of a high resolution and field of view. In fact, when the method was introduced, the long measurement times and high memory requirements limited this technique to images of 32x32 pixels [89]. Recently, however, there has been renewed interest for these direct ptychography methods due to technological advances in fast pixel detectors and computational memory [90].

3.3.3 Ptychographic CDI

In principle, the phase problem from a ptychographic data set has a unique solution for data sets with less dense sampling of relative probe-specimen positions than the sampling that is required for WDDM. In fact, in the case of a known periodic sample, it can be shown that only three diffraction patterns are sufficient to obtain a unique solution for the phase problem (see Ch. 2 of [83]). To avoid the amount of data required for WDDM, Rodenburg developed an al-

ternative approach to reconstruct specimen from ptychographic data in 2004: the Ptychographic iterative engine (PIE) [21]. The family of PIE algorithms combines the iterative optimisation techniques used in CDI with ptychographic data sets that are undersampled for spatial Fourier-transform. This approach avoids both the space-bandwidth limitations of WDDM as well as the necessity of strict specimen priors that are required for cCDI. While the algorithm initially proposed assumes a known wavefront, a significant improvement was achieved by solving for the complex probe and object wavefront separately through the extended ptychographic iterative engine (ePIE) algorithm [91]. By separating the illumination from the specimen, ptychography CDI is simultaneously an imaging and a high-resolution wavefront sensing technique. Furthermore, the separation of object and probe functions prevents degradation of the object image quality by aberrations in the illumination wavefront. In fact, several experimental studies have indicated that aberrations present in the wavefront tend to improve image quality and reconstruction robustness in ptychographic reconstructions [92, 93]. An important feature of PIE-inspired algorithms is the feasibility of solving for extra variables that are separate from the 2D specimen and functions. This is possible due to the highly over-constrained nature of ptychographic data sets. For example, several studies have shown that its possible to calibrate the axial position [25], to correct the lateral probe positions [94], or to model the object as a stack of 2D object slices [24] and solve for all of those. A special lens-based form of ptychography that has gathered attention in the recent decade, especially for visible light experiments, is Fourier ptychography [31, 95]. In Fourier-ptychography, a small-NA lens is used to obtain low-resolution, high field-of-view (FoV) image-plane intensities on the detector. By changing the angle from which the specimen is illuminated, the part of spatial-frequency space of the specimen that is captured by the lens aperture shifts laterally (see Eq. 9), and reconstruction algorithms identical to conventional ptychography can subsequently be used to reconstruct the field (where the shifting part of spatial frequency space field captured by the lens fills the role of the shifting object in diffraction-based ptychography, while the imaging lens and pupil combination fills the role of the probe).

3.3.4 *PIE-type algorithms*

In this section a description of the basic steps of several ptychographic algorithms used in Ch. 7 are described and the derivation of the ePIE update rules is given. Fig. 8 gives a basic flow chart for the steps of PIE and the algorithms discussed below. First we will start with describing the algorithmic steps of the ePIE algorithm. At each iteration of the ePIE algorithm [22], the following steps are applied once,

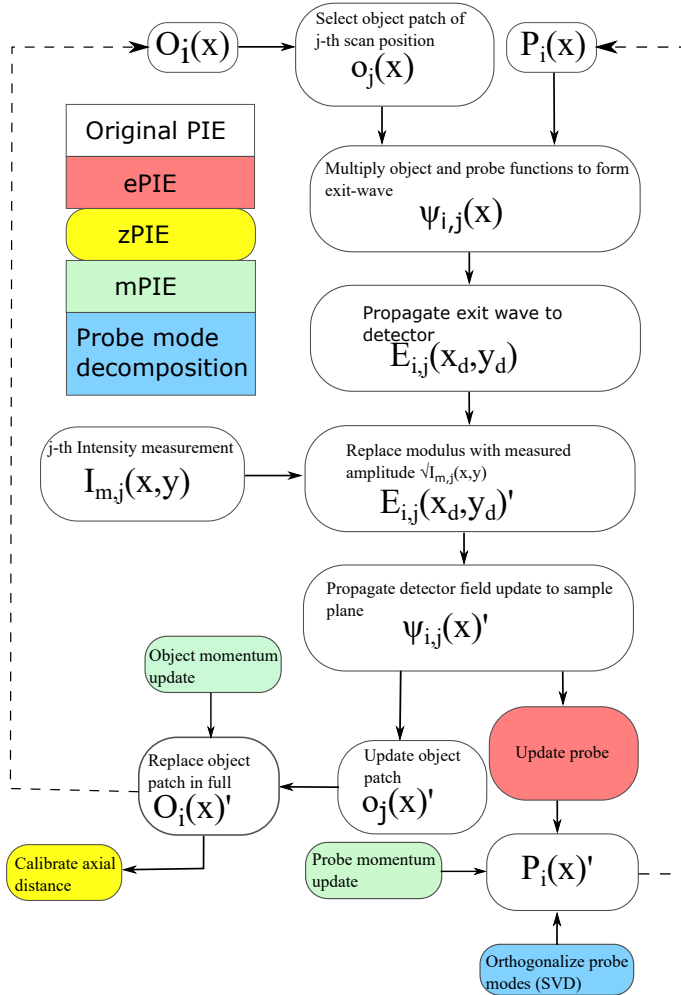


Figure 8: Flow chart of PIE algorithms, showing the different update steps for different extensions to the original PIE algorithm used in this thesis. The uncoloured boxes are the steps of the original PIE algorithm and are shared with all other listed algorithms, while the update step in red is the probe refinement step introduced by ePIE [22] and is shared with all algorithm except for the original PIE algorithm. Other possible extensions include axial distance calibration (zPIE [25], yellow), momentum acceleration to improve convergence (mPIE, green) [91] and orthogonal mode decomposition (blue) [27].

sequentially, to each scan position. An object patch $o_j(\mathbf{r})$ that encompasses the area illuminated at the j -th scan location is selected from the larger object $O(\mathbf{r} - \mathbf{R}_j)$ and is multiplied with the current probe guess $P_i(x)$ to obtain a guess for the j -th exit wave (see Eq. 34). Next, the forward model is used to propagate this exit wave guess to the detector plane. Then, like in Eq. 32 the modulus is replaced by the measured modulus $\sqrt{I_j}$. After back propagation, an updated guess for the exit wave $\psi'(\mathbf{r})$ is obtained. Then, the object and probe are updated with the following update rules.

$$o'_j(\mathbf{r}) = o_j(\mathbf{r}) + \alpha \frac{P^*(\mathbf{r}) (\psi'_j(\mathbf{r}) - \psi_j(\mathbf{r}))}{|P_{\max}|^2} \quad (36)$$

$$P'(\mathbf{r}) = P(\mathbf{r}) + \alpha \frac{o_j'^*(\mathbf{r}) (\psi'_j(\mathbf{r}) - \psi_j(\mathbf{r}))}{|O_{\max}|^2}, \quad (37)$$

where α is a stepsize, that is chosen between 0 and 1 and is often chosen to be unity. Next, the object patch update o'_j replaces the corresponding area in the larger object array O_i and the full sequence described above is repeated once over all scan location j for each iteration i of the algorithm, which itself is repeated until the algorithm has converged.

The ePIE object and probe updates of Eqs. 36 and 37 can be understood in several ways [91]. While the original article, like CDI previously, was described in terms of projections on constraint sets, here we will follow the formalism from the supplementary by a paper of Thibault and Menzel [26]. In this description the object update rule is derived by minimising the difference between the exit wave updated by the data $\psi'(\mathbf{r})$ and the exit wave predicted by the model (Eq. 34), through the cost function

$$L = \sum_{\mathbf{r}} |P(\mathbf{r})o'_j(\mathbf{r}) - \psi'(\mathbf{r})|^2 + \sum_{\mathbf{r}} \mu(\mathbf{r})|o'_j(\mathbf{r}) - o_j(\mathbf{r})|^2, \quad (38)$$

where the primes denote variable updates. The second term in this equation is a regularisation term (a secondary constraint on a solution to avoid over-fitting) that penalises rapid changes in the object updates with a chosen regularisation weight $\mu(\mathbf{r})$ and is allowed to vary spatially. A natural choice could be to resist rapid changes of the object at locations that were only weakly illuminated in the measurement responsible for the current object update. For example, this can be accomplished with the weight function: $\mu(\mathbf{r}) = |P_{\max}|^2 - |P(\mathbf{r})|^2$. This weight function penalises rapid changes of the object that are based on data with a relatively small signal-to-noise ratio, at the cost of potentially slower convergence. This choice for the regularisation weights will result in an update rule that is identical to the ePIE object update rule, apart from a chosen stepsize constant. The minimum of the cost function must satisfy its Euler-Lagrange (EL) equations.

As the traditional derivative is undefined for many complex functions (see App. A for a short explanation or the review by Kreutz and Delgado [96] for a more rigorous explanation), we will make use of complex-real (or Wirtinger [97]) derivatives to do the derivation for the EL equations. For these derivatives, we follow the definition suggested by [96]. In this definition (see App. A), the derivative of a function to its complex conjugate function is zero $\partial f/\partial f^* = 0$.

$$\frac{\partial L}{\partial(o_j^*)} = P^*(\mathbf{r}) (P(\mathbf{r})o_j'(\mathbf{r}) - \psi_j'(\mathbf{r})) + \mu(\mathbf{r}) (o_j'(\mathbf{r}) - o_j(\mathbf{r})) = 0. \quad (39)$$

This equation can be solved for the object patch update o_j' ,

$$o_j'(\mathbf{r}) = o_j(\mathbf{r}) + \frac{P^*(\mathbf{r}) (\psi_j'(\mathbf{r}) - P(\mathbf{r})o_j(\mathbf{r}))}{|P(\mathbf{r})|^2 + \mu(\mathbf{r})}. \quad (40)$$

The probe update can be found with a identical approach. This results in the following regularisation weight functions for object and probe,

$$\mu_{\text{object}}(\mathbf{r}) = |P_{\text{max}}|^2 - |P(\mathbf{r})|^2 \quad (41)$$

$$\mu_{\text{probe}}(\mathbf{r}) = |O_{\text{max}}|^2 - |o_j(\mathbf{r})|^2. \quad (42)$$

It is then possible to derive the following ePIE update rules [91]:

$$o_j'(\mathbf{r}) = o_j(\mathbf{r}) + \alpha \frac{P^*(\mathbf{r}) (\psi_j'(\mathbf{r}) - \psi_j(\mathbf{r}))}{|P_{\text{max}}|^2} \quad (43)$$

$$P'(\mathbf{r}) = P(\mathbf{r}) + \alpha \frac{o_j'^*(\mathbf{r}) (\psi_j'(\mathbf{r}) - \psi_j(\mathbf{r}))}{|O_{\text{max}}|^2}. \quad (44)$$

For some of the results of Ch. 7, the combination of the angular correction algorithm aPIE presented in the paper with the zPIE algorithm is investigated [25]. zPIE is an extension to the PIE algorithm that can calibrate the axial propagation distance. This distance is one of the experimental parameters incorporated in the forward model for ePIE. If the solution for the detector-space field is back-propagated from the detector plane to a plane at an axial distance that is close to, but not quite at the sample plane, then the apparent probe size will be different from the real probe size. This will cause the algorithm to misestimate the size of the scan grid and miscalculate the location in the greater object that should be updated by an object patch so that the candidate solution in a region will approximate a coherent sum of non uniformly shifted object updates. zPIE makes use of this property, by propagating an ePIE candidate solution to several axial planes close to the current best estimate for the axial distance. Then, it optimises a sharpness metric to find a better guess for the axial distance to specimen plane. Note that this can only calibrate the axial distance if the features in the object or probe vary significantly over a distance that is smaller than the apparent shifts of the scan grid.

3.3.5 *Convergence acceleration through momentum acceleration in ptychography*

While the diversity of the information in ptychographic data sets can typically overcome the non-uniqueness of the field solutions that is present in the single-diffraction-pattern inverse scattering problem, stochastic gradient descent (SGD) algorithms like ePIE (in which local gradient updates are calculated at sub-data sets) are known to be vulnerable to stagnation near saddle points and local minima. For example, convergence can be slow if there are approximate solutions that are consistent with the forward model for all but a small fraction of sub-data sets. Increasing the stepsize typically increases the convergence rate, but can also induce instability or even divergence, as the optimal stepsize might not be identical for each sub-dataset. To accelerate the convergence behavior of ptychographic reconstructions, a momentum-accelerated PIE algorithm (mPIE) was introduced in 2017 [91]. While this algorithm was not used in the results of Ch. 7, the inclusion of momentum acceleration in our angle-reconstruction method was influenced by this method, so we will briefly discuss the properties and advantages of momentum acceleration in optimisation problems that are not strongly convex. Momentum acceleration techniques [98] are inspired by the physical idea of momentum and are a commonly used method to accelerate convergence for gradient descent methods for non-convex problems in machine learning [99]. In momentum-accelerated methods, instead of stepping towards the negative gradient at each step, some velocity v_i builds towards the direction of the negative slope and the algorithm steps with the built-up velocity at each step. For convex optimisation problems it has been shown that Nesterov's accelerated gradient method [100], a form of momentum acceleration which served as the basis for mPIE, is guaranteed to be faster than normal gradient descent. Momentum methods have also shown to have superior initial convergence behavior for non-convex optimisation methods, while showing slower convergence when noise becomes the dominant form of error. While the exact reason to why these methods are superior for non-convex optimisation is still an active field of research [101]. However, some of the benefits of momentum acceleration can be intuitively understood. First, consider a cost-function that has a smooth optimisation landscape containing a saddle-point, such as the one illustrated in Fig. 9 a). In the direction of the inflection point of a) the algorithm can stagnate if the stepsize is too small. While a larger stepsize might enable the candidate solution to step past the inflection point, large stepsizes might make a reconstruction unstable and the optimal stepsize might not be the same in all directions. When the solution is slowly accelerated down the optimisation curve, complete stagnation at inflection points is impossible, even when one starts with a relatively small step-

size. By contrast, near a local or global minimum, the acceleration will average out to zero over many iterations. While second-order gradient methods, such as Newton's method, also take the curvature of the optimisation landscape into account and can potentially find a more accurate update rule, they are also computationally much more expensive to calculate than momentum methods, so that the computational cost per step is much higher. A second situation worth considering to explain the effectiveness of momentum acceleration on non-convex problems is a landscape that is approximately convex on a large scale, but locally rough, such as the one illustrated in Fig. 9 b). In such a landscape, momentum acceleration will enable the update to overcome areas where the roughness of the optimisation landscape gradient makes any local gradient a poor estimate of the direction to the global minimum, while the convexity on a larger scale makes the step-averaged gradient a better estimate for the right direction towards the minimum, at the cost of a higher likeliness to overshoot the global minimum. Finally, stochastic gradients only approximate the global gradient based on the sum of the gradient steps of separate batches containing only a subset of the data. As the optimal update direction is only inferred from a subset from the data it is bound to be sub-optimal, and the averaged gradient over multiple sub-datasets gives a better estimate on the proper downward direction of the slope, as compared to the gradient of any individual sub-dataset.

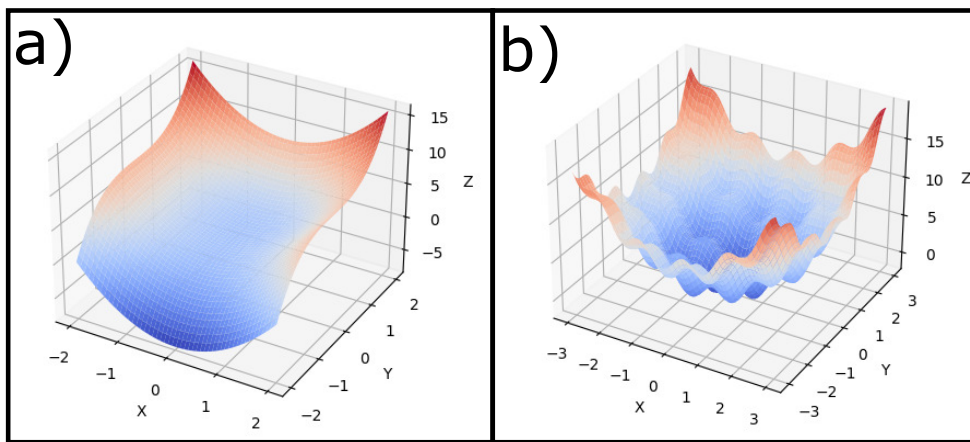


Figure 9: Illustration of example of potential optimisation landscapes that might benefit from momentum acceleration. a) shows part of a saddle point-like optimisation landscape. b) shows an almost convex optimisation landscape that is locally rough.

3.4 SPECTRALLY RESOLVED IMAGING THROUGH FOURIER-TRANSFORM SPECTROSCOPY

Conventional CDI methods have stringent temporal coherence requirements on the illumination source, which is discussed in more detail in Sec. 3.5.2. Typically this has the consequence that intrinsically broadband sources such as those provided by HHG or synchrotrons require a high degree of spectral filtering. In the work described in Ch. 5 and Ch. 6, spectrally resolved diffraction signals are obtained from a pair of phase-locked broadband harmonic sources. Through separation of the signal in different spectral components, the spectral coherence requirements are met without the requirement of spectral filtering, as long as the spectral sampling density is sufficient. In this method, the time delay of these phase-locked HHG sources is scanned, while recording intensities on the camera. Then, a temporal Fourier transformation is used to separate different spectral components, as described in more detail in Sec. 4.3. Here we will discuss the two reconstruction methods that were used to generate images from these signals from this signal: Diffractive shear interferometry (DSI) and an adjusted form of Fourier holography (FTS-FH). These methods bear a strong conceptual resemblance to a hyper-spectral imaging approach from astronomy called double Fourier-interferometry [60, 102], in which Fourier-transform spectroscopy (FTS) is applied on the signal from different radio or infrared baseline telescopes, which results in a signal that is similar to the one we obtain in our experiments.

Consider two illumination beams, which are propagating from two high-harmonic sources S_1 and S_2 , that scatter from a specimen towards a detector in the far field. This situation is illustrated in Fig. 10 a). As both sources are in the far-field of the specimen, it can be assumed that at the sample plane, the difference in phase curvature between these beams is negligible over the size of the specimen. Furthermore, it will be assumed that the amplitude profile at the specimen of the beams only differ by a constant factor c . The assumption that the phase relationship between the two beams is linear at the far-field conditions of our experiments is supported by the observation that the unscattered beams produce straight line fringes when they interfere at the detector. Under these assumptions the 2D probe functions of one beam P_2 at the sample can be written as a function of the probe function of the other beam P_1 , which leads to the following expression,

$$P_2(\boldsymbol{\rho}, \omega) = cP_1(\boldsymbol{\rho}, \omega)e^{i(\Delta\mathbf{k}_\rho(\omega) \cdot \boldsymbol{\rho} - \omega\tau)}, \quad (45)$$

where τ is the time delay between the pulses, ω is the optical frequency of the field, $\Delta\mathbf{k}_\rho(\omega)$ is the difference of the k-vectors of the two beams.

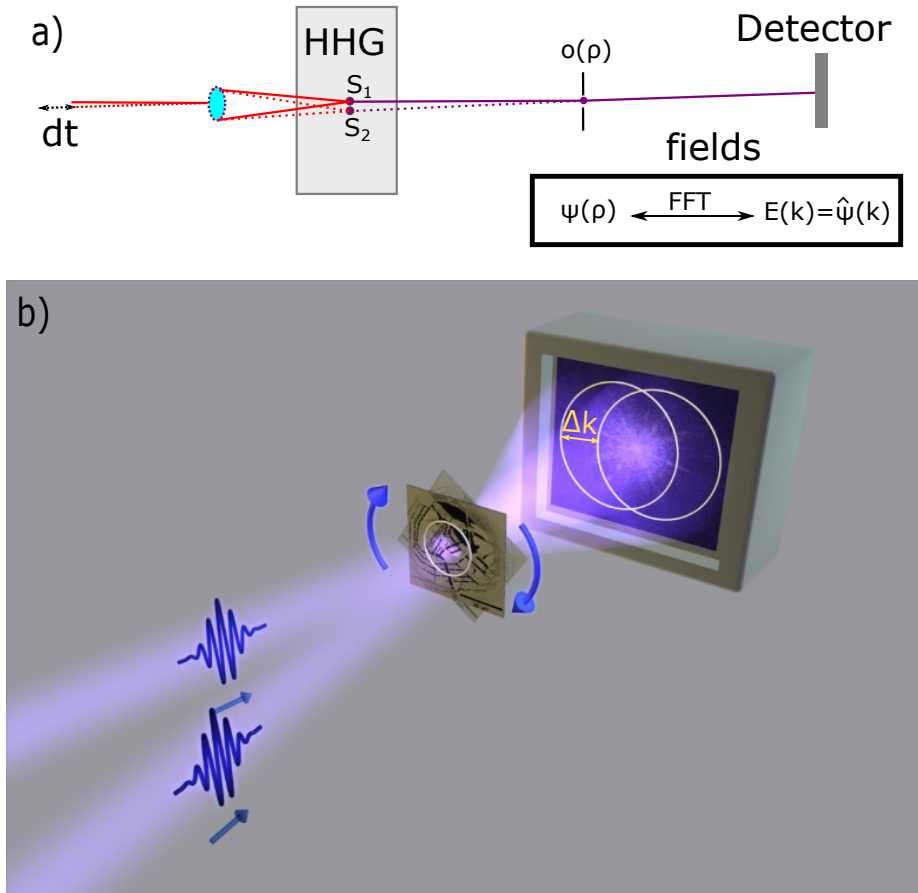


Figure 10: Geometry of DSI experiments with high harmonic illumination.

a) A pair of infrared sources is focused into a gas jet and generate harmonics at source points S_1 and S_2 . Two harmonic beams diverge from these source points and propagate to the object (o) located in the 2D object plane with coordinates ρ . After the beams scatter from the object, the exit wave (ψ) propagates to a detector in the far field, where the field $E(k)$ is expressed in spatial frequencies k .

b) 3D illustration of sheared diffraction patterns at the detector, the difference in the incidence angles of the two beams causes a lateral shear Δk between their Fourier-components at the detector in the far-field.

Finally, as in most forms of CDI (Eq. 34), a thin sample assumption will be used, so that the exit wave can be described by the multiplication of the sum of the 2D probe function and a 2D object function $o(\boldsymbol{\rho})$.

This enables us to express the total two pulse exit wave as follows,

$$\psi(\boldsymbol{\rho}, \tau) = \psi_1(\boldsymbol{\rho}, \tau) + \psi_2(\boldsymbol{\rho}, \tau) \quad (46)$$

$$= P_1(\boldsymbol{\rho}, \tau) o(\boldsymbol{\rho}) \left[1 + c e^{i(\Delta \mathbf{k}_\rho \cdot \boldsymbol{\rho} - \omega \tau)} \right]. \quad (47)$$

When this exit wave is propagated to a far-field detector plane by Fourier transformation (by using Fourier-shift theorem), we obtain the following detector-space intensities,

$$I_\tau(\mathbf{k}) = |\psi(\mathbf{k}, \tau)|^2 \quad (48)$$

$$= |E_1(\mathbf{k})|^2 + |c|^2 |E_1(\mathbf{k} + \Delta \mathbf{k}_\rho)|^2 + c E_1(\mathbf{k})^* E_1(\mathbf{k} + \Delta \mathbf{k}_\rho) e^{-i\omega \tau} + cc, \quad (49)$$

where \mathbf{k} are the spatial frequencies of the specimen and the far-field electric field of a single beam $E_1(\mathbf{k})$ is the Fourier transform of $\psi_1(\mathbf{k}, \tau)$. In what follows, we will use the electric field as a shorthand for the detector space (=Fourier space) electric field of a single beam $E_1(\mathbf{k})$, unless specifically stated otherwise.

So far we have only considered the detector intensities for a monochromatic source pair. However, for multiple wavelengths the total intensity signal is the incoherent sum of the intensity signals of all harmonics (see Sec 3.5.2). In DSI measurements, these intensities are recorded while scanning the time delay between the two sources. Then, by means of a temporal Fourier transformation, the measured intensity is expanded into time-delay frequency components. Apart from the time-delay-independent D.C. terms, which contains an incoherent sum over all wavelengths, this separates the signal in separate spectral components and results in the following complex signal for a harmonic with optical frequency ω :

$$M_\omega(\mathbf{k}) = E(\mathbf{k})^* E(\mathbf{k} + \Delta \mathbf{k}_\rho). \quad (50)$$

We use this quantity as a Fourier-space measurement constraint in our reconstructions.

Note that the challenges to finding a solution to this inverse problem are different from cCDI, in which the field is reconstructed from its absolute value $|\hat{\psi}_1(\mathbf{k})|$. Unlike in cCDI, the far-field amplitudes of the field can not be uniquely determined from the measurement signal alone as the signal from Eq. 50 only contains information about the ratios between amplitudes of the field at different spatial frequencies. It was shown by one of our collaborators from the technical university of Delft [103] that for any measurement with a single shear

and no priors, the solution is non-unique, when a solution is multiplied with a function that is periodic with two times the shear another solution is generated. However, while some information about the far-field amplitudes is lost, phase information obtained through the interferometry is present in the signal of Eq. 50, via:

$$\phi_M = \frac{M_\omega(\mathbf{k})}{|M_\omega(\mathbf{k})|} = e^{i[\phi(\mathbf{k}) - \phi(\mathbf{k} + \Delta\mathbf{k}_\rho)]}. \quad (51)$$

Here, $\phi(\mathbf{k})$ is the phase function of the electric field. While the phase function that satisfies Eq.51 is not unique, it does put a constraint on the possible solutions of the phase function of the field: For any solution to the measurement constraint, the integral of the phase gradient of the solution over the shear must match the phase difference measured at that shear:

$$\int_{\mathbf{k}}^{\mathbf{k} + \Delta\mathbf{k}} \nabla\phi(\mathbf{k}')d\mathbf{k}' = \phi(\mathbf{k}) - \phi(\mathbf{k} + \Delta\mathbf{k}) = \phi_M(\mathbf{k}). \quad (52)$$

This puts an additional constraint on candidate solutions. For example the phase conjugate of a solution is not typically a solution of the measurement constraint in DSI. By contrast, in single-shot CDI the phase-conjugated field is always a solution of the measurement constraint, and while this solution is only different in a trivial way (a mirrored object in object space) and the choice of the sign of the phase in DSI is arbitrary, reconstructions will often stagnate in between these two solutions in CDI, while they tend to prefer one orientation in DSI. Note that measurements that only use a single shear vector are insensitive to phase gradients perpendicular to the shear vector \mathbf{k} .

3.4.1 Diffractive shear Interferometry

Based on this measurement signal M we developed a CDI-like iterative optimisation scheme described in Ch. 5. Dividing the conjugate of the measurement M^* by a possible solution $E(\mathbf{k})$ results in a laterally shifted and conjugated version of a solution for the exit wave. Similarly, the ratio M/E^* will lead to a new guess for the sheared version of E . To avoid overshooting issues, a symmetrised and regularised update function is implemented that uses the following update step in Fourier space:

$$E_{n+1}(\mathbf{k}) = (1 - \beta)E_n(\mathbf{k}) + \frac{\beta}{2} \left[\frac{M(\mathbf{k} - \frac{\Delta\mathbf{k}}{2})E_n(\mathbf{k} - \Delta\mathbf{k})}{|E_n(\mathbf{k} - \Delta\mathbf{k})|^2 + \alpha^2} + \frac{M^*(\mathbf{k} + \frac{\Delta\mathbf{k}}{2})E_n(\mathbf{k} + \Delta\mathbf{k})}{|E_n(\mathbf{k} + \Delta\mathbf{k})|^2 + \alpha^2} \right]. \quad (53)$$

Where $E_n(\mathbf{k})$ is the n -th guess for $\hat{\psi}(\mathbf{k})$, β is a parameter between 0 and 1 that mixes in the input estimate with the update. Note that in the article $d\mathbf{k}$ denotes the half shear, while $\Delta\mathbf{k}$ denotes the full shear here. More details are given in Ch. 5

3.4.2 FTS-Fourier Holography

In the FTS-FH experiments, a pinhole in the specimen plane produces a reference beam (R) for the object of interest (O). The field of source S_1 at the detector is given by the Fourier transformation of its exit wave,

$$\hat{\psi}_1(\mathbf{k}) = [\hat{O}(\mathbf{k}) + \hat{R}(\mathbf{k})]. \quad (54)$$

Where O and R are the exit waves of the pinholes and the specimen respectively. This relationship can be combined with Eq. 50 to obtain the following expression for the DSI signal,

$$\begin{aligned} M_\omega(\mathbf{k}) = & \hat{O}(\mathbf{k})\hat{O}^*(\mathbf{k} + \Delta\mathbf{k}) + \hat{R}(\mathbf{k})\hat{R}^*(\mathbf{k} + \Delta\mathbf{k}) + \\ & \hat{O}(\mathbf{k})\hat{R}^*(\mathbf{k} + \Delta\mathbf{k}) + \hat{R}(\mathbf{k})\hat{O}^*(\mathbf{k} + \Delta\mathbf{k}). \end{aligned} \quad (55)$$

And, after 2D spatial Fourier transformation of the signal:

$$\begin{aligned} \hat{M}_\omega(\boldsymbol{\rho}) = & O(\boldsymbol{\rho}) \otimes O^*(\boldsymbol{\rho}) e^{i\Delta\mathbf{k}_\rho \cdot \boldsymbol{\rho}} + R(\boldsymbol{\rho}) \otimes R^*(\boldsymbol{\rho}) e^{i\Delta\mathbf{k}_\rho \cdot \boldsymbol{\rho}} + \\ & \hat{O}(\boldsymbol{\rho}) \otimes \hat{R}^*(\boldsymbol{\rho}) e^{i\Delta\mathbf{k}_\rho \cdot \boldsymbol{\rho}} + \hat{R}(\boldsymbol{\rho}) \otimes \hat{O}^*(\boldsymbol{\rho}) e^{i\Delta\mathbf{k}_\rho \cdot \boldsymbol{\rho}}. \end{aligned} \quad (56)$$

Aside from a convolution with a linear phase ramp for each of the terms, this expression is identical to the object space autocorrelation signal one would obtain in an ordinary FTH experiment. The effect of this convolution on the cross correlation terms, which are used to obtain an image in FTH imaging, can be reasonably approximated with a multiplication with a linear phase-ramp or even a constant phase offset as long as the spatial extent of the reference pinhole is limited.

3.5 COHERENCE AND SAMPLING REQUIREMENTS IN DIFFRACTIVE IMAGING

In this section the requirements on coherence and sampling in diffractive imaging experiments will be briefly described.

3.5.1 Sampling Requirements

The argument, which was made by Bates [78], that solutions for the phase problem for imaging of objects with a finite support are essentially unique aside from trivial object flips or displacement depends on a Nyquist sampling rate of the spatial frequencies present in the detector intensity signal. Consider the situation of Fig. 11, in which an incident plane wave scatters from an object of width W , to a detector at a far-field plane at a distance Z to detector pixels that are spaced with a detector pixel size Δx . The fastest fringes on the detector are due to the interference between the waves that scatter from

the object with the largest difference in scattering angle, from waves that are scattering from the edges of the object. The difference in angle α between such waves (assuming a paraxial approximation) is equal to W/Z [104]. Which will lead to interference fringes with a period of $\lambda/\alpha = \lambda Z/W$. The Nyquist requirement of at least two sample points per period results in a maximum detector pixel spacing $\Delta x < 2\lambda/\alpha = \lambda Z/W$.

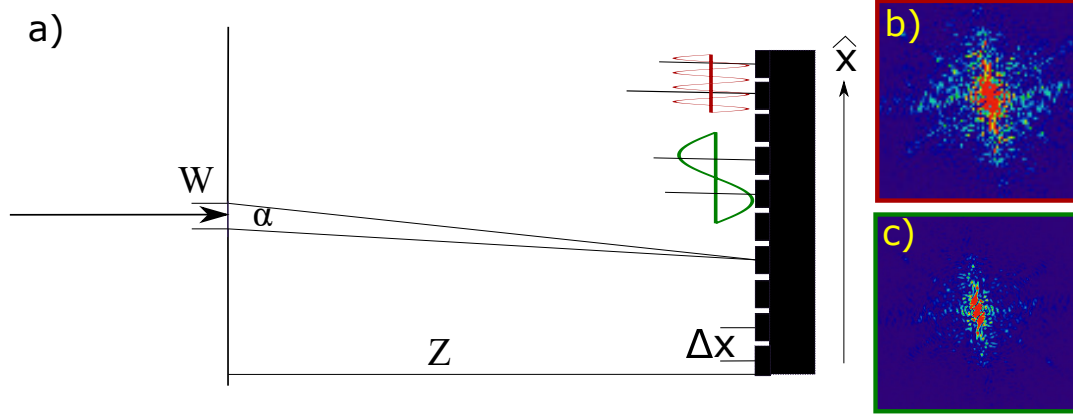


Figure 11: Illustration of sampling requirements in CDI. a) A diffraction pattern is sampled with a sampling density Δx , determined by the pixel size. In order to properly reconstruct the fields, it is required that this density at least matches the Nyquist frequency of the spatial fringes. So that the fastest fringes, generated by those points of the transmitting part of the object that are maximally separated (by width W), are sampled at least twice per period. The green sine function on the top right of the subfigure illustrates a well sampled signal, while the red sine illustrates a insufficiently sampled signal, b) and c) illustrate a undersampled and a sufficiently sampled diffraction pattern, respectively.

In pCDI, the sampling-density requirements for the individual diffraction patterns are not as strict as in the cCDI case. For ptychographic data sets, it has been shown that each scan position probes a different set of Nyquist sampling points, so that the combined data set can be Nyquist sampled even if individual diffraction patterns are significantly under-sampled, as long as the product of the object-space and Fourier-space sampling points satisfy Nyquist sampling [105].

In support-constraint based DSI (see Ch. 5), the measured signal can be described as $\hat{\psi}(\mathbf{k})\hat{\psi}(\mathbf{k} + \mathbf{dk})^*$. As with intensity-based signals in CDI, the fastest oscillations in $\hat{\psi}(\mathbf{k})$ will result in a signal that oscillates with twice the frequency of the field, so that the signal requires identical sampling conditions to the cCDI case for proper sampling. However, for rotational DSI, different rotational orientations sample different combinations of spatial frequencies, so that it can be argued that the minimum sampling requirements for each individual diffraction pattern are reduced similarly to the reduction of the sampling requirement in ptychography.

3.5.2 Coherence requirements

So far, in the sections about cCDI and pCDI, we have assumed that the detector intensity can be uniquely described as the propagation of a single instantaneous 2D monochromatic field at the object. However, the measured intensity signal is a time-averaged quantity and it is not guaranteed that the detector signal can be uniquely described with only a single non-averaged field distribution. This is only possible if the spatial oscillations of the instantaneous field are uniform, which depends on the temporal and spatial *coherence* properties of the illumination source. For temporally incoherent sources, such as random emitters and broadband sources, the time-integrated intensities do not have a linear relationship with the instantaneous intensities as the interference cross-terms between different spectral components average out on timescales longer than the coherence time $\tau = \frac{\lambda^2}{c\Delta\lambda}$. Instead, for such sources, the intensities can only be described with partial coherence theory, either through coherence functions [106] or as the time-averaged incoherent sum of monochromatic modes [107]. Sometimes, for the highly diverse data sets from pCDI, it is possible to reconstruct separate fields at different wavelengths using diffraction theory by modelling it as a mutually incoherent sum of coherent spectral modes [28, 29]. However, this leads to a dramatic increase the number of model parameters that need to be solved, and therefore typically requires strong priors about the sample and/or the illumination and a high sampling density in real space. The work in Ch. 5 and 6 explores an alternative solution that uses Fourier-transform spectroscopy to digitally separate the different spectral components before reconstruction. Even for mostly temporally coherent sources it is useful to consider up to what threshold objects can still be reconstructed with cCDI without appreciable reduction in obtainable resolution. One factor to consider for such sources is the wavelength dependence in the propagation direction of angular spectrum components (see Eq. 9). When the spectrum of the illumination of a sample shifts from monochromatic at frequency ν to a frequency band $\pm\Delta\nu$, the range of spatial frequencies of the object field scattering at a specific angle spreads from $k = \nu/c$ to $k \pm \Delta k$, where $\Delta k = (\Delta\nu)/c$. For insufficiently coherent illumination sources, the spatial fringes of the object are no longer distinguishable, so that it is no longer possible to reconstruct these fringes through standard cCDI methods. However, as long as the longitudinal coherence length $L_c = c/(2\pi\Delta\nu)$ of the illumination exceeds the maximum path length difference of rays scattering from the object to the detector, this blurring effect is small enough for the interference maxima of the fastest spatial frequencies to remain distinguishable. For a source field that can be described as

a plane wave, this results in the following minimum requirement for temporal coherence in cCDI:

$$\frac{c}{\pi\Delta\nu} > \lambda W/L * x_{\max} \quad (57)$$

A second factor to consider are spatial coherence requirements. For spatially incoherent (=spatially extended) sources, the inverse problem can become non unique if the spread in incidence angles towards the sample can no longer be distinguished from differences in the scattering angles from the sample normal. Spence [18] has argued that for CDI, the scattering angles from the sample can be uniquely identified from the diffraction pattern in cCDI, as long as the illumination beam stays in phase over twice the area of the object to satisfy the two-times oversampling requirement, or that the coherence width $X_c \approx \lambda/\theta_c > 2W$, where θ_c is the spread of angles in the illumination.

EXTREME ULTRAVIOLET LASER SYSTEM AND IMAGING SETUPS

This chapter contains a more detailed description of the laser system used for the diffractive shear interferometry (DSI) experiments described in Chapter 5 and Chapter 6. These experiments were performed using extreme-ultraviolet pulse pairs generated through up-conversion of infrared photons through high-harmonic generation (HHG).

In order to enable the high peak powers required for this highly non-linear process, femtosecond near-infrared pulses generated by a Titanium-sapphire oscillator (Ti:Sa) are amplified from a few nJ to several mJ through non-collinear optical parametric chirped-pulse amplification (NOPCPA) [108]. In this non-linear process, energy is transferred from picosecond pump photons into photons with the properties of the seed. After compression, these fs pulses are split into pulse pairs with a tunable time delay by a common-path interferometer. Next, both these pulses are focused inside a gas jet to generate high harmonics of the driving laser, which are finally used as illumination for our imaging setup.

A schematic overview of the experimental setups described in this chapter is shown in Fig. 12.

The laser and amplification system for these experiments will be described in Sec. 4.2, the vacuum setup and high harmonic generation setups are described in Sec. 4.3, and finally the imaging setups in Sec. 4.4.

Before discussing the experimental aspects, some of the physics behind high-harmonic generation is discussed in Sec. 4.1. A semi-classical picture is used to explain some of the basic physics. Then, phase matching considerations, are discussed in Sec. 4.1.2.

4.1 THE HIGH-HARMONIC GENERATION PROCESS

4.1.1 *Three-step model*

High-harmonic generation occurs in the strong-field regime, where the magnitude of the optical electric field is significant compared to the Coulomb potential between particles in the atom. In this regime, the induced dipole moment of the electron can no longer be accurately described as a perturbative series of the fundamental field, as is common in traditional non-linear optics. Instead, these high harmonics arise from the contribution to the radiating dipole emission

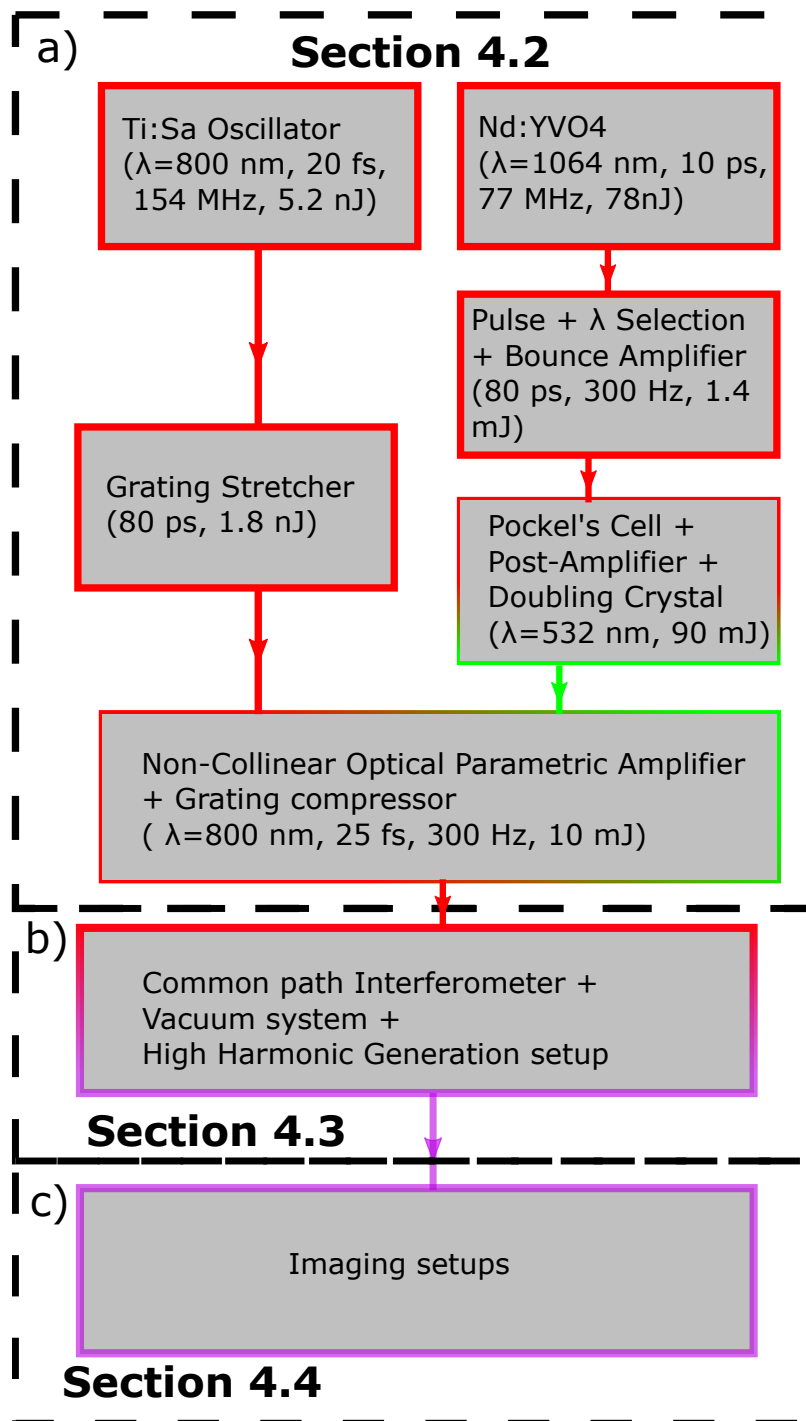


Figure 12: Schematic overview of the experimental setups described in this chapter. a) Laser system, the numbers given in the parentheses show changes in key parameters at the output for different stages. b) vacuum setup and generation of extreme-ultraviolet pulse pairs. c) imaging setup.

of those quantum paths in which the electron tunnels out of the Coulomb potential to continuum states, interacts with the field, and recombines with the atom. As only a part of the electron wavepacket tunnels out, the electron is never actually fully ionised. Surprisingly, despite the intrinsically quantum-mechanical nature of tunneling, a quasi-classical model can still be used to provide an intuitive picture on many aspects of their physical behaviour. This three-step model, which was proposed in 1993 [109], is shown schematically in Fig. 13. This model describes the process in the following parts: In the first

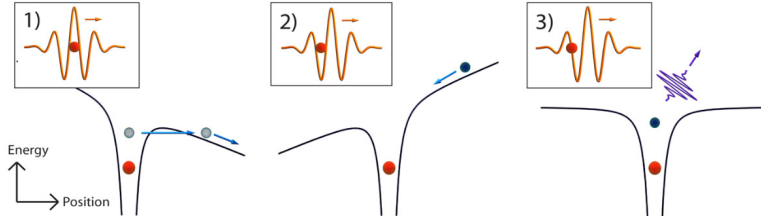


Figure 13: Three-step model of high harmonic generation. 1) The Coulomb potential of the atom is altered due to the influence of high intensity pulses, increasing the tunnel ionisation cross-section. After ionisation, the electron accelerates away from the nucleus until the electric field changes sign. 2) After being decelerated, the electron is accelerated back by the field of the laser, gaining kinetic energy. 3) The electron re-collides with the nucleus, releasing all kinetic and potential energy it gained through emission of a high energy photon.

step, an electron is removed from the atom through tunnel ionisation at some time τ_{start} . The cross-section of this tunnel-ionisation step is calculated using results from tunnel ionisation models. Then, in the second step, this electron is treated like a free particle that interacts classically with field of the driving laser, while the attractive force of the ion is neglected due to the strong-field conditions. In the third step the particle collides and recombines with the atom, after the field changes sign. Then photons are emitted with an energy that is the sum of its ionisation energy and the kinetic energy gained in the field. From the equations of motion, the energy of the emitted photon can be derived:

$$E_{\text{photon}} = I_p + 2U_p[\sin(\omega_0(\tau_{\text{start}})) - \sin(\omega_0(\tau_R))]. \quad (58)$$

Here E_{photon} is the energy of the emitted photon, I_p is ionisation potential of the atom, ω is the frequency of the optical field, and $U_p = \frac{(eE_0)^2}{4m\omega^2}$ is the ponderomotive energy.

As the recombination cross-section is only significant at any time the electron is close to its nucleus, it's possible to find the following expression (from Eq. 58) for a cutoff that sets an approximate limit on the energy of the photons:

$$E_{\text{cutoff}} \approx I_p + 3.17U_p \quad (59)$$

This prediction for the energy cut-off differs from the result of a full quantum-mechanical strong-field treatment, developed by Lewenstein [110] in 1994, only by the slope of its dependency on the ionisation potential.

4.1.2 Phase matching for HHG

Phase matching plays an important role for the efficiency of any process that uses non-linear optics to generate new wavelengths. Only if photons that are generated at different spots along the propagation direction of the generating beam interfere constructively can these processes be efficient. In non-linear crystals, such as those that are used for frequency doubling, birefringence is often used to compensate for the dispersion-induced mismatch in phase velocity between generated photons and the incident wave. For HHG in gasses, due to the lack of axial symmetry-breaking induced by the crystal structure, other processes have to be used to match the phase velocity, or equivalently the wave vectors, of the generated HHG beam with the fundamental beam. There are four main contributing factors to the phase matching of harmonics in a noble gas.

The first two terms arise as a wave-vector mismatch between the high harmonics and the fundamental beam due to dispersion in the medium. A positive dispersion term from the neutral noble gas atoms and a negative dispersion term from the plasma, as, inevitably, a significant fraction of the atoms will be ionised. The total wave-vector mismatch due to dispersion is given by (from [111]),

$$\Delta k_{\text{dispersion}} = qP \left([n(\omega_0) - n(\omega_q)][1 - \eta] - \eta \frac{0.1\lambda_0\tau\mu_0 e^2}{4\pi m_e k_b T} \right), \quad (60)$$

here q is the harmonic order, P is the pressure, $n(\omega_q)$ is the refractive index at frequency of the q -th harmonic, ω_0 and λ_0 are, respectively, the frequency and wavelengths of the driving laser, η is the ionisation fraction of the gas, T is the temperature of the free electrons, and m_e is the electron mass. A third factor arises due to the phase accumulated by the electron wavepacket over its trajectory, which is given by [111]:

$$\Delta k_{\text{dipole}} = \alpha \nabla I, \quad (61)$$

where α is a value dependent on the quantum trajectory. In tight focusing conditions, the geometric Gouy phase gives rise to a last significant phase mismatch contribution, as a Gaussian beam near its focal plane $z = 0$ acquires a π phase shift compared to a plane wave as it moves across the focus from $z = -\infty$ to $z = \infty$. This Gouy phase of a Gaussian beam is given by,

$$\phi_{\text{Gouy}}(z) = -\arctan(z/z_R), \quad (62)$$

where z_R is the Rayleigh range of the beam. For the low divergence XUV beam the Gouy phase shift is small enough to be neglected over the axial extent of the medium. In order to maximise the high-harmonic generation efficiency, the task is then to minimise the total wave-vector mismatch Δk , which is given by,

$$\Delta k = \Delta k_{\text{dispersion}} + \frac{\Delta\phi_{\text{Gouy}}(z)}{\Delta z} + \Delta k_{\text{dipole}}. \quad (63)$$

As the dispersion terms of Eq. 60 are linearly dependent on the pressure, while the other two terms are pressure independent, tuning the pressure enables experimental control of the relative strength of the dispersion term with respect to the dipole and geometric terms. Additionally, the phase-matching conditions can be tuned by changing the focal position: In the axial direction, the intensity gradient changes from positive values before the focus to negative values after the focus. By changing the position of the focus from one side of the interaction region to the other, the sign of the intensity gradient in the medium can be flipped, causing the dipole phase term to change sign, or if the focus is placed near the middle of interaction region, it will cause the dipole phase term acquired over the interaction region to become negligible. Tuning the distance between the focal spot and the interaction region controls the magnitude of Gouy wave-vector mismatch, as the derivative of the Gouy phase decreases as the distance between the interaction zone and the focal distance increases. Finally, the intensity of the driving laser influences the phase-matching conditions, as it changes the strength of the dipole and ion dispersion terms with respect to the neutral atom dispersion. The intensity in the interaction region can be experimentally tuned by changing the focusing conditions in the medium or by changing the strength of the driving laser. If the driving laser intensity gets too high, the ionisation fraction might exceed a critical threshold, for which it will no longer be possible to achieve phase matching [45] between the negative Gouy and plasma dispersions and the positive neutral atom dispersion. With proper phase matching, the divergence of the generated harmonics is typically far below the divergence of fundamental laser.

4.2 LASER AND AMPLIFICATION SYSTEM

4.2.1 *The Ti:Sa oscillator seed laser system*

Passive mode locking in Titanium-doped Sapphire (Ti:Sa) crystals was first demonstrated in 1991 [112]. Since this discovery, Ti:Sa has been a ubiquitous gain material for generating ultrafast pulses as these crystals combine good heat-conduction properties, and a high damage threshold with a large gain bandwidth (230 nm FWHM) of

the Ti^{3+} [113] ion. This large gain bandwidth, shown in Fig. 14 a), enables typical pulse lengths ranging from 100 fs down to a minimum of about 5 fs [114], depending primarily on dispersion control. Ti:Sa crystals have a wide absorption peak around 490 nm [115], and are traditionally pumped with argon lasers or frequency doubled green light generated in Nd-doped lasing materials [113, 116]. Although more compact, directly diode-pumped Ti:Sa lasers have also become available in recent years [116, 117]. Mode locking is enabled through the optical Kerr effect [118] in the crystal. This is a nonlinear effect in which the beam induces an intensity-dependent change of the refractive index of the medium that, with a typical intensity profile of a Gaussian beam, will lead to self focusing [119]. If the continuous-wave mode experiences losses due to aperture effects, the stronger self-focusing effects of the higher intensity pulsed mode can make mode-locked operation out-compete single-mode operation. To keep the pulses short in the crystal, and thus maintain the lower losses for the pulsed mode, the laser cavity dispersion is compensated through the use of chirped mirrors [120, 121]. One of the end mirrors in the crystal is held by a piezo-controlled mirror mount that is able to adjust the cavity size. As the repetition rate of the output is determined by the travel time of the pulse for a single round-trip, this enables synchronising its repetition rate to that of the pump laser. Roughly 5% of the output is split off to monitor the spectrum, and to synchronise the laser frequency with the pump laser. In modelocked operation our Ti:Sa laser emits a spectrum with a FWHM bandwidth of approximately 100 nm around a central wavelength of 800 nm (a typical output spectrum of the oscillator is shown in Fig. 15). The oscillator system generates 6-7 nJ pulses with a fs pulse length, at a repetition rate of 154 MHz.

4.2.2 *The Nd:YAG pump laser system*

The pump laser system delivers 90 mJ, 80 ps at 532 nm pulses, with a repetition rate of 300 Hz as a pump beam for parametric amplification. The seed for this pump laser system is a SESAM-modelocked vanadate oscillator (Nd:YVO_4) that generates 10 ps pulses around a center wavelength of 1064 nm light, with a repetition rate of 77.8 MHz.

A photo diode at the output of the oscillator is connected to a delay generator (DG645, Stanford Research systems). This delay generator divides the oscillator signal to 300 Hz and sends out triggers to synchronise all parts of the experiment. Part of the photo diode signal is split off to lock the frequency of the Ti:Sa oscillator output to the Nd:YVO_4 oscillator frequency by a proportional-integral-derivative (PID) controller that can adjust the cavity length of the Ti:Sa oscillator through the previously mentioned piezo-controlled mirror mount.

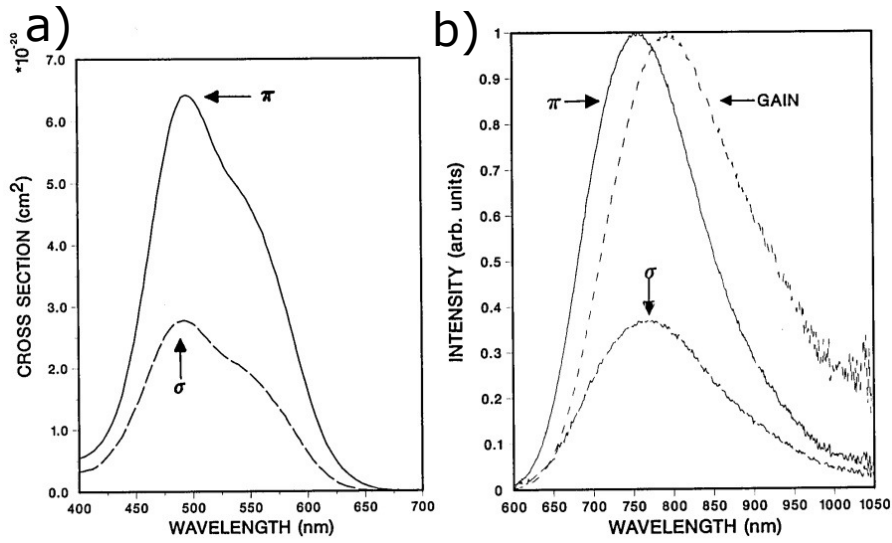


Figure 14: absorption (a) and gain spectra (b) of Titanium-Sapphire (Ti:AL₂O₃), taken from [122].

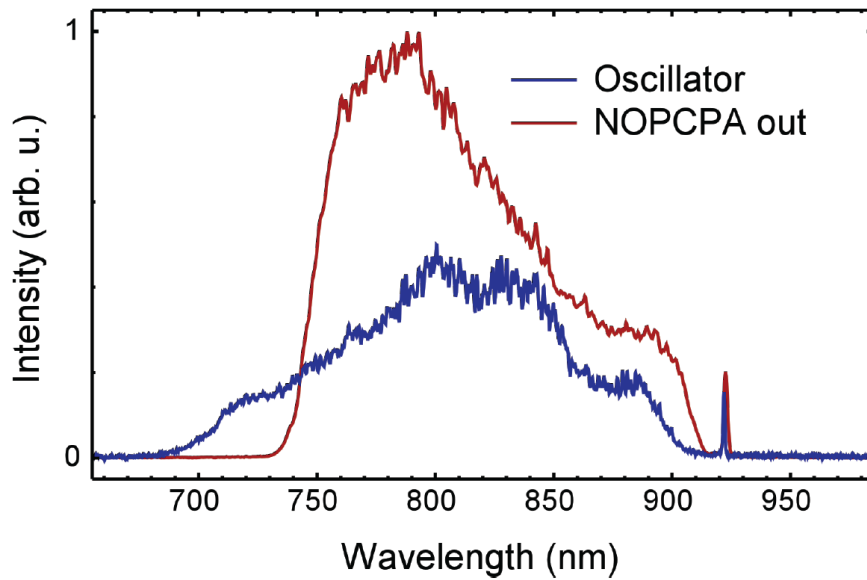


Figure 15: Typical spectra for the Ti:Sa oscillator(red) and after parametric amplification(blue).

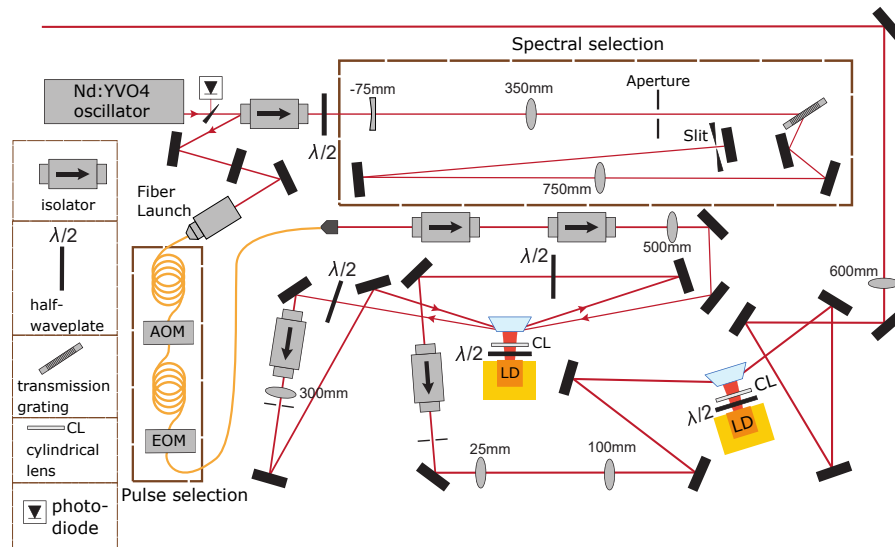


Figure 16: Schematic overview of the bounce amplifier and seeding oscillator to illustrate spectral selection through the 4f-grating-system, pulse selection through an acousto-optical modulator (AOM) and a electro-optical modulator (EOM), and amplification by grazing incidence passes through a pair of Nd:YVO₄ crystals, QCW pumped by laser diodes (LD). After collimation to 1 mm, the beam continues to a Pockels Cell.

These 1064 nm pump pulses are amplified through two amplification stages. The first of these two stages, is a grazing-incidence or bounce amplifier, with a design based on a system developed by our colleagues at the Vrije Universiteit [123]. This amplification scheme enables an extremely high single- or double-pass gain, through a geometry that combines internal reflection of the beam at the surface of a Nd:YVO₄ crystals with a slab geometry, side-pumped from one side with an array of high peak-power quasi continuous-wave pump diodes. Normally, the main disadvantage of such a pumping geometry is the spatially strongly inhomogeneous gain profile. However, in a grazing-incidence reflection geometry, the effect of the spatially inhomogeneous gain on the beam profile before reflection is compensated upon reflection. In this geometry, the beam experiences a very high gain, as it stays close to the pumped surface where the gain factor is the highest [124]. A schematic drawing of this amplifier system is shown in Fig. 16. First, the spectrum out of the seed oscillator is clipped using a combination of 4f-grating-system that disperses the spectral components spatially, while a slit near the Fourier plane of the 4f system selects a part of the spectrum. As the position and width are tunable, this enables a controlled way stretching of the pulse length, and thus lowering the peak intensity. This is done to avoid damage in our second Nd:YAG 'post'-amplifier system, and to select an optimal spectrum for gain extraction in the Nd:YAG post-amplifier. After the spectrum is narrowed, as the grating is imaged

onto itself with the 4-f-system, the different spectral components are recombined by a back-pass through the transmission grating, generating pulses with a typical pulse length of 80-90 ps. Then, fiber-coupled pulse-picking devices are used to select and isolate pulses for amplification with a repetition rate of 300 Hz. For this purpose, we use an acousto-optic modulator (AOM), which is an optical switch that is based on diffraction by piezo-transduced sound waves, to select a μs time gate, in combination with a Electro-optic modulator (EOM) to select out individual pulses from that time gate. Then, the light is coupled from the fiber to air and passes through a pair of 3 dB optical isolators to attenuate possible back reflections.

Next, the beam is amplified through two grazing incidence passes through a $2\times 5\times 20\text{ mm}^3$, 1 at.-%-doped Nd:YVO₄ gain module, followed by a single pass through a larger $4\times 6\times 20\text{ mm}^3$ gain module after expansion of the beam. Both modules are side-pumped by output laser diodes in quasi-continuous wave mode run at a current of 130 A and a voltage of 1 V. These modules emit around a wavelength of 880 nm. The polarisation of the light emitted by these diode arrays is rotated by a half-wave plate to match the optical axis of the crystal, while a cylindrical lens is used to collimate the pump beam vertically to respective beam heights of approximately 0.6 m and 1 mm, for the first and second module. These beams pump the crystals to saturated population inversion during 130 ms intervals that match the 300 Hz repetition rate of the pulse selection. Between passes, back-reflections are suppressed by an additional pair of 30 dB optical isolators, while two iris diaphragms reduce the amount of amplified spontaneous emission (ASE) propagating through the system. Otherwise, high levels of ASE might result in gain depletion or damage in later amplification stages.

After amplification in the bounce amplifier, the beam is collimated and sent to a Pockels Cell that, in combination with a half-wave plate and an isolator, acts as an optical switch. Due to some residual elliptical polarisation, a quarter-wave plate was used before the isolator to increase the contrast of the isolator. This optical switch is used as a 10 ns long time gate to further suppress the μs -timescale ASE pedestal with a 30 dB contrast. The Pockels cell has a half-wave voltage of approximately 10-11 kV. In the experiments in Ch. 5, it was run close to half-wave voltage. At some point during the second experiment we experienced electrical breakdown in the Pockel's Cell driver. To avoid such issues in our replacement driver, we limited the operating voltage to 8 kV after the incident. In order to compensate for the loss of transmission through the polariser, the pump current at which the diodes were operated was raised to approximately 135 A. Pulse energies after the isolator were measured with values in a typical range between 0.7 and 1 mJ, while the beam size was approximately 1 mm.

For further amplification, these pulses are sent to the post amplifier system that is depicted in Fig. 17. This system was built by one of my predecessors and is described in more detail in [125]. At this stage, the beam is amplified by a double-pass through a pair Nd:YAG gain modules (REA series by Northrop Grumman). Both of these modules contain a 14.6 mm long cylindrical rod that is side-pumped in quasi-continuous wave operation by five rows of diode bars that are placed around the rod. The first amplification module, which has a rod diameter of 6.3 mm, is operated at 230 V and a peak drive current of 75 A for an interval duration of 240 μ s, while the second module, which has a rod diameter of 10 mm, is driven at voltage of 230 V and a peak drive current of 90 A for an interval duration of 270 μ s. When pumped by the diodes at these high powers, these rods experience thermally induced birefringence as well as thermal lensing. However, a double-pass geometry, based on an approach pioneered by Scott and de Witt in 1971 [126], partially compensates for the depolarisation effects caused by the thermal birefringence, as for each module a Faraday rotator is placed in between the first and second pass that changes the polarisation by 45 degrees, and another 45 degrees after reflection. Thus some of the depolarisation caused by birefringence in the first pass through the module is compensated during the second pass through the module. Thin-film polarisers at the entrance of both modules transmit the beam incident from the previous amplification stages, while they reflect the beam after two passes, as its polarisation has been rotated 90 degrees by the double pass through the Faraday rotator.

For efficient energy extraction inside the rods, a relatively flat cross section of the beam is selected by an aperture with a diameter of 5 mm after expansion of the beam diameter to 12 mm with a telescope. This leaves a remaining pulse energy of about 0.4 mJ and a truncated Gaussian beam profile with an approximately 15% intensity drop off from the center to the edge of the beam. This relatively flat beam profile enables a spatially homogeneous gain profile and maximises energy extraction from the crystal. To avoid damage for sensitive optics due to the strong diffraction caused by the propagation of this top-hat-like beam profile, the beam is relay-imaged throughout the optical system to ensure that the beam is near an image plane of the aperture for all sensitive optics. The intermediate foci of the relay-imaging system after the first module are located inside vacuum tubes, to avoid thermal lensing or plasma generation effects in air. The imaging lenses between the first and the second module act as a telescope to increase the beam diameter to 8 mm in order to extract more energy from the second rod, which has a larger diameter.

The small-signal double-pass gain in the first module is approximately 30 dB, while the small signal double-pass gain in the second

module is approximately 10 dB. Due to the very high gain in these modules, all lenses and glass surfaces are placed at a small angle with respect to the beam path to avoid parasitic lasing from back reflections. While the tilt of the lenses leads to astigmatism in the beam, this is compensated for by tilting lens pairs in orthogonal directions.

After two passes in both modules, the pulse energy has been amplified to typical values of 15 mJ after the first module, and about 150 mJ after the second module. The output beam of the post-amp is imaged on a BBO crystal, where the light is up-converted through frequency doubling to a wavelength of 532 nm, leaving a pulse energy of roughly 100 mJ. The remaining light of the 1064 nm fundamental beam is picked off with a dichroic mirror that is mostly transparent at 532 nm. Most of the fundamental energy is dumped at a beam dump, while a tiny portion was directed to an imaging system for beam diagnostics.

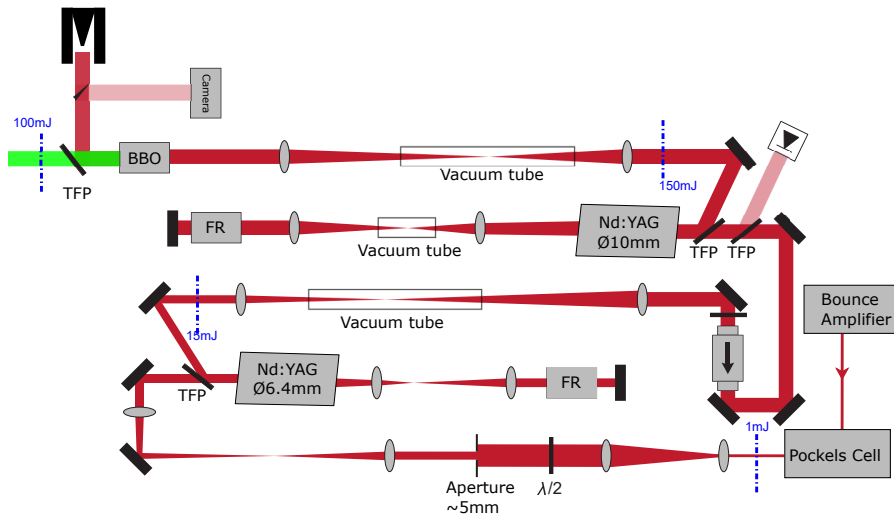


Figure 17: Schematic overview of the post amplifier. The input beam is spatially clipped by a 5 mm aperture and gets amplified through a double-pass through a pair of rod shaped Nd:Yag modules. After these amplification steps, the beam undergoes frequency doubling inside a BBO crystal. The top-hat beam profile at the aperture is relay-imaged onto all normal incidence mirrors, the rods and the BBO crystal. Pulse energies at several locations are indicated in blue. TFP:thin film polariser, FR:Faraday rotator.

4.2.3 The non-collinear optical parametric chirped-pulse amplifier system (OPA)

In the next stage, the 532 nm pump beam described in the previous section, is used to amplify the femtosecond pulses from the Ti:SA oscillator in the non-collinear optical parametric chirped-pulse amplifier (NOPCPA) built by my co-worker Mathijs Jansen [127]. This type of amplifier offers a very high gain over a very large band-

width, which makes them well suited for amplifying the broad spectra required for short pulses [108]. The basis of these amplifiers is a non-linear three-wave-mixing process that is schematically shown in Fig. 19. In this process, pump photons are down-converted through difference frequency generation to signal photons, with the properties of the seed, and to idler photons inside a nonlinear optical crystal (in our case β -BBO). In order to use the picosecond pump pulses to efficiently amplify the femtosecond seed pulses through this parametric process, a good temporal overlap between the two pulses is required. Therefore, a stretcher grating is used to elongate the infrared pulses from 20 fs to several tens of ps by inducing a controlled amount of dispersion. After amplification, a grating compressor compensates for most of the dispersion that is induced by the combination of the stretcher, as well as additional dispersion up to third order from dispersive elements in the optical path such as the BBO-crystals in the OPA, resulting in 25-30 fs output pulses.

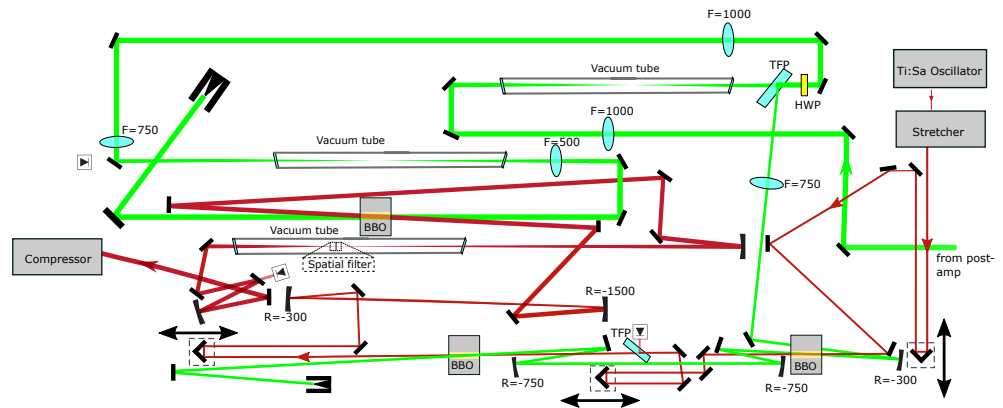


Figure 18: Schematic overview of the parametric amplifier system, in which 532 nm pump photons are effectively converted into signal photons with the properties of the 800 nm seed beam through parametric amplification. The seed beam is amplified from a couple of nJ up to 15 mJ inside three amplification crystals (BBO). The pump beam is split in two arms with a thin film polarizer (TFP), one arm contains the first two amplification stages, while the other arm contains the third stage. Delay stages in the path of the signal beam enable fine tuning of the temporal overlap between the two beams.

To keep the signal and idler photons generated at different positions in direction of the propagation of the pump beam phase-matched, the combined k -vectors of the signal and idler photons inside the crystal should closely match those of the pump photons. While it is possible to use the birefringence of the gain crystal in combination with an appropriate angle θ between the optical axis of the crystal and the pump to enable phase matching in a collinear geometry for a narrow band, the phase-matching bandwidth in such a geometry is limited due to the dispersion in the crystal [108]. By contrast, in a ge-

ometry where the pump and signal beam are non-collinear, the angle between the pump beam and the signal beam offers another knob to tune the phase matching. Using this extra degree of freedom, it has been shown that for β -BBO good phase-matching conditions can be achieved for a broad band of wavelengths, enabling an almost flat gain spectrum between 700 and 1000 nm at a non-collinear angle of $\alpha \approx 2.4^\circ$ [108].

In the experiments described in Ch. 5, we used gold-coated reflection gratings with 600 and 1200 lines per millimeter, respectively, for the stretcher and compressor. Blazed gratings can reach very high efficiencies in their Littrow configurations, in which the incident angle is perpendicular to the step surface. However, the separation of the in going and outgoing beams in a Littrow configuration was impossible due to the combination of small line spacings for the compressor and a designed spatial separation between compressor gratings of only a couple of centimetres. Therefore, the compressor was operated in a non-Littrow configuration, in which the combined efficiency of the compressor grating pair was only 40%. For the work in Ch. 6, we switched to transmission grating pairs with line densities of 1400 lines per mm to improve the efficiency. As the input and output beams are automatically separated for transmission gratings, it was possible to operate these in Littrow configuration. These gratings, which were produced by Lightsmyth, have a high designed diffraction efficiency of over 94% over a broad wavelength range. A more in-depth description of the stretcher compressor configurations can be found in [127]. In the NOCPA amplifier, depicted in Fig. 18, the stretched seed pulses are amplified from in three stages.

As a non-linear amplification medium, 5x5x5 mm BBO crystals are used in the first two stages, while a 10x10x5 mm BBO crystal is used in the final stage. Before the first stage, the pump beam is split into a beam with a pulse energy of 12 mJ for the first two OPA amplification stages and a beam with a pulse energy 78 mJ for the final amplification stage, using a combination of a half-lambda waveplate and a thin-film polarizer. The pump beam at the first two crystals is an image of the top-hat beam at the doubling crystal in the post-amplifier, demagnified by a telescope to roughly 2 mm. Before the beam is amplified at each amplification crystal, a delay stage is used to fine-tune the time-overlap of the pulses of the seed and the pump beam. The BBO crystals are kept at a temperature of 60° to avoid water absorption and are mounted on rotation stages that enable fine-tuning of the phase-matching angle.

At the first two stages, the infrared beam is amplified from a pulse energy of a nJ to roughly a mJ. Then, the infrared beam is expanded to a diameter of about 8 mm, in order to match the size of pump beam at the third crystal. After amplification at the third crystal, the pulse energy is increased to a typical value of 15 mJ. The spectrum after

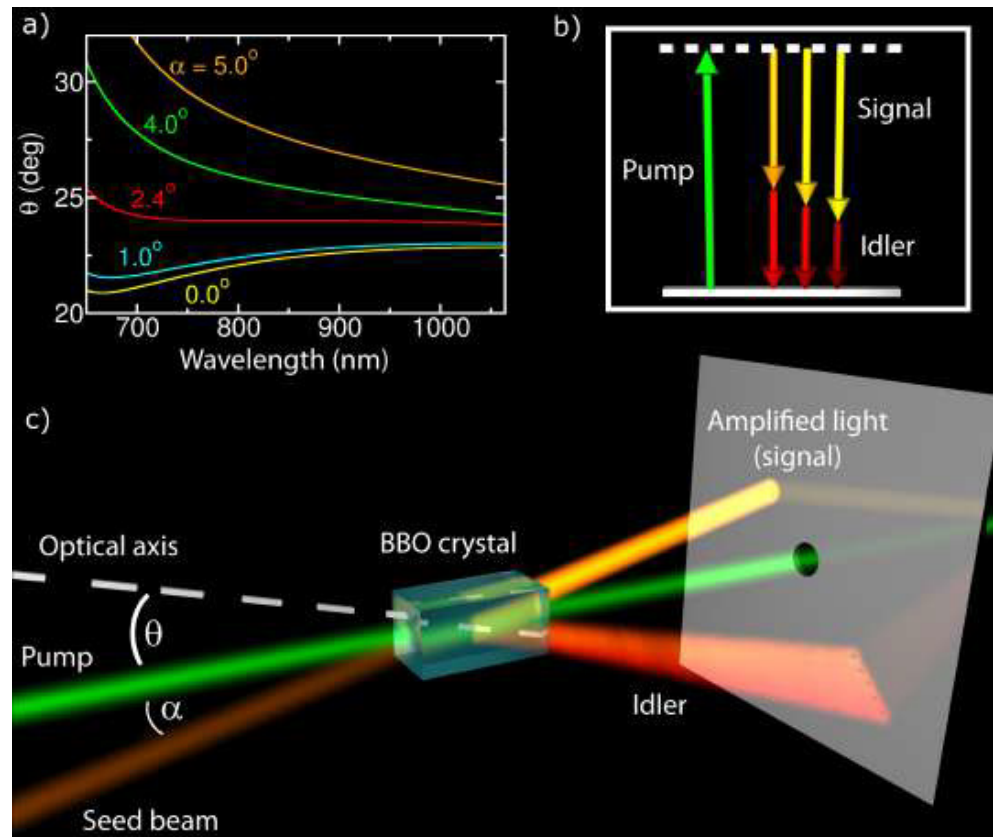


Figure 19: Schematic overview of the non-collinear optical parametric amplification process, taken from [108, 127]. b) In this process 532 nm pump photons are split into signal and idler photons. c) Geometry of the process, α is the non-collinear angle between the pump and the seed beams, θ is the angle between the optical axis and the pump. a) Phase-matching curves. For a non-collinear angle α of 2.4° , phase-matching conditions can be simultaneously achieved for a broad range of wavelengths.

this final amplification stage is shown in red in Fig. 15. After the third stage, a spatial filter was used to clean up the beam profile. This filter consists of a 0.2 mm hole drilled in a 5 mm boron nitride disk that is placed at the focus of a pair of relay-imaging curved mirrors and cuts about 25% of the remaining pulse energy. Finally, the infrared pulses are compressed by the grating compressor to a pulse length of roughly 25 fs, which was measured using frequency-resolved optical gating (FROG) [128]. After compression, the remaining pulse energy was approximately 8 mJ.

4.2.4 *Generating EUV pulse pairs through high-harmonic generation*

In order to generate high harmonics, pulses are focused by a lens ($f = 25$ cm) into a jet of noble gas. This gas jet is produced by a nozzle situated in the vacuum system as depicted in Fig. 20 a). As the pulses are focused about 8 mm from the nozzle, a 1.4 mm thin inner diameter stainless steel tube is used to guide the gas from the nozzle to the interaction region. This tube is intersected by the laser through two holes drilled by the focused beam itself. The experiments are kept at intermediate vacuum conditions to avoid significant reabsorption of harmonics outside of the interaction region by two low-vibration turbo-molecular pumps (Pfeifer HiPace 700) in combination with a scroll pump (Edwards XDS10) with flexible bellows wrapped in vibration-damping foam. Typical pressures during operating conditions were measured to be roughly at 10^{-7} mbar measured near the camera, while the pressure closer to the HHG interaction region was on the order of 10^{-3} mbar during operation, due to the injection of gas in to the vacuum chamber.

A pulsed piezo valve (developed by M.H.M. Janssen, Vrije Universiteit Amsterdam) limits the gas flow of the jet out of the nozzle to periods of roughly 30 μ s. These pulses are synchronised with the laser system to limit the quantity of noble gas that is used and reduce the gas load on the turbo-molecular pumps. The focusing lens is situated on a translation stage, which enables control of the relative distance between the focus and the interaction region. The position of the focus relative to the interaction region can be used to tune phase-matching conditions, as described in Sec. 4.1.2.

In the experiments described in this work, harmonics were generated in argon and krypton for the support-based and rotational DSI experiments respectively. Compared to other noble gases, these gases have a relatively low ionisation potential (respectively, 15.763 eV and 13.9996 eV for argon and krypton), which enables a relatively high ionisation cross-section. However, as a trade-off they have lower cut-off frequencies (see Eq. 59) than higher ionisation potential alternatives like Neon or Helium. To achieve efficient phase-matching conditions between the terms in Eq. 63, gas backing pressure and the

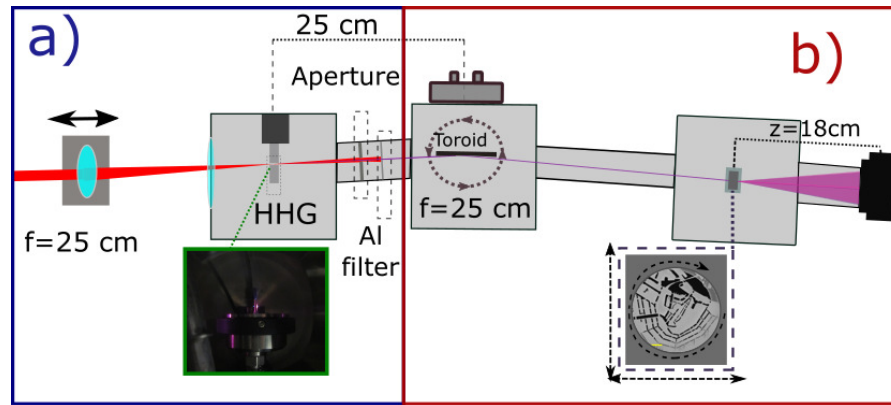


Figure 20: Schematic overview of the HHG experimental setup for the rotational DSI experiment. a) High-harmonic generation setup for both DSI experiments. Harmonics are generated in the HHG interaction zone (a picture that shows the gas jet in which harmonics are generated during operation is shown in the green outline). Behind the interaction zone, a combination of a 4 mm aperture and a 200 nm aluminium filter are used to filter out the infrared fundamental beam. b) rotational DSI imaging setup. The filtered HHG beam is one-to-one imaged to a point shortly before a sample holder. The sample is mounted on a rotational piezo-stage that is used to scan the sample orientation during the experiment.

position of the focus are tuned before each experiment by optimising on the output flux. While the exact tuning depends on varying laser conditions, typical values for the backing pressure were between 6 and 8 bar for argon.

High harmonics are generated in a low-divergence cone and co-propagate with the fundamental beam. Due to the low efficiency of the high-harmonic generation process, the high-harmonic flux is many orders of magnitude smaller than that of the fundamental beam. Therefore, the infrared beam must be filtered out effectively to be able to detect high harmonics on top of the background. We apply pre-filtering of the light using a 4 mm aperture, located roughly 15 cm downstream from the interaction zone. This aperture preferentially blocks the fundamental beam, as the divergence of the high harmonics is much lower due to phase-matching effects. Then, a 200 nm aluminium membrane reflects most of the remaining infrared beam, while it transmits approximately 60-70% of the light for the high harmonic orders (between 28 and 45 nm).

4.3 GENERATING EXTREME ULTRA-VIOLET PULSE PAIRS

4.3.1 *Fourier-transform spectroscopy and infrared pulse pairs*

In most HHG imaging experiments, single harmonics are selected from broad spectra using spectral filtering methods in order to satisfy

the temporal coherence requirements for CDI that are discussed in Sec. 3.5.2. Instead, in our EUV experiments we have applied Fourier-Transform spectroscopy on phase-locked high harmonic pulse pairs to obtain spectrally resolved signals at separate wavelengths, from which we reconstruct images with the methods described in Sec. 3.4.

To generate these HHG pulse pairs, the femtosecond pulses of the driving laser are split into pulse pairs in a common-path interferometer based on two pairs of birefringent wedges [129]. A schematic overview of this interferometer is shown in Fig. 21. An incident pulse

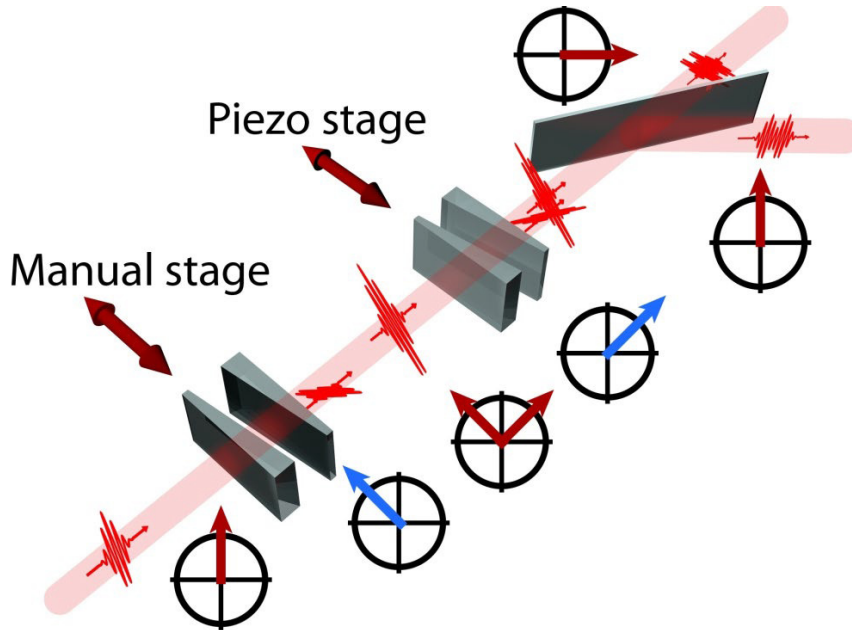


Figure 21: Schematic drawing of the common-path interferometer. The red polarisation diagrams indicate the polarisation of the beam at different points, while the blue diagrams show the orientation of the fast axes of the wedge pairs. A manual translation stage and a piezo-activated stage can control the amount of birefringent material traversed by the beam (and thus the time delay between the pulses), by moving one of the wedges in both wedge pairs in the direction of the double sided arrows. After the beam travels through both pairs of wedges, a thin-film polariser selects out a mutual polarisation direction from two pulses with orthogonal polarisations. Taken from [129].

is split into a pulse pair by a first set of birefringent wedges. This pair of wedges, with an optical axis that is rotated by 45° with respect to the polarisation of the incident beam, induces a delay of several picoseconds between the extraordinary and ordinary rays.

One of the wedges is mounted on a manual translation stage for rough tuning of this induced delay. A second pair of wedges, which has its fast and slow axes transposed with respect to the first pair, induces a time delay in opposite direction. One of the wedges in this

second pair is mounted on a linear piezo stage (Physik Instrumente GmbH, model number P-625.1CD).

The piezo stage enables fine control of the time delay between the pulses, by changing the amount of birefringent material traversed by the beam. This stage has a total travel range of 500 μm , a resolution of 1.4 nm and a repeatability of 5 nm. During operation the manual stage is tuned such that the pulses are overlapping while the piezo stage is approximately in the middle of its travel range.

The wedges in the interferometer consist of α -BBO and have an apex angle ϕ of 15° . This material was chosen for its strong birefringence ($\Delta n = n_e - n_o = -0.11$ at 800 nm) and low non-linear susceptibilities. The delay between pulses that is induced by each wedge pair scales linearly with the amount of birefringent material traversed by the beam. The specifications of the crystal combined with those of the piezo stage correspond to a maximum time-delay scan range of 50 fs, a time-delay resolution of 0.5 as and a repeatability of 0.14 as. Finally, reflection on a broadband thin-film polariser (TFP) projects the polarisation of the two pulses to the vertical axis. As half of the energy is reflected by the TFP this results into two pulses with a pulse energy of roughly 1 mJ each, which are used for high harmonic generation.

To avoid ionisation and heating effects of the first pulse from influencing the high harmonic generation process of the delayed pulse, one of the wedges in the interferometer is slightly tilted, inducing a 280 μm split in the focal plane.

4.4 EUV IMAGING SETUPS

In the DSI experiments of Ch. 5, the scattering samples were placed in a chamber downstream from the filter. Due to the large distance between the interaction zone and the filter, which was necessary to avoid damage from the infrared beam on the filter, the beam at the sample was significantly larger than the specimen. In the rotational DSI experiments of Ch. 6, the HHG sources were imaged one-to-one to a plane located at roughly 5 cm to the sample using a boron-carbide (B_4C) coated toroidal mirror with a focal length of 25 cm, in order use the available photons more efficiently. The distance of the focus to the sample was a trade-off between having significant beam overlap at the sample, as required for DSI, and photon efficiency. This toroidal mirror was designed to have a broadband reflectivity of around 80% at a 7.5° grazing incidence angle. This reduced the beam diameter near the sample by roughly a factor of two compared to the DSI experiment, resulting in a higher flux at the sample despite increased losses from the imaging system. A mechanical feedthrough system enabled control of the toroidal mirror alignment. The samples for these experiments were placed in a sample holder, mounted on a piezo-stage with two linear positioners (Smaract SLC-1730), that

were used to control the position of the sample in the transverse directions to the beam and switch between a grating spectrometer and imaging sensors, while in the rDSI experiment the 2D stage was combined with a piezo-driven rotation stage (Smaract SR-2812), which is depicted in the inset of Fig. 20. In the rDSI measurements, as the beam was only slightly larger than the sample and the axis of rotation was not perfectly aligned with the center of the sample, slight re-calibrations of the 2D linear position were necessary to realign the center of the sample with the beam. Diffraction patterns for the EUV experiments were captured using a CCD camera (Andor Ikon-L 936 SO, 2048x2048 pixels, pixel size 13.5 μm).

DIFFRACTIVE SHEAR INTERFEROMETRY FOR EXTREME ULTRAVIOLET HIGH-RESOLUTION LENSLESS IMAGING

5.1 ABSTRACT

We demonstrate a novel imaging approach and associated reconstruction algorithm for far-field coherent diffractive imaging, based on the measurement of a pair of laterally sheared diffraction patterns. The differential phase profile retrieved from such a measurement leads to improved reconstruction accuracy, increased robustness against noise, and faster convergence compared to traditional coherent diffractive imaging methods. We measure laterally sheared diffraction patterns using Fourier-transform spectroscopy with two phase-locked pulse pairs from a high-harmonic source. Using this approach, we demonstrate spectrally resolved imaging at extreme ultraviolet wavelengths between 28 and 35 nm.

This chapter was published as the following paper: G. S. M. Jansen, A. de Beurs, X. Liu, K. S. E. Eikema, and S. Witte, *Diffractive shear interferometry for extreme ultraviolet high-resolution lensless imaging*, *Opt. Express* 26, 12479-12489 (2018)

5.2 INTRODUCTION

In recent years, coherent diffractive imaging (CDI) has enabled vast progress in high-resolution microscopy [5, 40, 46, 130, 131]. Contrary to traditional microscopy, CDI does not rely on lenses to form an image from scattered light emerging from a sample. Instead, CDI employs numerical phase retrieval algorithms to reconstruct an image based on the recorded diffraction pattern [33, 82]. As the image resolution in CDI is not limited by focusing optics, it is well suited for microscopy using x-rays [79], extreme ultraviolet (EUV) radiation [46, 131] or electrons [132]. Despite the high-resolution results, the quality of the reconstructed intensity and phase of the images depends strongly on the signal-to-noise of the diffraction pattern [133]. Furthermore, other constraints such as finite support, positivity or atomicity are often required for convergence. This has led to the development of ptychography [21, 58, 134], which eliminates the need for strong constraints by taking much more data in a systematic manner.

The central challenge in CDI is to acquire knowledge of the phase of the recorded field. Performing a direct measurement of the phase is therefore beneficial, but typically does come at the cost of increased measurement complexity. The main example of such an approach is Fourier transform holography, in which the interference between a reference wave and a diffraction pattern is recorded [50, 135–138]. Holography allows for a simple image reconstruction which does not rely on iterative algorithms, but the image resolution and support are typically limited by the numerical aperture and wavefront of the reference wave.

Spatial phase determination of optical fields is a challenge that has been addressed in other areas as well. A specific approach that has shown promise in the context of CDI is lateral shearing interferometry (LSI) [139, 140], a technique that is used to reconstruct the wavefront - or phase profile - of a beam by interfering it with a sheared copy of itself. This results in an interference pattern that depends on the spatial derivative of the wavefront, which can be retrieved by spatial Fourier filtering. The wavefront can then be reconstructed by integration of the measured phase derivative. As a single LSI measurement only yields the one-dimensional derivative of the phase along the shear direction, several measurements with different shears are in principle necessary to retrieve the full 2D wavefront. Furthermore, accurate phase determination is only possible if the individual beams have smooth intensity profiles. The LSI phase profile can also be measured by phase shifting one of the beams and measuring the interference pattern for several phases. Isolation of the oscillating interference term then allows for direct determination of the interference phase. Such a measurement allows for measurement of much more complex

interference patterns. It has been shown that a collection of shear interference patterns for varying shears allows for the full reconstruction of the original electric field [141]. Simple numerical propagation of the electric field then enables phase contrast microscopy in various geometries.

In this article, we build upon the concept of lateral shearing interferometry to acquire differential phase information of diffraction patterns recorded with extreme ultraviolet radiation. The resulting diffraction intensity and differential phase information are then used as input for an iterative algorithm, that can reconstruct the full electric field based on a single laterally sheared diffraction pattern. The measurement and reconstruction of these diffraction patterns can be summarized as diffractive shear interferometry (DSI). In comparison with traditional coherent diffractive imaging methods, we find that our approach provides an improved reconstruction accuracy and convergence. For an experimental demonstration of the DSI approach, we measure laterally sheared diffraction patterns at several extreme ultraviolet wavelengths and numerically reconstruct high-resolution images from them.

To achieve spectral resolution, we employ spatially-resolved Fourier-transform spectroscopy (FTS) with a pair of phase-locked high-harmonic generation (HHG) sources [129]. A previous limitation of this FTS approach for HHG-based imaging has been the fact that the HHG beams need to be spatially displaced to avoid cross-talk in the HHG process [142]. The DSI approach presented here uses this sheared beam geometry in a natural way, even allowing improved reconstruction accuracy and robustness compared to single-beam experiments. From our results we find that our algorithm is able to accurately reconstruct complex electric fields even in the presence of significant noise. Coherent diffractive imaging with HHG sources has great potential for nanoscale imaging [46, 131]. Furthermore, elements often possess distinct absorption features at EUV wavelengths. Therefore, the present work forms a step towards EUV imaging with element-specific contrast.

5.3 SPATIAL SHEARING INTERFEROMETRY OF DIFFRACTION PATTERNS

5.3.1 *Interference of diffraction patterns*

In traditional CDI, the object is illuminated using a single beam of coherent, monochromatic light. The transmitted or reflected light scatters from the object and forms a diffraction pattern which is captured using a camera. In order to combine CDI with lateral shearing interferometry, we use two identical, mutually coherent beams to illuminate the object at slightly differing angles, as schematically depicted

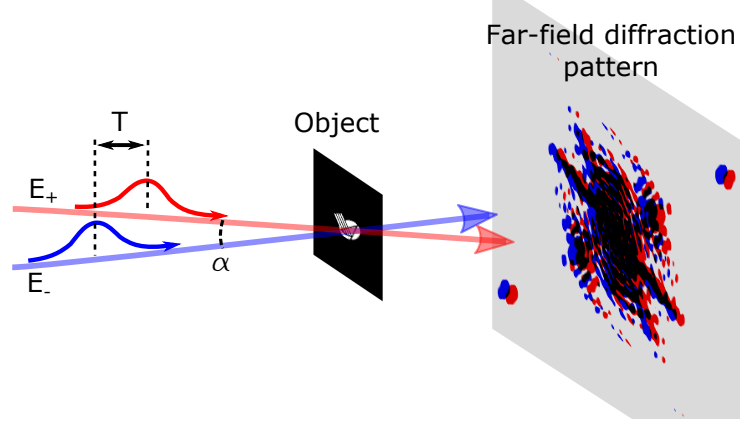


Figure 22: Schematic overview of lensless imaging by diffractive shear interferometry. Two identical and coherent beams, E_+ and E_- , illuminate a transmissive object such that the angle between the beams is α . This results in two far-field diffraction patterns on the camera which are slightly displaced relative to each other. The black region on the screen indicates where the diffraction patterns overlap and interfere.

in Fig. 22. For a thin, single-scattering object, the electric fields of the beams can then be written as the electric field of the illumination multiplied by the object transfer function. If dk is the wavevector corresponding to the half angle $\alpha/2$ between the two beams and X the transverse position in the object plane, the electric field corresponding to a single beam appearing directly after the object can be written

$$E_{\pm} = \tilde{A}(x) \exp[i(\tilde{\Phi}(x) \pm dkx)] \exp(-i\omega t_{\pm}), \quad (64)$$

where "+" and "-" correspond to the individual beams as indicated by Fig. 22. Effectively, the fields in Eq. (64) consist of the amplitude $\tilde{A}(x)$ and phase $\tilde{\Phi}(x)$ of the electric field transmitted by the object, multiplied by a linear phase ramp $\exp(\pm idkx)$ that distinguishes the two individual beams. Finally, there is a global phase term $\exp(i\omega t_{\pm})$. This electric field propagates towards the detector where the interference between E_+ and E_- is detected. In the case of far-field diffraction, the electric field can be described by the Fourier transform of the electric field in the object plane. The detected intensity can then be written as

$$I(k) = A(k + dk)^2 + A(k - dk)^2 + A(k + dk)A(k - dk) \exp\{i[\Phi(k + dk) - \Phi(k - dk) + \omega T]\} + c.c., \quad (65)$$

where the combined amplitude and phase $A(k) \exp[i\Phi(k)]$ at the camera is related by Fourier transform to the combined amplitude and phase $\tilde{A}(x) \exp[i\tilde{\Phi}(x)]$ at the object. For simplicity, the time difference between the beams is written as T . Compared to single-beam

CDI, the detected intensity in DSI contains more information as it encodes the phase shear in the interference term. This will naturally lead to a more stringent camera-space constraint that can be expected to aid convergence of phase retrieval algorithms [143]. Yet the available information can be exploited more effectively by separating the amplitude and phase terms in the interference term $A(k + dk)A(k - dk) \exp i[\Phi(k + dk) - \Phi(k - dk)]$. This can be achieved by performing measurements at multiple time delays T , as the interference is the only term in Eq. (65) that oscillates at frequency ω . Going one step further, taking a series of measurements as a function of T is equivalent to Fourier transform spectroscopy, and can even be used to extract interference terms for all frequencies present in the case of broadband illumination. Therefore, the proposed DSI approach is intrinsically compatible with polychromatic or broadband light sources such as high-harmonic generation, and can be used for spectrally resolved imaging at extreme ultraviolet wavelengths [142].

5.3.2 Image reconstruction

To reconstruct an image of the object, retrieval of the full electric field $A(k) \exp[i\Phi(k)]$ is required. Starting with the isolated interference term from Eq. (65), we will use an iterative algorithm to reconstruct the electric field. This algorithm relies on a set of constraints to the electric field, applied in different planes connected by free-space optical propagation [5, 33, 82]. The first constraint is provided by the measured data: the electric field at the camera plane should be consistent with the measured result. For our second constraint we will use a finite support; the electric field in the object plane is only non-zero in a certain limited window.

In traditional CDI, the most used camera plane operator is the modulus constraint: the amplitudes of the electric-field estimate are set to the measured values, while the estimated phases are preserved. However, in DSI the modulus constraint is not the most suitable operator for reconstructing interferometrically sheared diffraction patterns. This is because the measured intensity pattern $A(k + dk)A(k - dk)$ is not equal to the intensity $A(k)^2$ of the electric field to be reconstructed. Even though a modulus constraint based on Eq. (65) may be envisaged, it does not take into account the available phase information in an optimal way. We therefore derive a new camera plane operator that makes more efficient use of the amplitude and phase information available in DSI.

Starting with the n^{th} guess of the electric field

$$E_n(k) = A_n(k) \exp[i\Phi_n(k)] \quad (66)$$

at the camera and the complex measured interference pattern

$$M(k) = A(k + dk)A(k - dk) \exp\{i[\Phi(k + dk) - \Phi(k - dk)]\}, \quad (67)$$

it can be seen that division of the measured data by a sheared copy of the electric field guess yields a new electric field guess

$$E_{n+1}(k + dk) = \frac{M(k)}{E_n^*(k - dk)}. \quad (68)$$

If the original guess of the electric field is accurate, the new electric field guess is in fact equal to a shifted version of the electric field. Therefore, division of the measured data by a negatively sheared electric field guess yields a positively sheared electric field guess. This operation forms the basis of a useful camera-space constraint for interferometrically sheared diffraction pattern reconstruction. A general camera-space constraint can be written as

$$E_{n+1}(k) = (1 - \beta)E_n(k) + \frac{\beta}{2} \left[\frac{M(k - dk)E_n(k - 2dk)}{|E_n(k - 2dk)|^2 + \alpha^2} + \frac{M^*(k + dk)E_n(k + 2dk)}{|E_n(k + 2dk)|^2 + \alpha^2} \right], \quad (69)$$

which is a linear combination of the old guess and the average of the new guesses for the positively and negatively sheared electric fields. The numerical constant β determines the strength of the correction to the electric field guess and is typically set to 0.9. Instead of a direct division by the electric field E , we multiply by $E^*/(|E|^2 + \alpha^2)$, where α is a regularization constant that prevents errors arising from division by zero. For noisy data, we expect that the best results will be obtained when α is comparable to the noise floor.

In combination with a finite object support, the presented novel camera-space constraint is sufficient for retrieval of the full electric field. A basic approach to include a support constraint in the algorithm is using the error-reduction method, where all values outside of the support are set to zero. The output-output algorithm and hybrid input-output algorithms provide two alternatives which have been shown to provide different convergence properties [33, 144].

5.3.3 Comparison between DSI and single-beam CDI

To investigate the efficiency of the proposed phase-retrieval algorithm, we performed simulations comparing DSI to traditional single-beam CDI methods. Example datasets for CDI are produced by simulating far-field diffraction patterns with Poisson noise. We simulated several diffraction patterns with varying signal-to-noise ratio (SNR) by adjusting the total number of collected photons. To account for camera readout noise, we added Gaussian background noise with a standard deviation of 10 counts. Starting with a wide initial support, we reconstructed the image using both hybrid input-output and error-reduction in an alternating fashion. The shrinkwrap procedure was used to adaptively update the support [80]. The results of these simulations can be seen the first two columns of Fig. 23. In this figure,

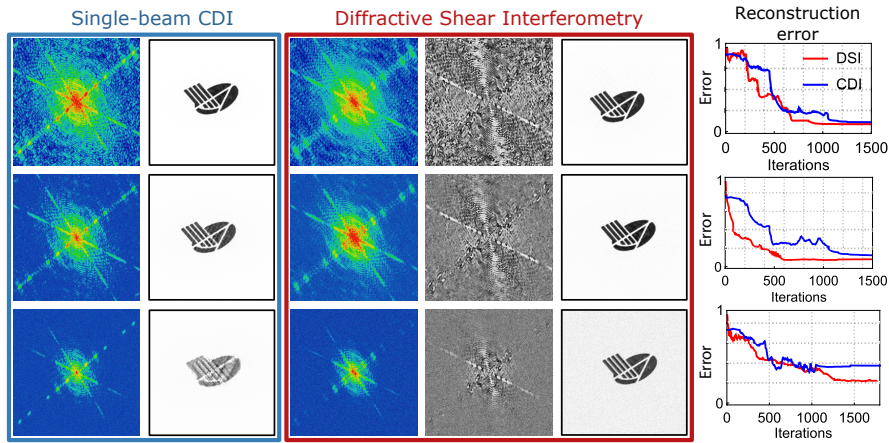


Figure 23: Comparison of traditional single-beam CDI with the proposed diffractive shear interferometry. Each row compares the two methods for identical signal-to-noise levels. The first two columns show the simulated diffraction patterns and reconstructions, respectively, for single-beam CDI. Columns three and four show the simulated DSI amplitude and phase. Column five shows the image retrieved using our algorithm. Finally, the last column compares the accuracy of both methods. The error is calculated from the RMS difference between reconstruction and original image. For clarity, the error calculation only considers the direct vicinity of the object.

each row has a different SNR. The top row is simulated such that we get 10^8 counts in the brightest pixel, leading to a SNR of 10^4 in the center of the diffraction pattern. The second and third row have SNRs of 1.8×10^3 and 0.6×10^3 respectively.

For DSI, we simulated several datasets with noise levels similar to the CDI simulations. This was achieved by adding Poisson noise and a Gaussian background to the shear interferometry signal. To also account for noise in the phase of the simulated interference pattern, we multiplied the simulated noise with a random phase pattern before addition to the noise-free diffraction pattern. The amplitude and phase of the simulated diffraction patterns can be seen in the third and fourth columns of Fig. 23 respectively. We verified that this method leads to realistic interference signals by comparing the simulated diffraction patterns to the result of a full simulated Fourier transform scan. Furthermore, we compared the simulated data to real measured EUV shearing interferometry data (section 5.4).

Reconstructions of the simulated DSI signals are shown in the fifth column of Fig. 23. These reconstructions were obtained by combining the algorithm presented in section 5.3.2 with a shrinkwrap procedure to find the support of the image. In order to compare these results to those obtained from the CDI simulations, we calculate the accuracy of the reconstructions. This is defined as the RMS difference between the reconstruction and input image, averaged over the number of

pixels and only calculated for the pixels in the direct vicinity of the original object. This calculation is corrected for spatial shifts and a global phase offset, which are free parameters for CDI. For DSI, we find that there is a limited number of spatial shifts and phase offsets compatible with the measured data. This is directly related to the phase information in the recorded diffraction pattern, as a shift of the object translates to a phase tilt in the far-field diffraction pattern. After shearing according to formula 67, this phase tilt reduces to a phase offset in the measured data. Reversing the process shows that a phase offset in the measured data leads to a shift of the reconstructed object, and any image reconstruction has to match this constraint.

From the reconstruction accuracy comparison in the sixth column of Fig. 23, it is clear that DSI consistently leads to a better solution than single-beam CDI. In addition, the reconstruction of DSI patterns appears to converge slightly faster than the reconstruction of single-beam CDI patterns. There are various parameters which influence the performance of DSI reconstruction, of which the value of the shear is the most critical. For the simulations presented in Fig. 23, we assumed that the shear was known accurately. For real measurements, accurate initial knowledge of the shear may not be possible, especially in cases where the shear has to be known with sub-pixel accuracy. In such cases, it is possible to extend the phase retrieval algorithm with a shear optimization step. As will be mentioned in section 5.4, for our present reconstructions we have used a manual search to find the correct shear.

Furthermore, the value of the shear has a strong influence on the measured signal and therefore on the retrieval process. If the shear is reduced to zero, the shear interferometry signal reduces to the single-beam far-field diffraction pattern and the phase information is reduced to zero. As the shear is increased, both the intensity of the diffraction pattern and the phase information become more complex-structured. Finally, very large shears lead to a reduced overlap between the diffraction patterns, leading to a weaker signal that is more sensitive to noise. We simulated several measurements with different shears, and found that larger shears lead to slightly better results and faster convergence, provided that the SNR remained sufficiently high. The shear used in Fig. 23 was approximately equal to one speckle of the diffraction pattern (the inverse of the object size), which is found to be a good compromise between signal strength and noise sensitivity.

5.4 EXPERIMENTAL DEMONSTRATION OF DIFFRACTIVE SHEAR INTERFEROMETRY USING HIGH-HARMONICS

As already noted in section 5.3.1, a promising approach to measuring DSI signals is through the use of a setup for Fourier-transform spec-

troscopy. Such a measurement enables coherent diffractive imaging using all wavelengths present in the illumination. We implement this scheme by employing a phase-locked pair of high-harmonic generation (HHG) sources to perform wavelength-resolved microscopy at EUV wavelengths. The phase-locked EUV pulse pair is produced by HHG upconversion of tightly phase-locked pairs of infrared driving pulses that have been produced by an ultrastable common-path interferometer [129]. Typical parameters of these infrared pulses are a central wavelength of 800 nm, a pulse energy of 1 mJ in each of the beams, a 300 Hz repetition rate and a pulse duration of 25 femtoseconds. A basic layout of the setup used for HHG and subsequent DSI imaging of samples in a transmission geometry is presented in Fig. 24(a). A typical EUV spectrum generated in Argon is also shown in Fig. 24(b). It is important to note that the HHG spectrum can change significantly due to small changes in the driving laser alignment.

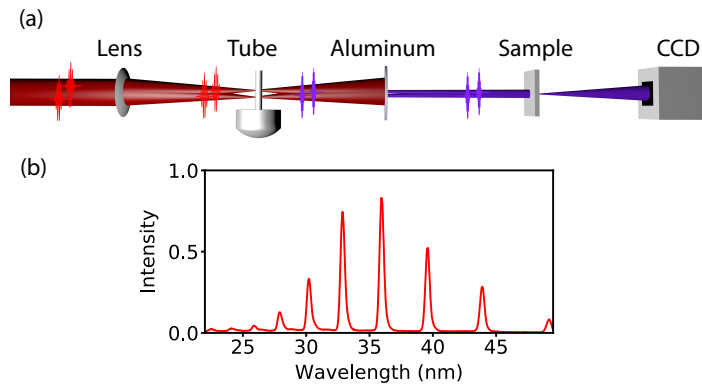


Figure 24: (a) Schematic overview of the setup used for EUV Fourier-transform interferometry. The output of a common-path interferometer is focused by the lens into a gas jet confined to tube. The resulting EUV pulse pair is separated from the infrared using an Aluminum filter and detected using an Andor Ikon-L CCD camera. A transmissive object can be positioned between the Aluminum filter and the camera using a remotely controlled translation stage. (b) Typical high-harmonic spectrum generated in Argon, measured through Fourier-transform spectroscopy in the same setup without an object in the beam.

The Fourier transform spectroscopy settings must be adapted to the HHG source spectrum. In practice, this means recording a few hundred time steps, spanning an optical path difference of at least two optical cycles of the driver in steps smaller than half the wavelength of the shortest harmonic [129, 142]. These settings depend strongly on the on-sample illumination spectrum. For monochromatic illumination, just four time steps would suffice.

5.4.1 Fourier-transform holography

As a first experiment, we used focused ion-beam milling to fabricate the sample shown in Fig. 25(a). The sample consists of our institute logo and in addition three circular apertures with diameters 12, 4 and 1 μm , respectively. The apertures act as references for Fourier-transform holography (FTH) by providing a spherical wave which interferes with the diffraction pattern arising from the logo [136]. For such a sample, a spatial Fourier-transform of the far-field diffraction pattern directly yields multiple images of the sample. The resolution of these images is determined by the diameter of the associated reference aperture. Therefore, FTH can provide an initial low-resolution guess of the image from which it is possible to determine the support. It is then possible to use phase-retrieval methods to improve the image resolution and contrast [135, 145].

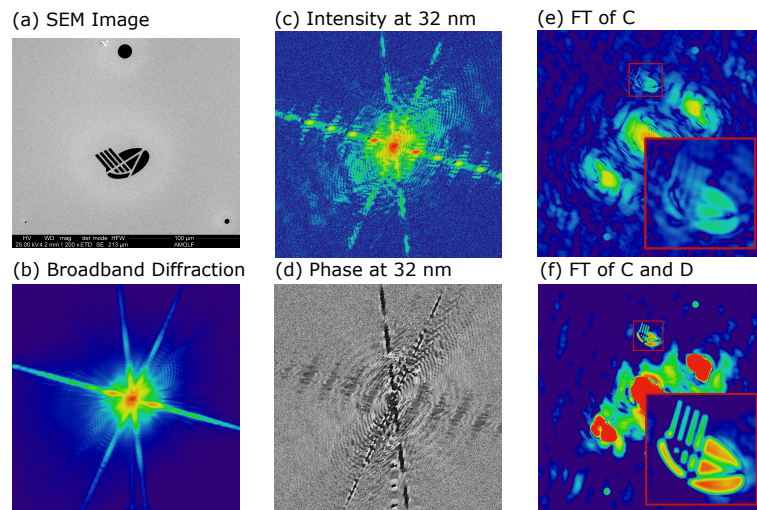


Figure 25: Extreme ultraviolet DSI of a transmissive sample with multiple holographic references. (a) Scanning electron microscope image of the sample used for the initial measurements at EUV wavelengths. The sample consists of our institute logo and three circular apertures with diameters 12, 4 and 1 μm respectively acting as holographic references. (b) Broadband EUV transmission of the sample. (c) Intensity at 32 nm retrieved from the FTS-scan. (d) Phase of the signal at 32 nm. (e) Hologram acquired using just the intensity at 32 nm as shown in (c). (f) Hologram acquired using both intensity and phase information at 32 nm. The inset show the hologram arising from interference with the 4 μm aperture.

The results obtained using only FTH are shown in Fig. 25. We used Fourier-transform spectroscopy to retrieve monochromatic shear interferometry signals for several individual high-harmonics. Every image of the Fourier transform spectroscopy measurement consists of a 10 second exposure, a 1 second exposure and a 0.1 second exposure to acquire the high dynamic range necessary for high-resolution CDI.

The spectral resolution in this experiment is 96 THz, providing an effective bandwidth $\Delta\lambda/\lambda$ of approximately 1/100 for the retrieved shear interferometry signals around 30 nm wavelength. As an example, we show the amplitude and phase of the shear interferometry signal for the 25th harmonic at 32 nm in Fig. 25(c) and (d) respectively. To illustrate the importance of the phase pattern, Fig. 25(e) shows the hologram calculated from the amplitude data alone, which has low contrast and contains clear distortions. We find that it is possible to retrieve a good-quality hologram from the shear interferometry signal if both measured amplitude and phase are used to calculate the hologram, as shown in Fig. 25(f). Note that the holograms arising from the 1 μm aperture are not visible, which is probably due to limited signal-to-noise.

5.4.2 DSI reconstruction

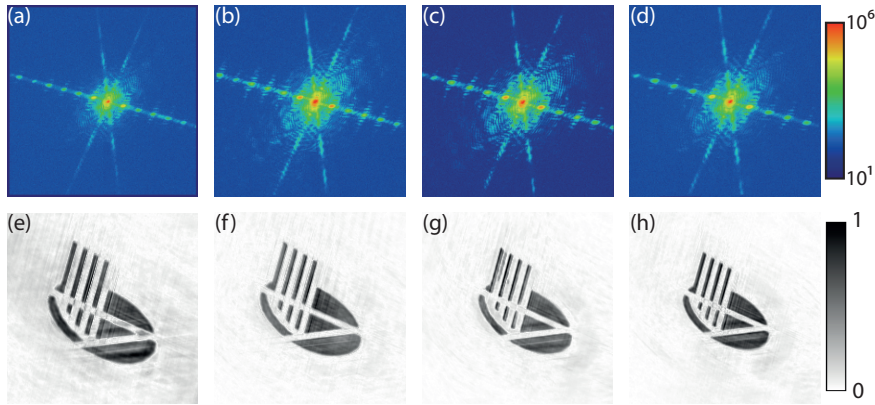


Figure 26: DSI reconstruction results of the multi-wavelength data presented in Fig. 25. (a-d) for the ARC/NL research center logo. Measured amplitude of the DSI patterns for the 29th, 27th, 25th and 23rd harmonics with wavelengths 28 nm, 30 nm, 32 nm and 35 nm respectively, shown on a logarithmic color scale. (e-h) Reconstructed images for the 29th to 23rd harmonics respectively, show on a linear grayscale. The images all have a height and width of 200 pixels, while the sample has a width of 40 μm . The difference in magnification follows directly from the differences in wavelength between the images.

The holography results provide a decent starting point for electric field reconstruction using DSI. For this reconstruction the holography result is used to determine an initial support. The determination of the initial support is slightly complicated by the presence of the reference apertures, as it is important to position the supports for the apertures at the correct positions relative to each other and to the main object. To accommodate for slight errors in this process, we start the image reconstruction with an object support that is larger

than the image obtained through holography. The object support is determined from the hologram by thresholding and expanding the result by a few pixels. We found that applying the object support using a linear combination of error reduction and hybrid input-output leads to the best convergence.

As with the DSI simulations, we combine the image reconstruction with a shrinkwrap routine. In addition, we performed a manual parameter search to find the optimal value for the shear. A simple search algorithm was used to find the phase offset in the measured data. These steps are performed by comparing the convergence over several hundred iterations for various values of the shear and phase offset. Typically, a retrieval sequence to reconstruct an image with known shear and offset phase is as follows: Using the initial support, 600 iterations of DSI with HIO and ER are performed, such that every object space operation is a linear combination of 10% HIO and 90% ER. During these iterations, the value for the regularization constant α is ramped down from 80 to 40. Then we perform six rounds of shrinkwrap followed by 200 DSI+ER+HIO iterations with constant α . As shown in Fig. 26, we were able to reconstruct high-quality images using this approach for four individual high-harmonics between 28 and 35 nm from a single measurement.

5.4.3 DSI imaging of complex objects

To verify that DSI also works for more complicated physical data, we fabricated another sample, shown in Fig. 27(a). It was produced by focused ion-beam (FIB) milling in a 100 nm gold layer on top of a freestanding 15 nm silicon nitride film. The settings of the FIB caused it to strip most of the gold while leaving a fine and irregular silicon nitride mesh. As the mesh is partially transparent to EUV radiation, this yields a sample that has a complicated pattern of transmission levels. Furthermore, the sample did not contain holographic reference apertures.

Similar to the measurement of the holography sample, we are able to obtain monochromatic interference patterns for several wavelengths through an FTS scan. In this case, each time step of the FTS scan consists of a 4 second exposure and two shorter ones. This lead to a 7 second measurement time per time step and a total measurement time of 50 minutes. As an example, Fig. 27(c) shows the amplitude and phase of the DSI pattern obtained for the 25th harmonic at 34 nm. In this case, the spectral resolution was 81 THz, yielding an effective bandwidth of 1/109 at 34 nm wavelength.

For the reconstruction, the initial object support was now retrieved from the autocorrelation of the sample. This provides a larger initial support and eliminates the need for a fine determination of the offset phase. We did perform a new shear optimization, as the experimen-

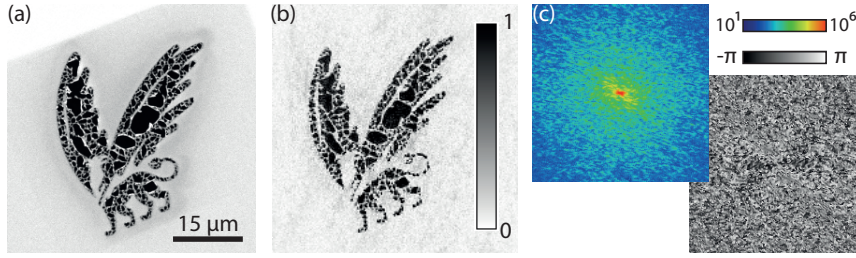


Figure 27: Results obtained for a complex ‘griffin’ sample without holographic references. (a) SEM image of the sample as described in section 5.4.3. (b) DSI reconstruction of the sample at 34 nm wavelength, shown on a linear colorscale. (c) Measured amplitude (logarithmic false color) and phase (gray) of the DSI pattern used to obtain (b).

tal geometry changed slightly in this measurement. With the optimal shear, we perform 2100 DSI iterations combined with 75% ER and 25% HIO, using shrinkwrap every 75 iterations. The reconstruction is finished using 1400 DSI iterations combined with 90% ER and 10% HIO, using shrinkwrap every 25 iterations. During the full reconstruction, α is ramped down smoothly from 1000 to 10. The final result is shown in Fig. 27(b). By calculating the phase-retrieval transfer function, we find that the final result has a resolution of approximately $0.27 \mu\text{m}$. This resolution corresponds to the diffraction limit of the captured data. Comparing the SEM and DSI images, it is clear that DSI is able to reconstruct the full complexity of the sample including the partial transmission of the silicon nitride mesh. This demonstrates that DSI is a promising technique to image complex isolated samples.

5.5 CONCLUSIONS

In conclusion, we have developed the method of diffractive shear imaging, in which the full electric field of a diffraction pattern is reconstructed based on the measurement of a single sheared diffraction pattern. Comparing the algorithm to standard phase retrieval methods for traditional CDI, we find that our method consistently yields more accurate results. In addition, the phase retrieval process converges slightly faster than traditional approaches. As DSI signals can be easily measured using spatially-resolved Fourier-transform spectroscopy, this approach is ideally suited for multi-wavelength coherent diffractive imaging [142]. In particular, this approach is interesting for CDI using high-harmonic generation sources, which produce a broad range of narrowband harmonics at extreme ultraviolet wavelengths. We have demonstrated high-resolution microscopy on two different samples using several high-harmonics at wavelengths between 28 and 35 nm. There are several possible extensions which may

lead to an even more versatile imaging technique. For example, rotation of the sample enables the measurement of shear interferometry signals at different effective shears. A set of these measurements can greatly enhance the image retrieval, and reduce the need for a well-defined object support. Furthermore, combining diffractive shear interferometry with ptychographic techniques can lead to a greater field of view while still preserving spectral sensitivity.

FUNDING

The project has received funding from the European Research Council (ERC) (ERC-StG 637476) and the Netherlands Organisation for Scientific Research (NWO).

ACKNOWLEDGMENTS

We thank D. E. Boonzajer Flaes for useful discussions and R. Kortekaas and N. Noest for technical assistance.

EXTREME ULTRAVIOLET LENSLESS IMAGING WITHOUT OBJECT SUPPORT THROUGH ROTATIONAL DIVERSITY IN DIFFRACTIVE SHEARING INTERFEROMETRY

6.1 ABSTRACT

We report on a method that allows microscopic image reconstruction from extreme-ultraviolet diffraction patterns without the need for object support constraints or other prior knowledge about the object structure. This is achieved by introducing additional diversity through rotation of an object in a rotationally asymmetric probe beam, produced by the spatial interference between two phase-coherent high-harmonic beams. With this rotational diffractive shearing interferometry method, we demonstrate robust image reconstruction of microscopic objects at wavelengths around 30 nm, using images recorded at only three to five different object rotations.

This chapter was published as the following paper: A. C. C. de Beurs, X. Liu, G. S. M. Jansen, A. P. Konijnenberg, W. M. J. Coene, K. S. E. Eikema, and S. Witte, *Extreme ultraviolet lensless imaging without object support through rotational diversity in diffractive shearing interferometry*, *Opt. Express* 28, 5257-5266 (2020)

6.2 INTRODUCTION

In recent years, coherent diffractive imaging (CDI) has proved to be a versatile imaging technique with many applications, such as high-resolution imaging using X-ray and extreme ultraviolet (XUV) [5, 40, 130, 131] as well as coherent beams of electrons [30] as illumination. High harmonic generation (HHG) is a process that enabled the development of tabletop sources generating a broad harmonic spectrum of spatially coherent XUV light [146]. Using these sources recently sub-wavelength resolution has been achieved [46]. The broad bandwidth of HHG sources enables imaging over wide wavelength spans throughout the extreme ultraviolet and soft-X-ray ranges. Recently we have demonstrated multi-wavelength CDI based on Fourier-transform spectroscopy [142, 147], and various promising spectrally resolved imaging results have been reported [58, 148].

In CDI, the exit wave of an object is reconstructed from a measured diffraction intensity pattern. In the far-field limit, the diffracted electric field corresponds to the Fourier-transform of the exit wave. Therefore, a reconstruction of this exit wave can be obtained by an inverse Fourier-transform of this diffracted electric field. The challenge in CDI measurements is that typically only the squared amplitude of this electric field is measured. To reconstruct the exit wave, the phase of the electric field at the detector plane needs to be retrieved using iterative methods [20, 79]. In the single-shot implementation of CDI, such algorithms rely on additional information, which often means knowledge of the object support. Finding a good estimate of such a support is often difficult, and can be solved in a number of ways: By using low resolution microscopy technique, such as optical microscopy [79] or Fourier-transform holography [135]. Another commonly used technique is shrinkwrap [80], where the object support is adaptively refined from a loose starting guess of the support. However, for objects with non-sharp edges, shrinkwrap-based algorithms require the user to make a choice about the threshold value at which to define the support boundary. Many recent developments have been driven by ptychography [21, 58, 134]. Ptychography uses transverse scanning of a spatially confined probe beam, while maintaining partial overlap between adjacent scan positions. This approach introduces additional translational measurement diversity which strongly constrains the exit wave solution. Ptychographic methods remove the need for an object support and the associated prior object knowledge, and simultaneously provide a reconstruction of the probe beam [134], but it does come at the cost of a strongly increased number of measurements.

In this paper, we present a novel approach to CDI that enables high-resolution imaging without the need for an object support in the reconstruction algorithm, using only a limited number of measure-

ments with a rotating interference pattern as the probe. Our approach is based on the diffractive shearing interferometry (DSI) approach which allows wavelength-resolved CDI. For our present application we use XUV radiation generated by HHG [129]. In DSI, the interference between two sheared diffraction patterns is measured through spatially resolved Fourier-transform spectroscopy (FTS) [147]. Effectively, this provides a measure of the phase gradient in the direction of the shear [140]. We now extend this approach by measuring multiple shear directions. In analogy to ptychography, these multiple measurements provide increased measurement diversity since our interferometric illumination is rotationally asymmetric. A phase retrieval approach that rotates an asymmetric illumination was earlier suggested by Wang et al. [149], and we recently explored the concept of interferometric probe ptychography in detail for visible light applications [150]. Shearing interferometry methods for phase imaging with visible light [141], deep-UV [151] and X-rays [152] have also been reported. Here we show that the obtained diffraction information is sufficient to accurately reconstruct an object image without the need for accurate knowledge of an object support. The only requirements are 1) that the diffraction pattern is sufficiently sampled, meaning that the object is fully contained within the field of view, and 2) that the illumination is smooth across the object (as is the case for CDI in general). The experimental results are further supported by numerical simulations, in which the influence of the number of orientations, the relative magnitude of the shear and the signal-to-noise ratio are investigated.

6.3 ROTATIONAL DIFFRACTIVE SHEARING INTERFEROMETRY

The measurement concept is shown in Fig. 28. An object is illuminated by a pair of broadband noncollinear HHG beams, which are produced using phase-locked pairs of intense driving laser pulses [129]. The noncollinear geometry gives rise to a coherent, spatially sheared pair of diffraction patterns at a camera placed in the far field. A series of far-field diffraction patterns is recorded as a function of the time delay between the HHG pulses. The combination of such sheared illumination with an FTS scan enables spectrally resolved diffractive imaging for the different harmonic wavelengths through diffractive shearing interferometry (DSI) [147]. Note that in the direction opposite to the shearing direction, extra support information is still required. To remove the need for such support information, the object is rotated and DSI diffraction data is recorded for a series of object angles, while the shear between the two beams remains fixed. In this section, this rotational DSI approach is explained in detail, and the phase retrieval algorithm required for image reconstruction is outlined.

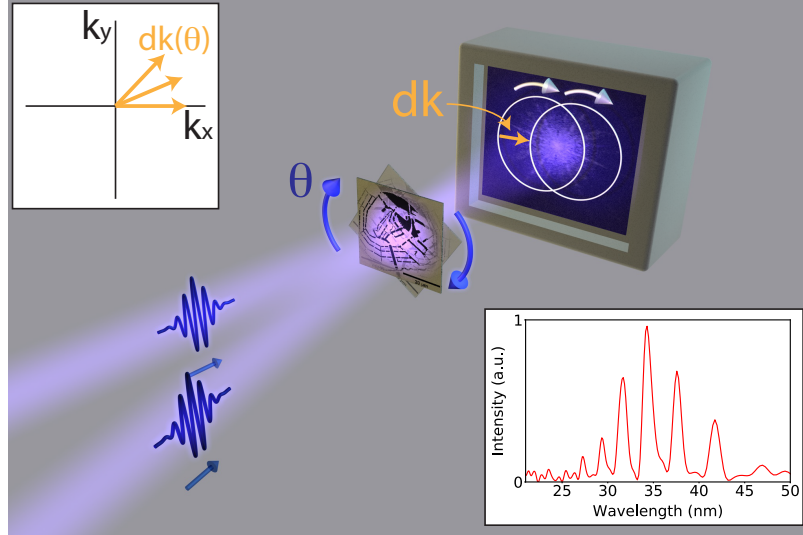


Figure 28: Two mutually delayed, identical XUV beams are incident on our sample in a non-collinear geometry. The signal measured on the camera is the interference pattern between two laterally sheared diffraction patterns. A time delay (FTS) scan is recorded for a range of sample rotations along angle θ , which introduces measurement diversity because of the directed interference in the illumination. The top left inset depicts how the relative shear vector \mathbf{dk} changes in k -space upon sample rotation. The amplitude of \mathbf{dk} is exaggerated for clarity. The bottom right inset shows a typical HHG spectrum retrieved from an FTS scan.

6.3.1 Diffractive Shearing interferometry

With DSI combined with FTS, it is possible to recover two identical but laterally sheared monochromatic diffraction-plane electric fields from their interference [147]. FTS scans provide (after Fourier transformation with respect to the time delay between the two pulses) such a signal resolved for each wavelength of the light source:

$$\begin{aligned} M(\mathbf{k}) &= E(\mathbf{k} + \mathbf{dk})E(\mathbf{k} - \mathbf{dk})^* \\ &= A(\mathbf{k} + \mathbf{dk})A(\mathbf{k} - \mathbf{dk}) \exp\{i(\Phi(\mathbf{k} + \mathbf{dk}) - \Phi(\mathbf{k} - \mathbf{dk}))\}, \end{aligned} \quad (70)$$

where the measured signal $M(\mathbf{k})$ corresponds to the product of the diffracted electric field $E(\mathbf{k} + \mathbf{dk})$ and its complex conjugate with opposite shear $E(\mathbf{k} - \mathbf{dk})^*$. $A(\mathbf{k})$ is the amplitude of the electric field of a single beam at the camera and $\Phi(\mathbf{k})$ is the phase of the electric field, \mathbf{k} are the camera plane coordinates and $2\mathbf{dk}$ is the combined lateral shear between the two beams. Note that bold-font symbols are used to indicate vectors. As can be seen from Eq. 70, the retrieved diffraction data does not directly correspond to the far-field diffraction pattern of the object, as the complex product between the two beams is measured instead of the intensity. An advantage of this measurement

is that the complex phase term provides information about the spatial phase derivative along the direction of the shear between the beams.

Starting from $M(\mathbf{k})$ it is possible to reconstruct the full complex far-field electric field of a single illumination beam, which is related to the object exit wave by a spatial Fourier-transform. This can be achieved by using an iterative phase retrieval algorithm [20, 144], which combines a finite support constraint with a camera space electric field update that takes into account the sheared geometry:

$$E_{n+1}(\mathbf{k}) = (1 - \beta)E_n(\mathbf{k}) + \frac{\beta}{2} \left[\frac{M(\mathbf{k} - \mathbf{dk})E_n(\mathbf{k} - 2\mathbf{dk})}{|E_n(\mathbf{k} - 2\mathbf{dk})|^2 + \alpha^2} + \frac{M^*(\mathbf{k} + \mathbf{dk})E_n(\mathbf{k} + 2\mathbf{dk})}{|E_n(\mathbf{k} + 2\mathbf{dk})|^2 + \alpha^2} \right], \quad (71)$$

where E_n is the n^{th} update step of the electric field estimate, β is a feedback parameter with a value close to unity that prevents amplitude overshooting, and α is a regularization constant to avoid division by zero.

6.3.2 Rotational diffractive shearing interferometry

As shown in Fig. 28, the rotational symmetry that would be present for single-beam illumination is broken by the fixed shear direction in the noncollinear double-beam illumination. Therefore, rotating the object around the average beam axis results in a qualitatively different diffraction pattern at the detector, as the individual diffraction patterns rotate but the interference direction remains fixed. Measurements at multiple rotation angles therefore provide increased measurement diversity. This additional information forms the basis for a phase retrieval algorithm that does not require support constraints or other prior sample-plane knowledge. Instead, it suffices to impose a constraint that requires the single-beam electric fields measured at different shear angles, as retrieved from a DSI procedure, to be identical. Because of the experimental challenge involved in rotating the shear direction between two HHG beams, we choose to rotate the object around an axis given by the average beam direction (Fig. 28). A series of DSI measurements is then performed as a function of this rotation angle. After the measurement, the resulting datasets are numerically rotated so that effectively the respective complex fields are acquired at different orientations of the object relative to a common orientation. This procedure is equivalent to the measurement of DSI patterns with a rotating shear. To accurately perform this numerical rotation of complex field data sampled on a square grid, a method is used that synthesises rotations by using a set of three shear operations [153]. This rotated data forms the starting point for an augmented DSI algorithm, which begins with a starting guess for the

unsheared electric field $E_{0,j}(\mathbf{k})$ for each measurement j at shear angle θ_j . The unsheared electric fields are then updated using the standard DSI camera space update [147], but now for each angle θ_j :

$$E_{n+1,j}(\mathbf{k}) = (1 - \beta)E_n(\mathbf{k}) + \frac{\beta}{2} \left[\frac{M_j(\mathbf{k} - \mathbf{d}\mathbf{k}_j)E_n(\mathbf{k} - 2\mathbf{d}\mathbf{k}_j)}{|\mathbf{E}_n(\mathbf{k} - 2\mathbf{d}\mathbf{k}_j)|^2 + \alpha^2} + \frac{M_j^*(\mathbf{k} + \mathbf{d}\mathbf{k}_j)E_n(\mathbf{k} + 2\mathbf{d}\mathbf{k}_j)}{|\mathbf{E}_n(\mathbf{k} + 2\mathbf{d}\mathbf{k}_j)|^2 + \alpha^2} \right], \quad (72)$$

where $M_j(\mathbf{k})$ is the measured signal at θ_j , $E_{n,j}(\mathbf{k})$ is the current field reconstruction and at that angle. Note that we refer to our camera-space coordinates as \mathbf{k} , since the camera plane takes the role of reciprocal space in our measurements. After each update, the field reconstructions in the object plane for all angles are averaged to obtain the field estimate for the next iteration:

$$E_{n+1}(\mathbf{r}) = \langle E_{n+1,j}(\mathbf{r}) \rangle \quad (73)$$

While the algorithm typically converges for both simulated and experimental data, it was observed that on several occasions the convergence stagnated in a local minimum. A probable cause for this stagnation is the presence of a possible relative phase shift between the sheared diffraction patterns retrieved at different angles, which can lead to errors in the field average in Eq. 73. This relative phase offset is challenging to retrieve from the iterative procedure directly. Therefore, to aid reconstruction and further improve the algorithm convergence properties we instead apply an additional constraint in the averaging step, typically after every 40 iterations:

$$E_{n+1}(\mathbf{r}) = \gamma \langle |E_{n+1,j}(\mathbf{r})| \rangle + (1 - \gamma)E_n(\mathbf{r}) \quad (74)$$

This constraint has the effect of damping object phase variations, and is therefore similar to a positivity constraint. However, it is not as strict as a true positivity constraint because of the introduction of the relaxation parameter γ . The value of γ is typically around 0.5.

6.4 NUMERICAL SIMULATIONS OF ROTATIONAL DSI

To systematically investigate how the quality of the reconstructions depends on the number of measurements at different rotation angles, we have performed a series of numerical simulations. The results of these simulations is shown in Fig. 29. Starting out from a test image (Fig. 29(a)), we simulate multiple DSI patterns for a range of different shear vector angles. In the simulations, the angle of the shear vector is rotated instead of the object, so that numerical object rotation of the diffraction data is not needed. Care is taken to simulate the far-field DSI patterns with a signal-to-noise ratio (SNR) comparable to

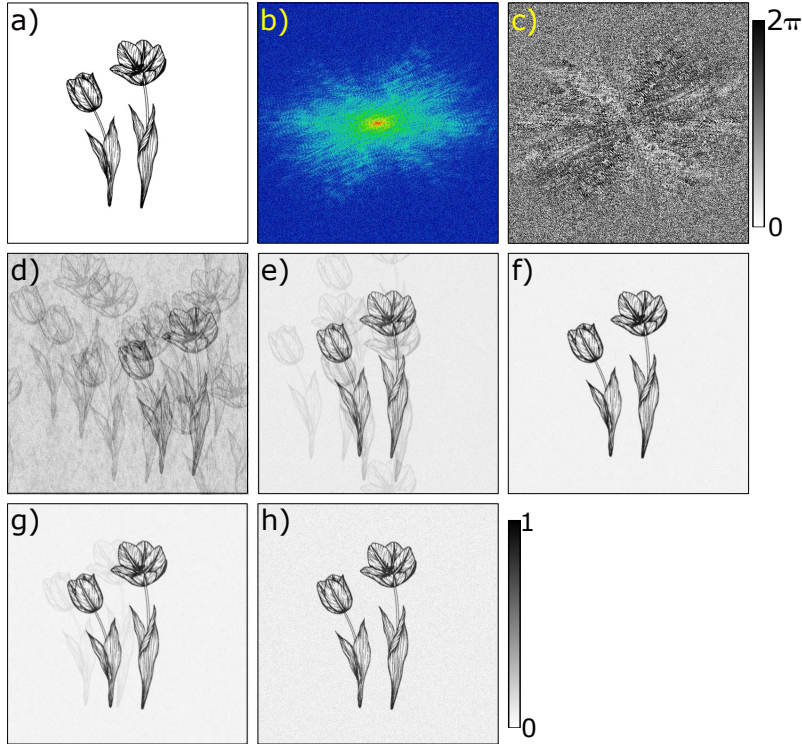


Figure 29: Numerical simulations of the algorithm performance as a function of number of included measurement angles. (a) Intensity image of the simulated object (a flat phase is assumed) (b, c) Far-field DSI intensity (b) and phase (c) pattern as they would be recorded in an experiment. (d-g) Reconstructed images of the object when including data respectively from two, three, four and five measurements recorded at different angles. Each of these images is the average of 10 independent reconstructions. (h) Typical result for a single reconstruction, using diffraction signals at five different shear angles. The colorbar bar right of (h) applies to all intensity images of the object.

our experimental data, which will be discussed in section 6.5. The intensity and phase of a typical simulated DSI pattern are shown in Figs. 29(b,c). We typically choose the magnitude of the shear to be around 5 pixels, which is slightly larger than the typical speckle size of the diffraction patterns, as this was previously found to give the best DSI reconstructions [147]. A series of DSI patterns is generated with the shear rotated to angles of 0° , 10° , 15° , 80° and 90° , respectively. The same angles were used to obtain the experimental results, which will be discussed below. Reconstructions are then performed using subsets of these DSI patterns, for an increasing number of angles ranging from two to five. These subsets always included the 0° and 90° datasets, because this pair introduces the largest diversity due to the orthogonal shears. The other angles were selected randomly in each subset. For each of these subsets, ten independent reconstructions were performed using randomized starting field guesses and

shear orientations. Of these ten reconstructions, the average is then taken as the overall reconstruction result for the subset corresponding to that particular number of shear angles. These averaged reconstruction results are shown in Figs. 29(d-g). In these reconstructions, the total number of camera update steps (Eq. 72) was kept constant.

It was found that when using only two shear angles, convergence was not guaranteed, and the reconstruction quality varied as a function of both the direction of the shear and the starting guess of the electric field. In the cases for which the algorithm did converge, it would often converge to a solution in a step-like manner after showing no visible improvement for many iterations, as illustrated in Fig. 30(a). Figure 30 shows the normalised mean square error (NMSE) [154] as a function of the number of iterations. This NMSE is given by the expression:

$$\text{Error} = \sqrt{\frac{\sum_{\mathbf{k},j} |M_j(\mathbf{k}) - M_{\text{rec},j}(\mathbf{k})|^2}{\sum_{\mathbf{k},j} |M_{\text{rec},j}(\mathbf{k})|^2}} \quad (75)$$

where $M_{\text{rec},j}$ and M_j are the reconstructed and measured interference terms, respectively. For the simulated datasets consisting of DSI patterns for three to five shear angles, the algorithm reliably converged to a clearly recognizable object image. From the averaged data (Figs. 29(e-g)), it does become clear that there is some remaining variability in the exact position of the object in the transverse plane. This effect is significant for three angles, but strongly reduces for four and five angles. For comparison, a single (non-averaged) reconstruction result when taking five angles into account is displayed in Fig. 29(h). This improved convergence behaviour is also apparent in Fig. 30(b), which shows the NMSE for a reconstruction including five angles. Compared to the two-angle reconstruction, convergence is much faster and less erratic, and proceeds in a nearly monotonous fashion. Note that the periodic spikes in the NMSE for the five-angle reconstruction stem from the application of the update constraint Eq. 74 every 40th iteration. From the reconstructed images and the error metric, the five-angle case is found to converge after just 70-100 iterations, after which the error metric only shows such periodic behaviour due to the regular update constraint application discussed above. In contrast, the spiking behaviour in the two-angle NMSE is irregular and cannot fully be explained by this constraint application.

6.5 EXPERIMENTAL DEMONSTRATION OF ROTATIONAL DSI

6.5.1 Setup and measurement procedure for DSI with a HHG source

To experimentally demonstrate the concept of rotational diversity in DSI, a series of measurements was performed in an XUV lensless

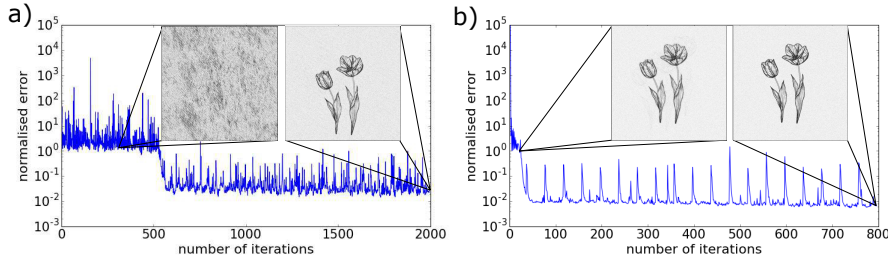


Figure 30: Estimation of convergence, using the normalised mean square error metric (Eq. 75) as a function of the number of iterations for a simulation with (a) two and (b) five diffraction patterns with varying shear-object orientations. The insets show reconstructed images after different amounts of iterations.

imaging geometry. The XUV radiation is produced by focusing 1 mJ, 25 fs laser pulses at a central wavelength of 800 nm from an optical parametric chirped pulse amplifier into a jet of Argon gas. The beam is focused with an $f = 25$ cm plano-convex lens. The gas jet is 1 mm wide, and produced by a pulsed nozzle backed by up to 8 bar of Argon that ejects gas into a metal tube to constrain the flow. The laser intersects the jet through small holes in the side of the metal tube. The repetition rate of the laser system is 300 Hz. To enable spectrally resolved imaging we use an FTS-approach. A coherent pair of HHG pulses is produced by two phase-stable driving laser pulses, which each focus in a separate location inside the gas jet but interfere at the object location. Further details of this method are given in previous work [129, 147]. A typical HHG spectrum as used in this experiment is shown in Fig. 28.

The object under study is a transmission sample, representing a map of the water ways in the city of Amsterdam, manufactured using focused ion beam milling. The object substrate consists of a freestanding 50 nm thick silicon nitride film, coated on both sides with 70 nm of gold. A scanning electron microscope (SEM) image of the object is shown in Fig. 31(a). In the black areas in this image, the film was fully milled through, while in some parts the material was only partially removed, so that the object should appear as a 'grayscale' intensity image under XUV exposure.

The sample is placed at a distance of 18 cm from the detector (Andor Ikon-L, 2048×2048 pixels, $13.5 \mu\text{m}$ pixel size). The lateral shear between the two diffraction patterns at the detector plane is set to $134 \mu\text{m}$, corresponding to about 10 pixels and an angle of $67 \mu\text{rad}$. The rotation of the sample with respect to the shear direction (angle θ in Fig. 28) is controlled by a piezo-driven rotation stage. FTS scans were performed for a series of angles, being 0° , 10° , 15° , 80° and 90° , respectively. These particular angles were selected to minimize the error in the numerical rotation of the diffraction patterns. For the FTS scan at 0° , a time scan of 6.2 fs is recorded in steps

of 34.4 attoseconds. These scan parameters correspond to a Nyquist-sampled spectral range of 14.5 PHz sampled at a frequency spacing of 164 THz. For the measurements at the other angles, a time scan of 6.3 fs was recorded in slightly larger time steps of 42.2 attoseconds, which results in a similar frequency spacing but at a somewhat smaller spectral range of 11.9 PHz. Each diffraction pattern in the FTS scans consists of set of exposures of 10 s, 2 s and 0.5 s, which are numerically merged into one image with increased dynamic range. We emphasize that the large number of images recorded in this measurement is specific for our Fourier-transform approach to diffractive imaging [142], and provides diffraction patterns for all wavelengths in the HHG source spectrum simultaneously. When instead using spectral filtering before the sample, the rotational DSI approach presented here in principle only requires a two to four recordings at different phase steps for each angle, which can be obtained in a total measurement time of a few minutes.

6.5.2 Measurement results and rotational DSI reconstructions

DSI signals at a wavelength of 31 nm as obtained from the FTS scan are shown in Fig. 31(b-g). From these diffraction patterns, object reconstructions are performed using the rotational DSI procedure described in section 6.3.2. Reconstructions are attempted using the data from a varying number of angles ranging from two to five, similar to what was done for the simulations described in the previous section. For all reconstructions, the total number of algorithm iterations was kept fixed at 3000 for all reconstructions.

For the experimental data, very similar convergence behaviour was observed compared to the simulations. When using two angles, the algorithm generally did not converge reliably. When including data from three to five angles, convergence was much more robust and proceeded in a more monotonous fashion. The results of these reconstructions when including three, four and five angles are displayed in Figs. 31(h-j), respectively. For the three- and four-angle reconstructions, the quality of the results was consistently good if a sufficiently large angular range (i.e. 0-90°) is included. In all reconstructions, the estimated resolution is 300 nm, based on the size of the smallest resolved features. This resolution matches well with the highest spatial frequency that was detected above the noise level. When comparing the reconstructions for the different number of included angles, we find that the resolution is similar between all reconstructions. The reconstructed image for five angles does show slightly sharper edges with less residual ripples in most parts of the image, but a consistent and significant resolution improvement cannot be claimed. Slight improvements can also be seen in the contrast of the images when including more angles. This mainly appears as a more homogeneous

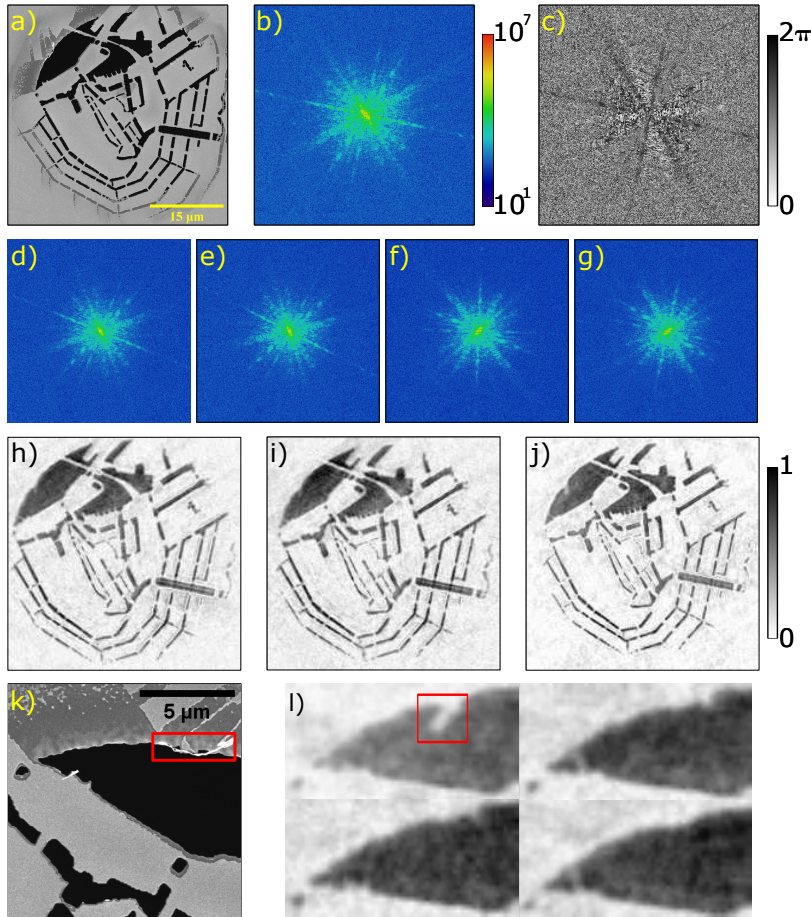


Figure 31: Object reconstructions from experimental data using rotational DSI at a wavelength of 31 nm. a) SEM image of the transmission sample. b,c) Intensity (log-scale) and phase of the diffraction pattern at 31 nm wavelength, obtained from the FTS scan at 0 degree angle. d-g) Diffraction intensity (log-scale) measured at 10, 15, 80 and 90 degree sample orientation. h-j) Object images obtained from the DSI reconstruction when including measurements at three, four and five different angles, respectively. k) Close-up of the SEM image highlighting a small contamination that moved upon rotation. l) Close-up of the reconstructed images at sample orientations at 0° (top left), 10° , 15° and 90° (bottom right), showing how the contamination is reconstructed differently at these different angles.

intensity distribution in the larger spaces (both light and dark), as well as in a more accurate representation of the partially transmitting areas. From these results we conclude that the main improvement in diversity from the rotational DSI approach is reached upon inclusion of data from at least three angles, and that adding data taken at more angles only results in moderate further improvements.

A noteworthy aspect in the retrieved object images, is that the algorithm is robust against some variation in the actual object upon

rotation. It was found that the fabricated sample contained a small contamination that was loosely attached to an edge of a larger open area, and that this feature changed its orientation as the sample was rotated over 90° . An zoomed-in SEM image showing this contamination is displayed in Fig. 31(k). The rotational DSI algorithm calculates an average field estimate in each update step. Nevertheless, when the final field estimate is calculated using the averaged phase combined with the diffraction intensity from a specific rotation angle, images are obtained that show variations in the location of the contamination, in a way that matched the expectation for how this feature would move upon rotation when considering gravity. Parts of the reconstructions for 0° , 10° , 15° and 90° highlighting this contamination are shown in Figs. 31(l). It should however be noted that, although the reconstruction is robust against real object variations between measurements at different angles, the presence of such changes does violate a basic assumption of the algorithm. Although the contamination observed here was too small a detail to limit reconstruction quality, the robustness to such variations is still a subject of further study.

6.6 CONCLUSION

We have demonstrated that using rotational diversity in combination with an asymmetric probe beam enables CDI image reconstruction without prior knowledge about the object support, other than that the object is contained within the imaging field-of-view. We have experimentally verified this concept, using the DSI approach that we developed earlier, in which interference between two coherent extreme-ultraviolet beams results in the asymmetric probe beam structure. We find that, although in principle the concept works with diffraction patterns recorded at only two angles, the inclusion of data for up to five different angles results in improved image quality and more robust reconstruction. The developed method provides a convenient way of relaxing support constraint requirements and/or other forms of prior knowledge in CDI, and enables robust reconstruction using only a limited number of measured diffraction patterns.

6.7 SUPPLEMENTARY MATERIAL

FUNDING

This research was supported by the Nederlandse Organisatie voor Wetenschappelijk Onderzoek (NWO) and the European Research Council (ERC Starting Grant 637476).

ACKNOWLEDGMENTS

This work has been carried out at ARCNL, a public-private partnership of UvA, VU, NWO and ASML.

APIE: AN ANGLE CALIBRATION ALGORITHM FOR REFLECTION PTYCHOGRAPHY

7.1 ABSTRACT

Reflection ptychography is a lensfree microscopy technique particularly promising in regions of the electromagnetic spectrum, where imaging optics are inefficient or not available. This is the case in tabletop extreme ultraviolet microscopy and grazing incidence small angle x-ray scattering experiments. Combining such experimental configurations with ptychography requires accurate knowledge of the relative tilt between the sample and the detector in non-coplanar scattering geometries. Here, we describe an algorithm for tilt estimation in reflection ptychography. The method is verified experimentally, enabling sample tilt determination within a fraction of a degree. Furthermore, the angle-estimation uncertainty and reconstruction quality are studied for both smooth and highly structured beams.

This chapter was published as the following paper: Anne de Beurs, Lars Loetgering, Milan Herczog, Mengqi Du, Kjeld S. E. Eikema, and Stefan Witte, *APIE: an angle calibration algorithm for reflection ptychography*, **Opt. Express** 28, 5257-5266 (2020)

7.2 INTRODUCTION

Ptychography is a diffractive imaging technique that enables simultaneous quantitative phase microscopy and wavefront sensing [84]. Instead of producing a direct image of a sample of interest on a detector, a series of diffraction intensities is recorded while a sample is laterally scanned through a focused beam. The recorded data is inverted via iterative phase retrieval algorithms, resulting in a deconvolution of sample and illumination contributions in the observed signal [22, 134]. Ptychography has become a popular technique for extreme ultraviolet, x-ray, and electron microscopy, where the lensless experimental geometry dispenses with the need for high-resolution imaging optics [29, 155, 156]. Moreover it has been used for visible light label free quantitative phase microscopy [157, 158], near-infrared wavefront sensing [23], and terahertz imaging [32]. Throughout the past decade the experimental robustness of ptychography has been improved by means of various self-calibration techniques. These include algorithms for the correction of lateral [159, 160] as well as axial [25, 161] position errors, wavefront instability [27], and partial coherence [26, 28]. An additional complication arises in reflection-mode ptychography [162], where the sample and camera are situated in a non-coplanar geometry. Tilting the sample introduces a nonlinear coordinate warping in the observed diffraction data, parameterized by the relative angle between the specimen and the detector [65]. Inaccurate knowledge of this angle results in model mismatch, with the effect of degraded imaging performance. Here, we report an angle self-calibration algorithm for reflection-mode ptychography. We demonstrate the method on experimental near-infrared data. In addition, we investigate the influence of the illumination wavefront shape on the uncertainty of the retrieved angle.

Far-field diffraction between two mutually tilted planes is given by [64–66]

$$\tilde{\psi}(u, v) = \iint \psi(x', y') \exp[-i2\pi(ux' + vy')] dx' dy', \quad (76)$$

where x', y' denote sample (=source) coordinates. The relation between spatial frequencies u, v and observation coordinates x, y is described by the mapping

$$\mathbf{T}: u = \frac{x}{\lambda r_0} \cos \theta + \frac{\sin \theta}{\lambda} \left[\left(1 - \frac{x^2 + y^2}{r_0^2} \right)^{1/2} - 1 \right], v = \frac{y}{\lambda r_0}. \quad (77)$$

where $r_0 = \sqrt{x^2 + y^2 + z^2}$ denotes the distance from the sample plane origin to a point x, y in the observation plane. z is the distance from the sample plane origin to the observation plane origin. θ is the angle between the sample surface normal and the optical axis

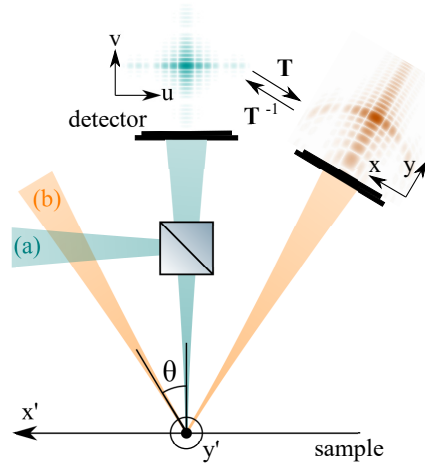


Figure 32: Effect of sample tilt on diffraction. (a) Sample and detector in coplanar detection geometry and perpendicular incidence illumination. (b) Non-coplanar geometry with oblique illumination. The diffraction pattern in (b) is obtained via nonlinear transformation \mathbf{T} of the diffraction pattern in (a) and vice versa.

(cf. Fig. 32). Equations 76 and 77 assume a small detection numerical aperture, i.e. $x, y \ll z$. For $\theta \neq 0$ the coordinate transformation distorts the diffraction lobes with increasing distance from the center coordinate. This is illustrated in Fig. 32, where the observed diffraction pattern under oblique incidence is equivalent to the diffraction pattern observed under perpendicular incidence when subjected to the mapping \mathbf{T} .

7.3 BACKWARD MAPPING VS FORWARD MAPPING

We consider two approaches for numerically transforming a function from one coordinate system to another (see Fig. S1 of the supplementary materials). The first method, referred to here as *forward mapping*, applies a coordinate transformation to the input (=detector) coordinate grid $(x, y) \rightarrow (u, v) = \mathbf{T}(x, y)$ to find the associated grid points in output (=spatial frequency) coordinates. Due to the nonlinearity of the transformation, the output grid exhibits irregular spacings. As most commonly used FFT methods require uniform grids, the intensity on this warped grid is interpolated onto a regular grid. This method was previously suggested for use for tilted plane coordinate correction by Gardner et al. [163]. However, this approach has some downsides in terms of interpolation: The data points for this method are not on a rectilinear grid aligned with the coordinate axes, which excludes the use of fast bivariate interpolation schemes, such as bilinear or bicubic [164, 165]. Alternatives to these bivariate interpolation methods tend to either compromise accuracy or are much slower in determining the interpolation weights for neighbouring pixels. Such

interpolation schemes are no option for our angle correction method (see below), which needs to embed the interpolation step into each iteration of the algorithm. Thus a more performant approach is needed.

An alternative approach to transform the intensities is to substitute $x(u, v)$ and $y(u, v)$ into the measured intensity $I(x, y)$ using the *inverse mapping* \mathbf{T}^{-1} . The reverse transformation is applied to an evenly spaced spatial frequency output grid to find the associated observation coordinates. Next, the intensity function at those detector points is found by means of interpolation $I(x_{\text{warped}}, y_{\text{warped}}) = I(\mathbf{T}^{-1}(u_{\text{regular}}, v_{\text{regular}}))$. Since the data points for this interpolation step are located on a regular detector pixel grid, this interpolation step is compatible with bilinear interpolation, which is straightforward and fast [166]. As repeated transformation and interpolation steps of the diffraction pattern are required for the angle calibration procedure reported in this work, a backward mapping approach with bilinear interpolation is used in this paper. Starting from the forward transform (see Eq. 77, the following expression for the inverse transformation \mathbf{T}^{-1} was derived (see the supplementary materials in the appendix B for more details):

$$\mathbf{T}^{-1} : x = \frac{y}{v} \frac{\lambda u + \sin(\theta)}{\lambda \cos(\theta)} - z \tan(\theta), y = \frac{-2vz^2}{b_0 - [b_0^2 - 4az^2]^{1/2}}, \quad (78)$$

where

$$a = \cos(\theta)^2 v^2 - \frac{\cos(2\theta)}{\lambda^2} + u^2 + 2 \sin(\theta) \frac{u}{\lambda}, \quad (79)$$

and

$$b_0 = -2z \sin(\theta) \left(u + \frac{\sin(\theta)}{\lambda} \right). \quad (80)$$

7.4 ALGORITHM

In its simplest form, ptychography models the wave diffracted by a sample as the product of an illumination and a sample transmissivity or reflectivity, depending on the operation mode. The resulting wave exiting the sample plane is propagated into the observation plane by application of a suitable diffraction model. This results in an estimated wave in the detector plane, which can be updated in such a way that it complies with the experimental observation [22, 134]. Here, we add an extra step that minimizes the mismatch between the forward model and the experimental observation with respect to the *a priori* unknown specimen tilt angle θ . To this end, we measure model mismatch by the error metric

$$e = \sum_{u,v} \sum_j \left| I_{j,m}(u(x, y, \theta), v(x, y, \theta)) - |\mathcal{F}[\psi_j(x', y')]|^2 \right|, \quad (81)$$

where the summation is over all measured spatial frequencies (u, v) and scan positions (j) , and \mathcal{F} denotes two-dimensional Fourier transformation. For energy conservation upon coordinate transformation, the data is normalised on measured total energy. Note that due to the non-linearity of the transformation, a Jacobian determinant correction will be required when operating closer to grazing incidence or at higher NA. Such a correction is described for tilted plane propagation with the angular spectrum method in [68]. Our angle estimation method, summarized in Alg. 1, is a combination of a randomized search inspired by the Luus-Jakoola (LJ) algorithm [167] and the extended ptychographic iterative engine (ePIE) [22]. At each iteration, the measured diffraction intensities are transformed with \mathbf{T}^{-1} for a test angle θ_t drawn from a uniform probability distribution (\mathcal{U}) of width $2\Delta\theta$ and centered around the current estimate θ . As the candidate solution approaches the true tilt angle, the model mismatch in Eq. 81 decreases. Therefore, if the error e_t for the test angle θ_t is lower than the error $c \cdot e$ for the previous angle estimate θ , the latter will be replaced by the former. We added an additional factor, $c = 0.999$, to make the comparison between the test angle error and the previously estimated angle more robust. At every iteration of the algorithm $\Delta\theta$ is linearly contracted to narrow down the search space. Next, inspired by the approach of mPIE [91], a momentum acceleration term v_j is added to the angle to speed up the rate of convergence. This momentum term is initialized at zero, and gets updated at the end of every iteration: $v_j = (\theta_{\text{update}} - \theta) + \eta \cdot v_{j-1}$, where $\eta = 0.7$ is a friction term. At the end of each loop the angle estimate is updated with the following momentum update step $\theta = \theta_{\text{update}} + v_j$. To test our angle calibration method in experiment, a series of ptychographic measurements were recorded in a tilted-plane reflection geometry using a USAF (Thorlabs R3L1S4P) resolution test target. The experimental setup is shown in Fig. 33. Illumination around a wavelength of 708.8 nm was generated by spectrally limiting a super continuum source by means of short pass (SP1000) and long pass (LP700) filters, and finally by selecting a narrow wavelength band with an acousto-optic tunable (AOTF) filter ($\Delta\lambda = 0.6$ nm). The sample and detector were mounted on two concentric rotation stages, enabling control of the tilt angle θ between the incident beam and the specimen's surface normal. Using this setup 20 data sets were recorded at a tilt angle of $43 \pm 1^\circ$, which was triangulated from the setup geometry. In half of these measurements a focused top-hat beam was used, while a structured beam was used in the other half. The beam structuring was achieved by means of a scotch tape. Each data set consists of 152 diffraction patterns recorded on a CCD camera (AVT GT3400, 14 bit, 3384×2704 pixels) at a sample-detector distance of 71.4 mm. The linear overlap ratio in these scans was 87%. Reconstructions were executed on a NVIDIA Titan RTX GPU. Reconstructions in this paper

Algorithm 1 Angle calibration ptychographic iterative engine (aPIE) based on Luus-Jaakola algorithm

```

1: procedure aPIE( $P, O, \theta$ )
2:    $v_0 = 0$  ▷ initialize momentum
3:    $c = 0.999$ 
4:   for  $m \leftarrow 1$  to  $n$  do ▷ n: number of iterations
5:      $\theta_t \leftarrow \theta + \xi, \xi \in \mathcal{U}[-\Delta\theta, \Delta\theta]$  ▷ draw  $\theta_t$  random
6:      $(P, O, e_t) \leftarrow \text{ePIE}(P, O, \theta)$ 
7:      $(P_t, O_t, e_t) \leftarrow \text{ePIE}(P, O, \theta_t)$ 
8:     if  $e_t < c \cdot e$  then
9:        $v_j = (\theta - \theta_t) + \eta \cdot v_{j-1}$  ▷ update momentum
10:       $(\theta, P, O, e) \leftarrow (\theta_t + v_j, P_t, O_t, e_t)$ 
11:    else
12:       $v_j = \eta \cdot v_{j-1}$ 
13:       $(\theta, P, O, e) \leftarrow (\theta + v_j, P, O, e)$ 
14:    end if
15:     $\Delta\theta \leftarrow (1 - m/n) \cdot \Delta\theta_{\max}$  ▷ contract search interval
16:  end for
17:  return  $P, O, \theta$ 
18: end procedure

```

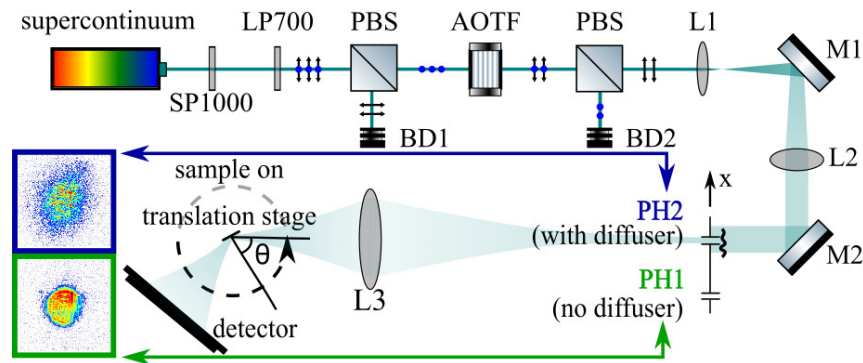


Figure 33: Experimental setup. A supercontinuum source is spectrally limited via short pass (SP1000) and long pass (LP700) filters to a wavelength range of 700 nm to 1000 nm. The beam is linearly polarized using polarization beam splitters (PBS). A narrow spectral band ($\Delta\lambda = 0.6$ nm) is selected by means of an acousto-optic tunable filter (AOTF). The beam is expanded through lenses L1 ($f_1 = 25$ mm) and L2 ($f_2 = 300$ mm), and modulated through pinholes PH1 (empty pinhole) or PH2 (pinhole with a scotch tape diffuser). Finally the pinhole is imaged by L3 ($f_3 = 500$ mm) onto the sample. The sample and detector are mounted on concentric rotation stages (dashed lines), permitting flexible control in the tilt angle θ between the sample normal and the optical axis.

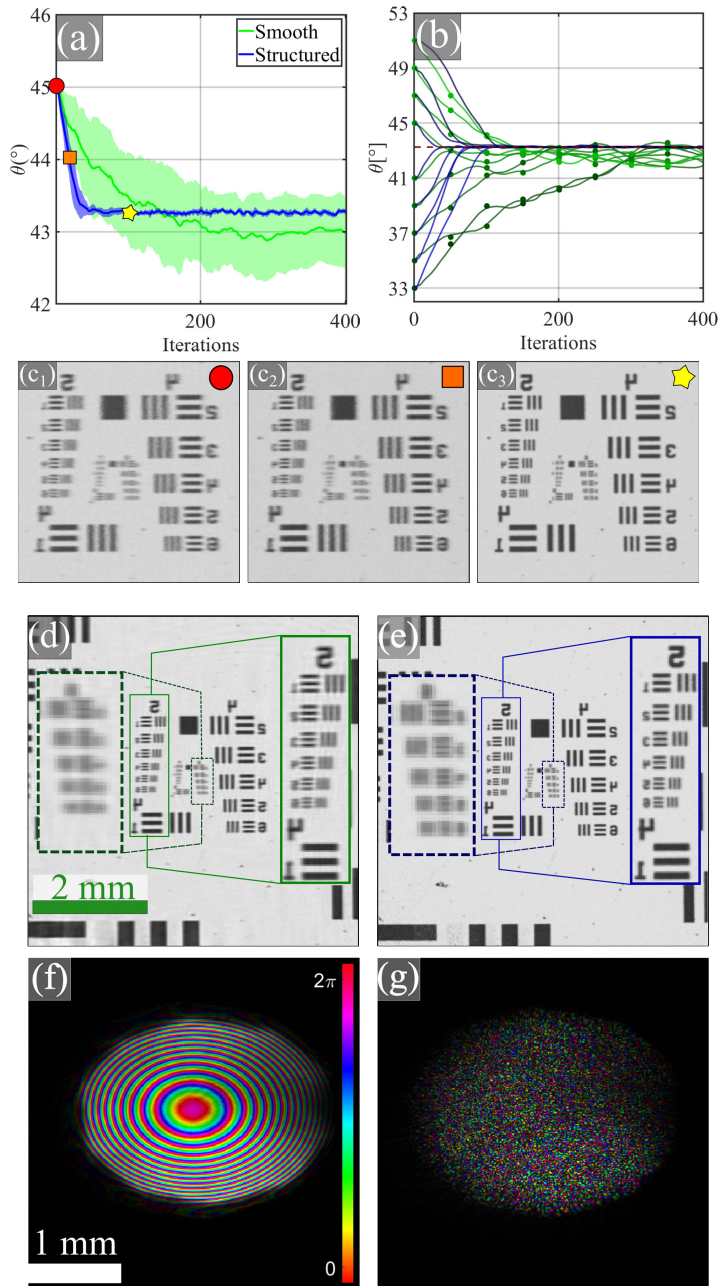


Figure 34: (a) Comparison of the standard deviation of the estimated angle for smooth (green) and structured (blue) illumination. The solid lines indicate the average tilt angle estimate, while the shaded areas indicate the region within ± 1 standard deviation (averaged over 10 measurements) from the mean. (b) Convergence behaviour for varying initial tilt angle θ guesses. The green lines (with round markers) indicate smooth illumination and the blue lines indicate structured illumination. The results shown in (a) and (b) are preprocessed by 200 iterations of ePIE at the original angle estimates before aPIE is started. (c₁-c₃) Image reconstructions before (c₁), during (c₂), and after (c₃) convergence of the angle correction method using structured illumination. Note that ePIE convergence was already reached for (c₁) before the angle correction was initiated. (d,f) Reconstructions of object and probe, respectively, obtained with a smooth beam. (e,g) Reconstructions of object and probe, respectively, obtained with a structured beam.

have been preprocessed by 200 iterations of ePIE, before applying 400 iterations of aPIE. Representative reconstructions of the object and the probe are depicted in Fig. 34 (d,f) for the case of smooth illumination, and in Fig. 34 (c,e,g) for the case of a structured illumination. Upon starting angle optimization, the error (Eq. 81) rapidly improves as illustrated in Supplementary Figure 37. The robustness of the angle calibration of the smooth beam was compared to that of the structured beam through an estimation of the standard deviation of the recovered values of the tilt angle θ . The results of this comparison are shown in Fig. 34(a), where the solid line and shaded areas indicate the average and standard deviation of the current estimate of θ . The solid curves were calculated by averaging reconstructions of 10 different data sets. It is seen that the standard deviation for the angle estimate is much smaller for the case of the structured beam, indicating more precise parameter estimation performance. This is also reflected in the improved object reconstruction quality in Fig. 34(e) (structured) as compared to Fig. 34(f) (smooth). Next, we tested the robustness of our method against inaccurate initial tilt angle estimates. A series of reconstructions were carried out with varying starting values for θ . The recovered tilt angle θ for these reconstructions as a function of the number of iterations is shown in Fig. 34(b). It is seen that our angle calibration method retrieved the angle within the aforementioned uncertainty given by the respective beam profile for initial deviations as large as 10 deg, with a more rapid convergence rate observed for the structured illumination. Finally the feasibility of a combined calibration of the detector sample distance z and the tilt angle θ was investigated. For this purpose, a series of reconstructions was executed with varying starting θ - z -estimates the structured beam data. These reconstructions alternated between 200 iterations of zPIE [25] and 50 iterations of aPIE for 2500 iterations. The trajectories of these combined reconstructions through the joint θ - z plane are shown in Fig. 35, where each colour indicates a single reconstruction with a different initial guess. These reconstructions converged to a value for theta of $43.37 \pm 0.06^\circ$ and to a value for z of 71.16 ± 0.04 mm, where the uncertainty is a single standard deviation in the final parameter estimates.

7.5 DISCUSSION AND CONCLUSION

In this letter we proposed a self-calibration algorithm for estimating the tilt angle in non coplanar reflection ptychography. The method was tested experimentally, where it showed robust performance for an initial estimate range up to 10° deviation from the true angle. We observed empirically in these tests that a structured illumination helps to reduce the uncertainty in the angle estimate and to improve the convergence rate of our proposed algorithm. Additionally, we

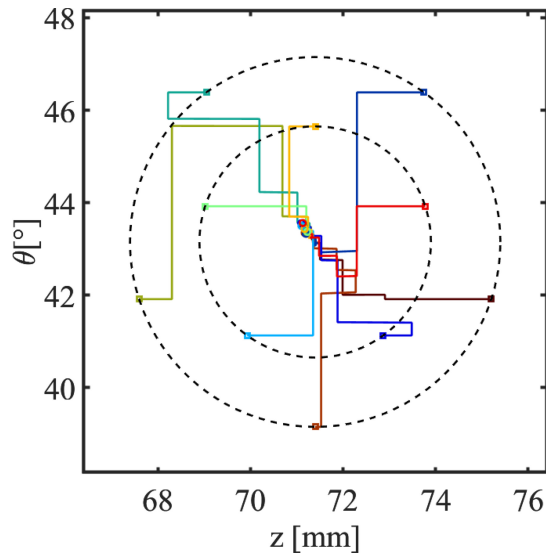


Figure 35: Convergence diagram of a combined calibration of both the tilt angle θ and the sample-detector distance z . The calibration alternates between 50 iterations of aPIE and 200 iterations of zPIE on experimental data with a structured beam illumination (cf. Fig. 34f). Each colored trajectory represents the convergence behaviour for a different initial estimate starting on the dashed circles. The reconstructions converged to $z = 71.16 \pm 0.04$ mm and $\theta = 43.37 \pm 0.06^\circ$.

demonstrated that despite of the explicit z -dependency of the underlying coordinate transformation, an alternating descent optimization of the tilt angle and detector-sample distance is feasible, even when neither parameter is known precisely. In summary, aPIE will improve the robustness and allow for tilt angle self-calibration in reflection-mode ptychography.

Funding. Nederlandse Organisatie voor Wetenschappelijk Onderzoek (NWO-HTSM project no. 13934), and ERC Consolidator Grant 3D-VIEW (ERC-CoG 864016).

Disclosures. The authors declare no conflicts of interest

Data Availability Statement Data underlying the results presented in this paper are not publicly available at this time but may be obtained from the authors upon reasonable request.

See Supplement 1 for supporting content.

BIBLIOGRAPHY

- [1] G. Youssef et al. "Cardiac sarcoidosis: applications of imaging in diagnosis and directing treatment." *Heart* 97.24 (2011), 2078. DOI: [10.1136/hrt.2011.226076](https://doi.org/10.1136/hrt.2011.226076).
- [2] T. Liu, H. Peng, and X. Zhou. "Imaging informatics for personalised medicine: applications and challenges." *Int J Funct Inform Personal Med* 2.2 (2009), 125. DOI: [10.1504/IJFIPM.2009.027587](https://doi.org/10.1504/IJFIPM.2009.027587).
- [3] J. H. Yim et al. "Rapid 3D-Imaging of Semiconductor Chips Using THz Time-of-Flight Technique." *Applied Sciences* 11.11 (2021), 4770. DOI: [10.3390/app11114770](https://doi.org/10.3390/app11114770).
- [4] C. Yoon et al. "Toward realization of high-throughput hyper-spectral imaging technique for semiconductor device metrology." *JM3* 21.2 (2022), 021209. DOI: [10.1117/1.JMM.21.2.021209](https://doi.org/10.1117/1.JMM.21.2.021209).
- [5] H. N. Chapman and K. A. Nugent. "Coherent lensless X-ray imaging." *Nature Photon* 4.12 (2010), 833. DOI: [10.1038/nphoton.2010.240](https://doi.org/10.1038/nphoton.2010.240).
- [6] G. B. Airy. "On the Diffraction of an Object-glass with Circular Aperture." *Transactions of the Cambridge Philosophical Society* (1835).
- [7] E. Abbe. "Beiträge zur Theorie des Mikroskops und der mikroskopischen Wahrnehmung." *Archiv f. mikrosk. Anatomie* 9.1 (1873), 413. DOI: [10.1007/BF02956173](https://doi.org/10.1007/BF02956173).
- [8] G. Huszka and M. A. M. Gijs. "Super-resolution optical imaging: A comparison." *Micro and Nano Engineering* 2 (2019), 7. DOI: [10.1016/j.mne.2018.11.005](https://doi.org/10.1016/j.mne.2018.11.005).
- [9] A. Lewis et al. "The optical near-field: super-resolution imaging with structural and phase correlation." *Nanophotonics* 3.1-2 (2014), 3. DOI: [10.1515/nanoph-2014-0007](https://doi.org/10.1515/nanoph-2014-0007).
- [10] S. T. Hess, T. P. K. Girirajan, and M. D. Mason. "Ultra-High Resolution Imaging by Fluorescence Photoactivation Localization Microscopy." *Biophysical Journal* 91.11 (2006), 4258. DOI: [10.1529/biophysj.106.091116](https://doi.org/10.1529/biophysj.106.091116).
- [11] M. J. Rust, M. Bates, and X. Zhuang. "Sub-diffraction-limit imaging by stochastic optical reconstruction microscopy (STORM)." *Nat Methods* 3.10 (2006), 793. DOI: [10.1038/nmeth929](https://doi.org/10.1038/nmeth929).
- [12] K. Rosfjord et al. "Direct index of refraction measurements at extreme-ultraviolet and soft-x-ray wavelengths." *Appl. Opt., AO* 45.8 (2006), 1730. DOI: [10.1364/AO.45.001730](https://doi.org/10.1364/AO.45.001730).

- [13] A. J. Fresnel. "Calcul de l'intensité de la lumière au centre de l'ombre d'un écran et d'une ouverture circulaires éclairés par un point radieux." *Œuvres Complètes d'Augustin Fresnel, Imprimerie Impériale, Paris* (1866).
- [14] I. Mohacsi et al. "Fabrication and characterization of high-efficiency double-sided blazed x-ray optics." *Opt. Lett.* 41.2 (2016), 281. DOI: [10.1364/OL.41.000281](https://doi.org/10.1364/OL.41.000281).
- [15] E. Fogelqvist et al. "Laboratory cryo x-ray microscopy for 3D cell imaging." *Sci Rep* 7.1 (2017), 13433. DOI: [10.1038/s41598-017-13538-2](https://doi.org/10.1038/s41598-017-13538-2).
- [16] H. Legall et al. "Compact x-ray microscope for the water window based on a high brightness laser plasma source." *Opt. Express* 20.16 (2012), 18362. DOI: [10.1364/OE.20.018362](https://doi.org/10.1364/OE.20.018362).
- [17] J. Kirz et al. "Soft x-ray microscopy with coherent x rays." *Review of Scientific Instruments* 63.1 (1992), 557. DOI: [10.1063/1.1142705](https://doi.org/10.1063/1.1142705).
- [18] J. C. H. Spence. "Diffractive Imaging of Single Particles." *Springer Handbook of Microscopy*. Ed. by P. W. Hawkes and J. C. H. Spence. Springer International Publishing, 2019, 1009. DOI: [10.1007/978-3-030-00069-1_20](https://doi.org/10.1007/978-3-030-00069-1_20).
- [19] J. R. Fienup and C. C. Wackerman. "Phase-retrieval stagnation problems and solutions." *J. Opt. Soc. Am. A* 3.11 (1986), 1897. DOI: [10.1364/JOSAA.3.001897](https://doi.org/10.1364/JOSAA.3.001897).
- [20] J. R. Fienup. "Reconstruction of an object from the modulus of its Fourier transform." *Opt. Lett.* 3.1 (1978), 27. DOI: [10.1364/OL.3.000027](https://doi.org/10.1364/OL.3.000027).
- [21] J. M. Rodenburg and H. M. L. Faulkner. "A phase retrieval algorithm for shifting illumination." *Appl. Phys. Lett.* 85.20 (2004), 4795. DOI: [10.1063/1.1823034](https://doi.org/10.1063/1.1823034).
- [22] A. M. Maiden and J. M. Rodenburg. "An improved ptychographical phase retrieval algorithm for diffractive imaging." *Ultramicroscopy* 109.10 (2009), 1256. DOI: [10.1016/j.ultramicro.2009.05.012](https://doi.org/10.1016/j.ultramicro.2009.05.012).
- [23] M. Du et al. "Measuring laser beam quality, wavefronts, and lens aberrations using ptychography." *Optics Express* 28.4 (2020), 5022. DOI: [10.1364/OE.385191](https://doi.org/10.1364/OE.385191).
- [24] P. Li and A. Maiden. "Multi-slice ptychographic tomography." *Sci Rep* 8.1 (2018), 2049. DOI: [10.1038/s41598-018-20530-x](https://doi.org/10.1038/s41598-018-20530-x).
- [25] L. Loetgering et al. "zPIE: an autofocusing algorithm for ptychography." *Opt. Lett.* 45.7 (2020), 2030. DOI: [10.1364/ol.389492](https://doi.org/10.1364/ol.389492).

- [26] P. Thibault and A. Menzel. "Reconstructing state mixtures from diffraction measurements." *Nature* 494.7435 (2013), 68. DOI: [10.1038/nature11806](https://doi.org/10.1038/nature11806).
- [27] M. Odstroil et al. "Ptychographic coherent diffractive imaging with orthogonal probe relaxation." *Opt. Express* 24.8 (2016), 8360. DOI: [10.1364/OE.24.008360](https://doi.org/10.1364/OE.24.008360).
- [28] D. J. Batey, D. Claus, and J. M. Rodenburg. "Information multiplexing in ptychography." *Ultramicroscopy* 138 (2014), 13. DOI: [10.1016/j.ultramic.2013.12.003](https://doi.org/10.1016/j.ultramic.2013.12.003).
- [29] L. Loetgering et al. "Tailoring spatial entropy in extreme ultraviolet focused beams for multispectral ptychography." *Optica* 8.2 (2021), 130. DOI: [10.1364/OPTICA.410007](https://doi.org/10.1364/OPTICA.410007).
- [30] Y. Jiang et al. "Electron ptychography of 2D materials to deep sub-ångström resolution." *Nature* 559.7714 (2018), 343. DOI: [10.1038/s41586-018-0298-5](https://doi.org/10.1038/s41586-018-0298-5).
- [31] P. C. Konda et al. "Fourier ptychography: current applications and future promises." *Opt. Express* 28.7 (2020), 9603. DOI: [10.1364/OE.386168](https://doi.org/10.1364/OE.386168).
- [32] L. Valzania et al. "THz coherent lensless imaging." *Appl. Opt.* 58.34 (2019), G256. DOI: [10.1364/AO.58.00G256](https://doi.org/10.1364/AO.58.00G256).
- [33] J. R. Fienup. "Phase retrieval algorithms: a comparison." *Appl. Opt.* 21.15 (1982), 2758. DOI: [10.1364/AO.21.002758](https://doi.org/10.1364/AO.21.002758).
- [34] T. E. H. T. Collaboration. "First M87 Event Horizon Telescope Results. IV. Imaging the Central Supermassive Black Hole." *ApJL* 875.1 (2019), L4. DOI: [10.3847/2041-8213/ab0e85](https://doi.org/10.3847/2041-8213/ab0e85).
- [35] K. L. Bouman et al. "Computational Imaging for VLBI Image Reconstruction." *arXiv:1512.01413 [astro-ph.IM]* (2016). arXiv: 1512.01413. DOI: <https://doi.org/10.48550/arXiv.1512.01413>.
- [36] M. Hirose et al. "Multibeam ptychography with synchrotron hard X-rays." *Opt. Express* 28.2 (2020), 1216. DOI: [10.1364/OE.378083](https://doi.org/10.1364/OE.378083).
- [37] A. Schropp et al. "Full spatial characterization of a nanofocused x-ray free-electron laser beam by ptychographic imaging." *Sci Rep* 3.1 (2013), 1633. DOI: [10.1038/srep01633](https://doi.org/10.1038/srep01633).
- [38] J. C. H. Spence. "XFELs for structure and dynamics in biology." *IUCr* 4.Pt 4 (2017), 322. DOI: [10.1107/S2052252517005760](https://doi.org/10.1107/S2052252517005760).
- [39] M. Dierolf et al. "Ptychographic X-ray computed tomography at the nanoscale." *Nature* 467.7314 (2010), 436. DOI: [10.1038/nature09419](https://doi.org/10.1038/nature09419).
- [40] M. Holler et al. "High-resolution non-destructive three-dimensional imaging of integrated circuits." *Nature* 543.7645 (2017), 402. DOI: [10.1038/nature21698](https://doi.org/10.1038/nature21698).

- [41] H. V. Le et al. "Generation of highly coherent extreme ultraviolet source and its application in diffraction imaging." *Results in Physics* 4 (2014), 113. DOI: [10.1016/j.rinp.2014.07.008](https://doi.org/10.1016/j.rinp.2014.07.008).
- [42] S. Zayko et al. "Ultrafast high-harmonic nanoscopy of magnetization dynamics." *Nat Commun* 12.1 (2021), 6337. DOI: [10.1038/s41467-021-26594-0](https://doi.org/10.1038/s41467-021-26594-0).
- [43] P. D. Baksh et al. "Quantitative and correlative extreme ultraviolet coherent imaging of mouse hippocampal neurons at high resolution." *Science Advances* 6.18 (2020), eaaz3025. DOI: [10.1126/sciadv.aaz3025](https://doi.org/10.1126/sciadv.aaz3025).
- [44] P.-A. Chevreuril et al. "Water-window high harmonic generation with 0.8- μm and 2.2- μm OPCPAs at 100 kHz." *Opt. Express* 29.21 (2021), 32996. DOI: [10.1364/OE.440273](https://doi.org/10.1364/OE.440273).
- [45] T. Popmintchev et al. "Phase matching of high harmonic generation in the soft and hard X-ray regions of the spectrum." *Proceedings of the National Academy of Sciences* 106.26 (2009), 10516. DOI: [10.1073/pnas.0903748106](https://doi.org/10.1073/pnas.0903748106).
- [46] D. F. Gardner et al. "Subwavelength coherent imaging of periodic samples using a 13.5 nm tabletop high-harmonic light source." *Nature Photon* 11.4 (2017), 259. DOI: [10.1038/nphoton.2017.33](https://doi.org/10.1038/nphoton.2017.33).
- [47] M. Tanksalvala et al. "Nondestructive, high-resolution, chemically specific 3D nanostructure characterization using phase-sensitive EUV imaging reflectometry." *Science Advances* 7.5 (2021), eabd9667. DOI: [10.1126/sciadv.abd9667](https://doi.org/10.1126/sciadv.abd9667).
- [48] F. Zernike. "How I Discovered Phase Contrast." *Science* 121.3141 (1955), 345. DOI: [10.1126/science.121.3141.345](https://doi.org/10.1126/science.121.3141.345).
- [49] Y. Park, C. Depeursinge, and G. Popescu. "Quantitative phase imaging in biomedicine." *Nature Photon* 12.10 (2018), 578. DOI: [10.1038/s41566-018-0253-x](https://doi.org/10.1038/s41566-018-0253-x).
- [50] D. Gabor. "A New Microscopic Principle." *Nature* 161.4098 (1948), 777. DOI: [10.1038/161777a0](https://doi.org/10.1038/161777a0).
- [51] A. F. H. Goetz et al. "Imaging Spectrometry for Earth Remote Sensing." *Science* 228.4704 (1985), 1147. DOI: [10.1126/science.228.4704.1147](https://doi.org/10.1126/science.228.4704.1147).
- [52] *Imaging Spectrometry*. 4. Springer International Publishing, 2001.
- [53] A. E. Cerussi et al. "Diffuse optical spectroscopic imaging correlates with final pathological response in breast cancer neoadjuvant chemotherapy." *Philos Trans A Math Phys Eng Sci* 369.1955 (2011), 4512. DOI: [10.1098/rsta.2011.0279](https://doi.org/10.1098/rsta.2011.0279).

- [54] V. Hill et al. "VLT/FLAMES high-resolution chemical abundances in Sculptor: a textbook dwarf spheroidal galaxy." *Astronomy & Astrophysics* 626.A15 (2019), 23 pp. DOI: [10.1051/0004-6361/201833950](https://doi.org/10.1051/0004-6361/201833950).
- [55] V. Almendros-Abad et al. "Youth analysis of near-infrared spectra of young low-mass stars and brown dwarfs." *A&A* 657 (2022), A129. DOI: [10.1051/0004-6361/202142050](https://doi.org/10.1051/0004-6361/202142050).
- [56] P. Qi et al. "Wide field imaging energy dispersive X-ray absorption spectroscopy." *Sci Rep* 9.1 (2019), 17734. DOI: [10.1038/s41598-019-54287-8](https://doi.org/10.1038/s41598-019-54287-8).
- [57] M. C. Veale et al. "HEXITEC: A High-Energy X-ray Spectroscopic Imaging Detector for Synchrotron Applications." *Synchrotron Radiation News* 31.6 (2018), 28. DOI: [10.1080/08940886.2018.1528431](https://doi.org/10.1080/08940886.2018.1528431).
- [58] B. Zhang et al. "Ptychographic hyperspectral spectromicroscopy with an extreme ultraviolet high harmonic comb." *Opt. Express* 24.16 (2016), 18745. DOI: [10.1364/OE.24.018745](https://doi.org/10.1364/OE.24.018745).
- [59] K. Itoh and Y. Ohtsuka. "Fourier-transform spectral imaging: retrieval of source information from three-dimensional spatial coherence." *J. Opt. Soc. Am. A* 3.1 (1986), 94. DOI: [10.1364/JOSAA.3.000094](https://doi.org/10.1364/JOSAA.3.000094).
- [60] A. S. Iacchetta and J. R. Fienup. "Wide-field spatio-spectral interferometry: theory and imaging properties." *J. Opt. Soc. Am. A* 34.10 (2017), 1896. DOI: [10.1364/JOSAA.34.001896](https://doi.org/10.1364/JOSAA.34.001896).
- [61] G. Kirchhoff. "Zur Theorie der Lichtstrahlen." *Annalen der Physik* 254.4 (1883), 663. DOI: [10.1002/andp.18832540409](https://doi.org/10.1002/andp.18832540409).
- [62] A. Sommerfeld. "Mathematische Theorie der Diffraction." *Math. Ann.* 47.2 (1896), 317. DOI: [10.1007/BF01447273](https://doi.org/10.1007/BF01447273).
- [63] G. C. Sherman. "Application of the Convolution Theorem to Rayleigh's Integral Formulas." *J. Opt. Soc. Am.* 57.4 (1967), 546. DOI: [10.1364/JOSA.57.000546](https://doi.org/10.1364/JOSA.57.000546).
- [64] J. W. Goodman. *Introduction to Fourier Optics*. W. H. Freeman, 1968.
- [65] K. Paturski. "Fraunhofer Diffraction Patterns of Tilted Planar Objects." *Optica Acta: International Journal of Optics* 30.5 (1983), 673. DOI: [10.1080/713821241](https://doi.org/10.1080/713821241).
- [66] H. Rabal, N. Bolognini, and E. Sicre. "Diffraction by a Tilted Aperture." *Optica Acta: International Journal of Optics* 32.11 (1985), 1309. DOI: [10.1080/713821668](https://doi.org/10.1080/713821668).
- [67] D. Leseberg and C. Frère. "Computer-generated holograms of 3-D objects composed of tilted planar segments." *Appl. Opt., AO* 27.14 (1988), 3020. DOI: [10.1364/AO.27.003020](https://doi.org/10.1364/AO.27.003020).

- [68] K. Matsushima, H. Schimmel, and F. Wyrowski. "Fast calculation method for optical diffraction on tilted planes by use of the angular spectrum of plane waves." *J. Opt. Soc. Am. A* 20.9 (2003), 1755. DOI: [10.1364/JOSAA.20.001755](https://doi.org/10.1364/JOSAA.20.001755).
- [69] E. N. Leith and J. Upatnieks. "Reconstructed Wavefronts and Communication Theory*." *J. Opt. Soc. Am.* 52.10 (1962), 1123. DOI: [10.1364/JOSA.52.001123](https://doi.org/10.1364/JOSA.52.001123).
- [70] J. W. Goodman and R. W. Lawrence. "Digital image formation from electronically detected holograms." *Appl. Phys. Lett.* 11.3 (1967), 77. DOI: [10.1063/1.1755043](https://doi.org/10.1063/1.1755043).
- [71] T. Tahara et al. "Digital holography and its multidimensional imaging applications: a review." *Microscopy* 67.2 (2018), 55. DOI: [10.1093/jmicro/dfy007](https://doi.org/10.1093/jmicro/dfy007).
- [72] W. Hoppe and J. Gassmann. "Phase correction, a new method to solve partially known structures." *Acta Crystallographica Section B* 24.1 (1968), 97. DOI: [10.1107/S0567740868001755](https://doi.org/10.1107/S0567740868001755).
- [73] R. P. Millane. "Phase retrieval in crystallography and optics." *J. Opt. Soc. Am. A* 7.3 (1990), 394. DOI: [10.1364/JOSAA.7.000394](https://doi.org/10.1364/JOSAA.7.000394).
- [74] D. Sayre. "Some implications of a theorem due to Shannon." *Acta Cryst* 5.6 (1952), 843. DOI: [10.1107/S0365110X52002276](https://doi.org/10.1107/S0365110X52002276).
- [75] R. W. Gerchberg and W. Saxton. "A practical algorithm for the determination of the phase from image and diffraction plane pictures." *Optik* 35 (1972), 237.
- [76] Y. M. Bruck and L. G. Sodin. "On the ambiguity of the image reconstruction problem." *Optics Communications* 30.3 (1979), 304. DOI: [10.1016/0030-4018\(79\)90358-4](https://doi.org/10.1016/0030-4018(79)90358-4).
- [77] R. H. T. Bates. "Fourier phase problems are uniquely solvable in more than one dimension. I: Underlying theory," *Optik* 61 (1982), 247.
- [78] R. H. T. Bates. "Uniqueness of solutions to two-dimensional fourier phase problems for localized and positive images." *Computer Vision, Graphics, and Image Processing* 25.2 (1984), 205. DOI: [10.1016/0734-189X\(84\)90103-8](https://doi.org/10.1016/0734-189X(84)90103-8).
- [79] J. Miao et al. "Extending the methodology of X-ray crystallography to allow imaging of micrometre-sized non-crystalline specimens." *Nature* 400.6742 (1999), 342. DOI: [10.1038/22498](https://doi.org/10.1038/22498).
- [80] S. Marchesini et al. "X-ray image reconstruction from a diffraction pattern alone." *Phys. Rev. B* 68.14 (2003), 140101. DOI: [10.1103/PhysRevB.68.140101](https://doi.org/10.1103/PhysRevB.68.140101).
- [81] E. S. Ameh. "A review of basic crystallography and x-ray diffraction applications." *Int J Adv Manuf Technol* 105.7 (2019), 3289. DOI: [10.1007/s00170-019-04508-1](https://doi.org/10.1007/s00170-019-04508-1).

- [82] V. Elser. "Phase retrieval by iterated projections." *J. Opt. Soc. Am. A* 20.1 (2003), 40. DOI: [10.1364/JOSAA.20.000040](https://doi.org/10.1364/JOSAA.20.000040).
- [83] J. Rodenburg. "Ptychography and Related Diffractive Imaging Methods." *Advances in Imaging and Electron Physics*. Vol. 150. Elsevier, 2008, 87. DOI: [10.1016/S1076-5670\(07\)00003-1](https://doi.org/10.1016/S1076-5670(07)00003-1).
- [84] J. Rodenburg and A. Maiden. "Ptychography." *Springer Handbook of Microscopy*. Ed. by P. W. Hawkes and J. C. H. Spence. Springer International Publishing, 2019, 819. DOI: [10.1007/978-3-030-00069-1_17](https://doi.org/10.1007/978-3-030-00069-1_17).
- [85] W. Hoppe. "Beugung im inhomogenen Primärstrahlwellenfeld. I. Prinzip einer Phasenmessung von Elektronenbeugungsinterferenzen." *Acta Crystallographica Section A* 25.4 (1969), 495. DOI: [10.1107/S0567739469001045](https://doi.org/10.1107/S0567739469001045).
- [86] M. Du. "Computational Depth-resolved Imaging and Metrology." PhD-Thesis. Amsterdam, 2021.
- [87] J. M. Rodenburg and R. H. T. Bates. "The theory of super-resolution electron microscopy via Wigner-distribution deconvolution." *Philosophical Transactions of the Royal Society of London. Series A: Physical and Engineering Sciences* 339.1655 (1992), 521. DOI: [10.1098/rsta.1992.0050](https://doi.org/10.1098/rsta.1992.0050).
- [88] H. N. Chapman. "Phase-retrieval X-ray microscopy by Wigner-distribution deconvolution." *Ultramicroscopy* 66.3 (1996), 153. DOI: [10.1016/S0304-3991\(96\)00084-8](https://doi.org/10.1016/S0304-3991(96)00084-8).
- [89] P. Li, T. B. Edo, and J. M. Rodenburg. "Ptychographic inversion via Wigner distribution deconvolution: Noise suppression and probe design." *Ultramicroscopy* 147 (2014), 106. DOI: [10.1016/j.ultramic.2014.07.004](https://doi.org/10.1016/j.ultramic.2014.07.004).
- [90] H. Yang et al. "Electron ptychographic phase imaging of light elements in crystalline materials using Wigner distribution deconvolution." *Ultramicroscopy* 180 (2017), 173. DOI: [10.1016/j.ultramic.2017.02.006](https://doi.org/10.1016/j.ultramic.2017.02.006).
- [91] A. Maiden, D. Johnson, and P. Li. "Further improvements to the ptychographical iterative engine." *Optica* 4.7 (2017), 736. DOI: [10.1364/OPTICA.4.000736](https://doi.org/10.1364/OPTICA.4.000736).
- [92] M. Odstrčil et al. "Towards optimized illumination for high-resolution ptychography." *Opt. Express* 27.10 (2019), 14981. DOI: [10.1364/OE.27.014981](https://doi.org/10.1364/OE.27.014981).
- [93] M. Guizar-Sicairos et al. "Role of the illumination spatial-frequency spectrum for ptychography." *Phys. Rev. B* 86.10 (2012), 100103. DOI: [10.1103/PhysRevB.86.100103](https://doi.org/10.1103/PhysRevB.86.100103).
- [94] P. Dwivedi et al. "Lateral position correction in ptychography using the gradient of intensity patterns." *Ultramicroscopy* 192 (2018), 29. DOI: [10.1016/j.ultramic.2018.04.004](https://doi.org/10.1016/j.ultramic.2018.04.004).

- [95] G. Zheng, R. Horstmeyer, and C. Yang. "Wide-field, high-resolution Fourier ptychographic microscopy." *Nature Photon* 7.9 (2013), 739. DOI: [10.1038/nphoton.2013.187](https://doi.org/10.1038/nphoton.2013.187).
- [96] K. Kreutz-Delgado. "The Complex Gradient Operator and the CR-Calculus." *arXiv:0906.4835* (2009). DOI: <https://doi.org/10.48550/arXiv.0906.4835>.
- [97] W. Wirtinger. "Zur formalen Theorie der Funktionen von mehr komplexen Veränderlichen." *Mathematische Annalen* 97 (1927), 357.
- [98] B. T. Polyak. "Some methods of speeding up the convergence of iteration methods." *USSR Computational Mathematics and Mathematical Physics* 4.5 (1964), 1. DOI: [10.1016/0041-5553\(64\)90137-5](https://doi.org/10.1016/0041-5553(64)90137-5).
- [99] I. Sutskever et al. "On the importance of initialization and momentum in deep learning." *Proceedings of the 30th International Conference on Machine Learning*. 2013, 1139.
- [100] Y. Nesterov. "A method of solving a convex programming problem with convergence rate $\mathcal{O}(1/k^2)$." *Sov. Math. Dokl.* 27.3 (1983), 543.
- [101] A. Defazio. *Momentum via Primal Averaging: Theoretical Insights and Learning Rate Schedules for Non-Convex Optimization*. 2021. DOI: [10.48550/arXiv.2010.00406](https://doi.org/10.48550/arXiv.2010.00406).
- [102] J. Mariotti and S. Ridgway. "Double Fourier spatio-spectral interferometry—combining high spectral and high spatial resolution in the near infrared," *Astronomy and Astrophysics* 195.1-2 (1988), 350.
- [103] A. P. Konijnenberg et al. "Phase retrieval algorithms for lensless imaging using diffractive shearing interferometry." *J. Opt. Soc. Am. A* 37.6 (2020), 914. DOI: [10.1364/JOSAA.389791](https://doi.org/10.1364/JOSAA.389791).
- [104] J. Spence, U. Weierstall, and M. Howells. "Coherence and sampling requirements for diffractive imaging." *Ultramicroscopy* 101.2-4 (2004), 149. DOI: [10.1016/j.ultramic.2004.05.005](https://doi.org/10.1016/j.ultramic.2004.05.005).
- [105] T. B. Edø et al. "Sampling in x-ray ptychography." *Phys. Rev. A* 87.5 (2013), 053850. DOI: [10.1103/PhysRevA.87.053850](https://doi.org/10.1103/PhysRevA.87.053850).
- [106] F. Zernike. "The concept of degree of coherence and its application to optical problems." *Physica* 5.8 (1938), 785. DOI: [10.1016/S0031-8914\(38\)80203-2](https://doi.org/10.1016/S0031-8914(38)80203-2).
- [107] E. Wolf. "A new description of second-order coherence phenomena in the space-frequency domain." *AIP Conference Proceedings* 65.1 (2008), 42. DOI: [10.1063/1.32286](https://doi.org/10.1063/1.32286).

- [108] S. Witte and K. S. E. Eikema. "Ultrafast Optical Parametric Chirped-Pulse Amplification." *IEEE Journal of Selected Topics in Quantum Electronics* 18.1 (2012), 296. DOI: [10.1109/JSTQE.2011.2118370](https://doi.org/10.1109/JSTQE.2011.2118370).
- [109] P. B. Corkum. "Plasma perspective on strong field multiphoton ionization." *Phys. Rev. Lett.* 71.13 (1993), 1994. DOI: [10.1103/PhysRevLett.71.1994](https://doi.org/10.1103/PhysRevLett.71.1994).
- [110] M. Lewenstein et al. "Theory of high-harmonic generation by low-frequency laser fields." *Phys. Rev. A* 49.3 (1994), 2117. DOI: [10.1103/PhysRevA.49.2117](https://doi.org/10.1103/PhysRevA.49.2117).
- [111] S. Kazamias et al. "Pressure-induced phase matching in high-order harmonic generation." *Phys. Rev. A* 83.6 (2011), 063405. DOI: [10.1103/PhysRevA.83.063405](https://doi.org/10.1103/PhysRevA.83.063405).
- [112] D. E. Spence, P. N. Kean, and W. Sibbett. "60-fsec pulse generation from a self-mode-locked Ti:sapphire laser." *Opt. Lett.* 16.1 (1991), 42. DOI: [10.1364/OL.16.000042](https://doi.org/10.1364/OL.16.000042).
- [113] S. Backus et al. "High power ultrafast lasers." *Review of Scientific Instruments* 69.3 (1998), 1207. DOI: [10.1063/1.1148795](https://doi.org/10.1063/1.1148795).
- [114] R. Ell et al. "Generation of 5-fs pulses and octave-spanning spectra directly from a Ti:sapphire laser." *Opt. Lett.* 26.6 (2001), 373. DOI: [10.1364/OL.26.000373](https://doi.org/10.1364/OL.26.000373).
- [115] D. S. McClure. "Optical Spectra of Transition-Metal Ions in Corundum." *J. Chem. Phys.* 36.10 (1962), 2757. DOI: [10.1063/1.1732364](https://doi.org/10.1063/1.1732364).
- [116] P. W. Roth et al. "Directly diode-laser-pumped Ti:sapphire laser." *Opt. Lett.* 34.21 (2009), 3334. DOI: [10.1364/OL.34.003334](https://doi.org/10.1364/OL.34.003334).
- [117] S. Backus et al. "Direct diode pumped Ti:sapphire ultrafast regenerative amplifier system." *Opt. Express* 25.4 (2017), 3666. DOI: [10.1364/OE.25.003666](https://doi.org/10.1364/OE.25.003666).
- [118] J. Kerr. "A new relation between electricity and light: Dielectric media birefringent." *The London, Edinburgh, and Dublin Philosophical Magazine and Journal of Science* 50.332 (1875), 337. DOI: [10.1080/14786447508641302](https://doi.org/10.1080/14786447508641302).
- [119] F. Salin, J. Squier, and M. Piché. "Mode locking of Ti:Al₂O₃ lasers and self-focusing: a Gaussian approximation." *Opt. Lett.* 16.21 (1991), 1674. DOI: [10.1364/OL.16.001674](https://doi.org/10.1364/OL.16.001674).
- [120] R. Szipöcs et al. "Chirped multilayer coatings for broadband dispersion control in femtosecond lasers." *Opt. Lett.* 19.3 (1994), 201. DOI: [10.1364/OL.19.000201](https://doi.org/10.1364/OL.19.000201).
- [121] A. Stingl et al. "Sub-10-fs mirror-dispersion-controlled Ti:sapphire laser." *Opt. Lett.* 20.6 (1995), 602. DOI: [10.1364/OL.20.000602](https://doi.org/10.1364/OL.20.000602).

- [122] P. F. Moulton. "Spectroscopic and laser characteristics of Ti:Al₂O₃." *J. Opt. Soc. Am. B* 3.1 (1986), 125. DOI: [10.1364/JOSAB.3.000125](https://doi.org/10.1364/JOSAB.3.000125).
- [123] J. Morgenweg and K. S. E. Eikema. "A 1.8 mJ, picosecond Nd:YVO₄ bounce amplifier pump front-end system for high-accuracy XUV-frequency comb spectroscopy." *Laser Phys. Lett.* 9.11 (2012), 781. DOI: [10.7452/lapl.201210079](https://doi.org/10.7452/lapl.201210079).
- [124] J. E. Bernard and A. J. Alcock. "High-efficiency diode-pumped Nd:YVO₄ slab laser." *Opt. Lett.* 18.12 (1993), 968. DOI: [10.1364/OL.18.000968](https://doi.org/10.1364/OL.18.000968).
- [125] D. W. E. Noom et al. "High-energy, high-repetition-rate picosecond pulses from a quasi-CW diode-pumped Nd:YAG system." *Opt. Lett.* 38.16 (2013), 3021. DOI: [10.1364/OL.38.003021](https://doi.org/10.1364/OL.38.003021).
- [126] W. C. Scott and M. de Wit. "BIREFRINGENCE COMPENSATION AND TEM₀₀ MODE ENHANCEMENT IN A Nd: YAG LASER." *Appl. Phys. Lett.* 18.1 (1971), 3. DOI: [10.1063/1.1653466](https://doi.org/10.1063/1.1653466).
- [127] G. Jansen. "Wavelength-resolved Extreme Ultraviolet Lensless Imaging and Metrology." PhD-Thesis. 2020.
- [128] D. Kane and R. Trebino. "Characterization of arbitrary femtosecond pulses using frequency-resolved optical gating." *IEEE Journal of Quantum Electronics* 29.2 (1993), 571. DOI: [10.1109/3.199311](https://doi.org/10.1109/3.199311).
- [129] G. S. M. Jansen et al. "Spatially resolved Fourier transform spectroscopy in the extreme ultraviolet." *Optica* 3.10 (2016), 1122. DOI: [10.1364/OPTICA.3.001122](https://doi.org/10.1364/OPTICA.3.001122).
- [130] D. Shapiro et al. "Biological imaging by soft x-ray diffraction microscopy." *Proc. Natl. Acad. Sci. U.S.A.* 102.43 (2005), 15343. DOI: [10.1073/pnas.0503305102](https://doi.org/10.1073/pnas.0503305102).
- [131] M. Zürch et al. "Real-time and Sub-wavelength Ultrafast Coherent Diffraction Imaging in the Extreme Ultraviolet." *Sci Rep* 4.1 (2014), 7356. DOI: [10.1038/srep07356](https://doi.org/10.1038/srep07356).
- [132] W. J. Huang et al. "Sub-ångström-resolution diffractive imaging of single nanocrystals." *Nature Phys* 5.2 (2009), 129. DOI: [10.1038/nphys1161](https://doi.org/10.1038/nphys1161).
- [133] A. V. Martin et al. "Noise-robust coherent diffractive imaging with a single diffraction pattern." *Opt. Express* 20.15 (2012), 16650. DOI: [10.1364/OE.20.016650](https://doi.org/10.1364/OE.20.016650).
- [134] P. Thibault et al. "High-Resolution Scanning X-ray Diffraction Microscopy." *Science* 321.5887 (2008), 379. DOI: [10.1126/science.1158573](https://doi.org/10.1126/science.1158573).

- [135] V. T. Tenner, K. S. E. Eikema, and S. Witte. "Fourier transform holography with extended references using a coherent ultra-broadband light source." *Opt. Express* 22.21 (2014), 25397. DOI: [10.1364/OE.22.025397](https://doi.org/10.1364/OE.22.025397).
- [136] S. Eisebitt et al. "Lensless imaging of magnetic nanostructures by X-ray spectro-holography." *Nature* 432.7019 (2004), 885. DOI: [10.1038/nature03139](https://doi.org/10.1038/nature03139).
- [137] R. L. Sandberg et al. "Tabletop soft-x-ray Fourier transform holography with 50 nm resolution." *Opt. Lett.* 34.11 (2009), 1618. DOI: [10.1364/OL.34.001618](https://doi.org/10.1364/OL.34.001618).
- [138] D. Gauthier et al. "Single-shot Femtosecond X-Ray Holography Using Extended References." *Phys. Rev. Lett.* 105.9 (2010), 093901. DOI: [10.1103/PhysRevLett.105.093901](https://doi.org/10.1103/PhysRevLett.105.093901).
- [139] M. E. Riley and M. A. Gusinow. "Laser beam divergence utilizing a lateral shearing interferometer." *Appl. Opt.* 16.10 (1977), 2753. DOI: [10.1364/AO.16.002753](https://doi.org/10.1364/AO.16.002753).
- [140] D. R. Austin et al. "Lateral shearing interferometry of high-harmonic wavefronts." *Opt. Lett.* 36.10 (2011), 1746. DOI: [10.1364/OL.36.001746](https://doi.org/10.1364/OL.36.001746).
- [141] C. Falldorf, C. v. Kopylow, and R. B. Bergmann. "Wave field sensing by means of computational shear interferometry." *J. Opt. Soc. Am. A* 30.10 (2013), 1905. DOI: [10.1364/JOSAA.30.001905](https://doi.org/10.1364/JOSAA.30.001905).
- [142] S. Witte et al. "Lensless diffractive imaging with ultra-broadband table-top sources: from infrared to extreme-ultraviolet wavelengths." *Light Sci Appl* 3.3 (2014), e163. DOI: [10.1038/lsa.2014.44](https://doi.org/10.1038/lsa.2014.44).
- [143] L. Loetgering et al. "Phase retrieval via propagation-based interferometry." *Phys. Rev. A* 95.3 (2017), 033819. DOI: [10.1103/PhysRevA.95.033819](https://doi.org/10.1103/PhysRevA.95.033819).
- [144] S. Marchesini. "Invited Article: A unified evaluation of iterative projection algorithms for phase retrieval." *Review of Scientific Instruments* 78.1 (2007), 011301. DOI: [10.1063/1.2403783](https://doi.org/10.1063/1.2403783).
- [145] F. Capotondi et al. "A scheme for lensless X-ray microscopy combining coherent diffraction imaging and differential corner holography." *Opt. Express* 20.22 (2012), 25152. DOI: [10.1364/OE.20.025152](https://doi.org/10.1364/OE.20.025152).
- [146] R. A. Bartels et al. "Generation of Spatially Coherent Light at Extreme Ultraviolet Wavelengths." *Science* 297.5580 (2002), 376. DOI: [10.1126/science.1071718](https://doi.org/10.1126/science.1071718).
- [147] G. S. M. Jansen et al. "Diffractive shear interferometry for extreme ultraviolet high-resolution lensless imaging." *Opt. Express* 26.10 (2018), 12479. DOI: [10.1364/OE.26.012479](https://doi.org/10.1364/OE.26.012479).

- [148] Y. Meng et al. "Octave-spanning hyperspectral coherent diffractive imaging in the extreme ultraviolet range." *Opt. Express* 23.22 (2015), 28960. DOI: [10.1364/OE.23.028960](https://doi.org/10.1364/OE.23.028960).
- [149] H. Wang et al. "Phase imaging with rotating illumination." *Chin. Opt. Lett.* 12.1 (2014), 010501.
- [150] D. E. Boonzajer Flaes and S. Witte. "Interference probe ptychography for computational amplitude and phase microscopy." *Opt. Express* 26.24 (2018), 31372. DOI: [10.1364/OE.26.031372](https://doi.org/10.1364/OE.26.031372).
- [151] I. Harder, J. Schwider, and N. Lindlein. "DUV-Shearing Interferometer with reduced spatial coherence." *DGaO Proc.* (2005).
- [152] T. Weitkamp et al. "X-ray phase imaging with a grating interferometer." *Opt. Express* 13.16 (2005), 6296. DOI: [10.1364/OPEX.13.006296](https://doi.org/10.1364/OPEX.13.006296).
- [153] K. G. Larkin, M. A. Oldfield, and H. Klemm. "Fast Fourier method for the accurate rotation of sampled images." *Optics Communications* 139.1-3 (1997), 99. DOI: [10.1016/S0030-4018\(97\)00097-7](https://doi.org/10.1016/S0030-4018(97)00097-7).
- [154] J. R. Fienup. "Invariant error metrics for image reconstruction." *Appl. Opt.* 36.32 (1997), 8352. DOI: [10.1364/AO.36.008352](https://doi.org/10.1364/AO.36.008352).
- [155] F. Pfeiffer. "X-ray ptychography." *Nature Photonics* 12.1 (2018), 9. DOI: [10.1038/s41566-017-0072-5](https://doi.org/10.1038/s41566-017-0072-5).
- [156] F. Hüe et al. "Wave-front phase retrieval in transmission electron microscopy via ptychography." *Physical Review B - Condensed Matter and Materials Physics* 82.12 (2010), 121415. DOI: [10.1103/PhysRevB.82.121415](https://doi.org/10.1103/PhysRevB.82.121415).
- [157] J. Marrison et al. "Ptychography – a label free, high-contrast imaging technique for live cells using quantitative phase information." *Sci Rep* 3.1 (2013), 2369. DOI: [10.1038/srep02369](https://doi.org/10.1038/srep02369).
- [158] N. Anthony et al. "Ptychographic imaging of NaD1 induced yeast cell death." *Biomed. Opt. Express* 10.10 (2019), 4964. DOI: [10.1364/B0E.10.004964](https://doi.org/10.1364/B0E.10.004964).
- [159] M. Guizar-Sicairos and J. R. Fienup. "Direct image reconstruction from a Fourier intensity pattern using HERALDO." *Opt. Lett.* 33.22 (2008), 2668. DOI: [10.1364/OL.33.002668](https://doi.org/10.1364/OL.33.002668).
- [160] A. M. Maiden et al. "An annealing algorithm to correct positioning errors in ptychography." *Ultramicroscopy* 120 (2012), 64. DOI: [10.1016/j.ultramic.2012.06.001](https://doi.org/10.1016/j.ultramic.2012.06.001).
- [161] E. H. R. Tsai et al. "X-ray ptychography with extended depth of field." *Optics Express* 24.25 (2016), 29089. DOI: [10.1364/OE.24.029089](https://doi.org/10.1364/OE.24.029089).

- [162] M. D. Seaberg et al. "Tabletop nanometer extreme ultraviolet imaging in an extended reflection mode using coherent Fresnel ptychography." *Optica* 1.1 (2014), 39. DOI: [10.1364/OPTICA.1.000039](https://doi.org/10.1364/OPTICA.1.000039).
- [163] D. F. Gardner et al. "High numerical aperture reflection mode coherent diffraction microscopy using off-axis apertured illumination." *Opt. Express* 20.17 (2012), 19050. DOI: [10.1364/OE.20.019050](https://doi.org/10.1364/OE.20.019050).
- [164] I. Skorokhodov. "Interpolating Points on a Non-Uniform Grid using a Mixture of Gaussians." *arXiv:2012.13257 [cs]* (2020). DOI: <https://doi.org/10.48550/arXiv.2012.13257>.
- [165] D. W. Zingg and M. Yarrow. "A method of smooth bivariate interpolation for data given on a generalized curvilinear grid." *SIAM journal on scientific and statistical computing* 13.3 (1992), 687.
- [166] R. E. Woods, S. L. Eddins, and R. C. Gonzalez. *Digital image processing using MATLAB*. 2nd. Gatesmark, 2009.
- [167] R. Luus and T. H. I. Jaakola. "Optimization by direct search and systematic reduction of the size of search region." *AIChE Journal* 19.4 (1973), 760. DOI: [10.1002/aic.690190413](https://doi.org/10.1002/aic.690190413).
- [168] D. Goldberg. "What every computer scientist should know about floating-point arithmetic." *ACM computing surveys (CSUR)* 23.1 (1991), 5.

LIST OF PUBLICATIONS

This work is based on the following publications:

Chapter 5:

G. S. M. Jansen, A. C. C. de Beurs, X. Liu, K. S. E. Eikema, and S. Witte, *Diffraction Shear interferometry for extreme ultra-violet high-resolution lensless imaging*, Opt. Express **26**, 12479-12489 (2018).

Author contributions:

G. S. M. Jansen, A. C. C. de Beurs, K. S. E. Eikema and S. Witte designed research.

G. S. M. Jansen fabricated the samples.

G. S. M. Jansen and A. C. C. de Beurs and X. Liu performed experiments.

A. C. C. de Beurs and G. S. M. Jansen developed analysis codes and performed data analysis.

K. S. E. Eikema and S. Witte supervised research

All authors discussed results and contributed to interpreting the results and the writing the manuscript.

Chapter 6:

A. C. C. de Beurs, X. Liu, G. S. M. Jansen, A. P. Konijnenberg, W. M. J. Coene, K. S. E. Eikema, and S. Witte, *Extreme ultraviolet lensless imaging without object support through rotational diversity in diffractive shearing interferometry*, Opt. Express **28**, 5257-5266 (2020).

Author contributions:

A. C. C. de Beurs, K. S. E. Eikema and S. Witte designed research.

A. C. C. de Beurs and X. Liu fabricated the samples.

A. C. C. de Beurs, X. Liu and G. S. M. Jansen performed experiments.

A. C. C. de Beurs developed analysis codes and performed data analysis.

A. C. C. de Beurs, X. Liu, G. S. M. Jansen, A. P. Konijnenberg, W. M. J. Coene, K. S. E. Eikema, and S. Witte interpreted data, developed image reconstruction concepts, and tested algorithms.

W. M. J. Coene, K. S. E. Eikema, and S. Witte supervised research.

A. C. C. de Beurs, X. Liu, G. S. M. Jansen, K. S. E. Eikema, and S. Witte

wrote the manuscript, which was reviewed and edited by all.

Chapter 7:

A. C. C. de Beurs, L. Loetgering, M. Herczog, M. Du, K. S. E. Eikema and S. Witte, *aPIE: an angle calibration algorithm for reflection ptychography*, *Opt. Lett.* **47**, 1949-1952 (2022).

Author contributions:

A. C. C. de Beurs, L. Loetgering and S. Witte designed research.
L. Loetgering performed experiments.
A. C. C. de Beurs, L. Loetgering, M. Du and S. Witte derived the angle correction approach.
A. C. C. de Beurs, L. Loetgering, M. Herczog, M. Du developed ptychography codes.
A. C. C. de Beurs and L. Loetgering performed data analysis.
K. S. E. Eikema and S. Witte supervised research.

All authors discussed results and contributed to interpreting the results and the writing the manuscript.

Other papers contributions:

In addition, the author has contributed to the following works:

L. Loetgering, X. Liu, A. C. C. De Beurs, M. Du, G. Kuijper, K. S. E. Eikema, S. Witte, *Tailoring spatial entropy in extreme ultraviolet focused beams for multispectral ptychography*, *Optica* **8**, 130-138 (2021).

A. P. Konijnenberg, A. C. C. de Beurs, G. S. M. Jansen, H. P. Urbach, S. Witte, and W. M. J. Coene, *Phase retrieval algorithms for lensless imaging using diffractive shearing interferometry*, *J. Opt. Soc. Am. A* **37**, 914-924 (2020)

Part II

APPENDIX

APPENDIX A

A.1 COMPLEX REAL CALCULUS

In many fields of engineering, including the field of coherent diffractive imaging, Complex-Real (CR) or Wirtinger [97] derivatives are used for calculating complex derivatives for optimisation algorithms, often without explicitly stating so. The traditional definition of the derivative of a complex function $f(x)$ is only uniquely defined if the value of the limit that defines the derivative, which is given by

$$\frac{d(f(x))}{dx} = \lim_{h \rightarrow 0} \frac{f(x+h) - f(x)}{h}, \quad (82)$$

does not depend on from which direction it approaches zero in the complex plane. This only holds if the complex function satisfies the Cauchy-Riemann equations. This condition is not satisfied by many basic complex functions [96]. However, in CR-calculus a derivative is defined that is suitable for complex functions that do not satisfy these conditions by treating the real and imaginary parts of a function as mutually independent real-valued functions. The CR derivative is then defined as the sum of the (real-valued) partial derivatives to these parts. For a complex function f that is a function of its real and imaginary parts Re and Im ,

$$f(x, y) = \text{Re}(x, y) + i\text{Im}(x, y), \quad (83)$$

the CR-derivative can be defined by the following expression (following the convention advocated by Kreutz and Delgado [96]),

$$\left(\frac{\delta}{\delta f}\right)_{\text{CR}} = \frac{1}{2} \left(\left(\frac{\delta}{\delta \text{Re}(x, y)}\right) - i \left(\frac{\delta}{\delta \text{Im}(x, y)}\right) \right). \quad (84)$$

CR derivatives have the convenient property that the conjugate function is, by definition, a fixed point for the derivative to the function itself, which can simplify calculating the derivatives of absolute valued functions (such as vector norms), as complicated chain rules are avoided.

$$\left(\frac{\delta}{\delta f^*}\right)_{\text{CR}} = \frac{1}{2} \left(\left(\frac{\delta}{\delta \text{Re}(f)}\right) + i \left(\frac{\delta}{\delta \text{Im}(f)}\right) \right) \quad (85)$$

$$\left(\frac{\delta}{\delta f}\right)_{\text{CR}} f^* = \left(\frac{\delta}{\delta f^*}\right)_{\text{CR}} f = 0 \quad (86)$$

Note that the definition of the CR-derivative is not unique, as it depends on whether you consider the positive or negative direction for i to be larger.

The alternative convention, in which more positive i are considered to be larger, this convention is common in many area's of engineering and is given by,

$$\left(\frac{\partial}{\partial f}\right)_{\text{alt}_c\mathbb{R}} = \frac{1}{2} \left(\left(\frac{\partial}{\partial \text{Re}(x,y)}\right) + i \left(\frac{\partial}{\partial \text{Im}(x,y)}\right) \right). \quad (87)$$

However, the complex-real derivative in this definition does not revert to the real-valued derivative for real-valued functions, as in this definition, the complex-real derivative of a function to itself is zero.

SUPPLEMENTARY MATERIAL FOR CHAPTER 7 (APIE)

B.1 DERIVATION OF THE INVERSE TRANSFORMATION

Starting from the forward transformation $\mathbf{T}(x, y) = (u, v)$ of Eq. 77 in the main text, which maps detector space coordinates (x, y) to spatial frequencies (u, v) of the object, we derive the inverse transformation $\mathbf{T}^{-1}(u, v) = (x, y)$. Spatial frequencies associated with x are given by (see Eq. 77 of the main text)

$$u = \frac{x \cos(\theta)}{\lambda r_0} + \frac{\sin(\theta)}{\lambda} \left[\left(1 - \frac{x^2 + y^2}{r_0^2} \right)^{1/2} - 1 \right] \quad (88)$$

$$= \frac{x \cos(\theta)}{\lambda r_0} + \frac{\sin(\theta)}{\lambda} \left(\frac{z}{r_0} - 1 \right) \quad (89)$$

$$= \frac{x \cos(\theta)}{\lambda r_0} + \frac{\sin(\theta)}{\lambda r_0} (z - r_0), \quad (90)$$

and spatial frequencies associated with y are given by

$$v = \frac{y}{\lambda r_0}. \quad (91)$$

We can use Eq. 91 to get an expression for r_0 , which can then be substituted into Eq. 90 in order to eliminate the dependencies on $r_0(x, y)$,

$$r_0 = \frac{y}{\lambda v} \quad (92)$$

$$u = \frac{v}{y} \left[x \cos(\theta) + \sin(\theta) \left(z - \frac{y}{\lambda v} \right) \right]. \quad (93)$$

The x coordinate can be eliminated from Eq. 93 in the following way,

$$r_0^2 = \left(\frac{y}{\lambda v} \right)^2 = x^2 + y^2 + z^2 \quad (94)$$

$$x = \pm \left[\left(\frac{y}{\lambda v} \right)^2 - y^2 - z^2 \right]^{1/2} \quad (95)$$

$$u = \frac{v}{y} \left[\pm \left[\left(\frac{y}{\lambda v} \right)^2 - y^2 - z^2 \right]^{1/2} \cos(\theta) + \sin(\theta) \left(z - \frac{y}{\lambda v} \right) \right]. \quad (96)$$

Then, Eq. 94 is rearranged to isolate the root term,

$$\frac{uy}{\cos(\theta)v} = \pm \left[\left(\frac{y}{\lambda v} \right)^2 - y^2 - z^2 \right]^{1/2} + \frac{\sin(\theta)}{\cos(\theta)} \left(z - \frac{y}{\lambda v} \right), \quad (97)$$

$$\pm \left[\left(\frac{y}{\lambda v} \right)^2 - y^2 - z^2 \right]^{1/2} = \frac{uy}{v \cos(\theta)} - \frac{\sin(\theta)}{\cos(\theta)} \left(z - \frac{y}{\lambda v} \right). \quad (98)$$

After taking the square of both sides, these terms can be reordered as a quadratic polynomial in y :

$$y^2 \left[1 - \left(\frac{1}{\lambda v} \right)^2 + \left(\frac{u}{v \cos(\theta)} \right)^2 + \left(\frac{\sin(\theta)}{\lambda v \cos(\theta)} \right)^2 + 2 \frac{u \sin(\theta)}{\lambda v^2 \cos^2(\theta)} \right] + y \left[\frac{-2z \sin(\theta)}{v \cos^2(\theta)} \left(\frac{\sin(\theta)}{\lambda} + u \right) \right] + z^2 (1 + \tan^2(\theta)) = 0. \quad (99)$$

Next, we multiply both sides of Eq. 99 with $v^2 \cos^2(\theta)$,

$$y^2 \left[\cos^2(\theta) v^2 + \frac{-\cos(2\theta)}{\lambda^2} + u^2 + 2 \frac{u \sin(\theta)}{\lambda} \right] + y \left[-2vz \sin(\theta) \left(\frac{\sin(\theta)}{\lambda} + u \right) \right] + v^2 z^2 = 0. \quad (100)$$

From here, the standard quadratic formula is used to solve for y ,

$$y = \frac{-b \pm [b^2 - 4ac]^{1/2}}{2a}, \quad (101)$$

where,

$$a = \cos^2(\theta) v^2 - \frac{\cos(2\theta)}{\lambda^2} + u^2 + 2 \sin(\theta) \frac{u}{\lambda} \quad (102)$$

$$b = -2vz \sin(\theta) \left(\frac{\sin(\theta)}{\lambda} + u \right) = b_0 v \quad (103)$$

$$c = v^2 z^2, \quad (104)$$

in which $b_0 = b/v$ is a parameter that is introduced for compactness of the final expression. From here, Eq. 101 can be rewritten into the following expression for y ,

$$y = \frac{-b_0 v \pm |v| [b_0^2 - 4az^2]^{1/2}}{2a}. \quad (105)$$

Next, the correct sign of the root term of this solution needs to be determined. From the forward transformation Eq. 91, we see that the sign of v and y should be the same, as λr_0 is positive. This leads to the following constraint on the signs:

$$\text{sign}(y) = \text{sign} \left(\frac{-b_0 v \pm |v| [b_0^2 - 4az^2]^{1/2}}{2a} \right) = \text{sign}(v) \quad (106)$$

Thus, the sign of the numerator times that of the denominator in Eq. 106 must be identical to the sign of v . In the case that $a < 0$, the two terms in the square root add up. The magnitude of the square root term then becomes larger than b_0v , and determines the sign of the numerator. To match the sign of v , we must choose the \pm sign in Eq. 106 opposite to $\text{sign}(v)$.

For $a > 0$, the terms in the square root are subtracted, and the sign of the numerator is determined by the $-b_0v$ term. This in principle leaves the choice of the \pm sign undetermined. In this case, additional insight can be gained by considering the limit $a \rightarrow 0$, which may occur for specific parameter combinations. For y to remain finite, the numerator in Eq. 106 should then also go to zero, which can only be ensured in the general case if $-b_0v \pm |b_0v| = 0$. From Eq. 103 it can be seen that b_0 can only become positive when $u < -\sin(\theta)/\lambda$. In the regime where the paraxial approximation is valid, $1/\lambda \gg u, v$. Thus, b_0 can only become positive for very small values of θ . Note that $\sin(\theta) > 0$, as the measurement geometry restricts θ to values between 0 and 90 degrees. For such small angles, a is negative as the $-\cos(2\theta)/\lambda^2$ term dominates Eq. 102. Therefore, in the limit of $a \rightarrow 0$, b_0 is negative and we obtain the same sign choice as above.

The remaining case is that of $b_0 < 0$ and $a > 0$.

Assuming that the solution should be continuously connected to the case described above for $a \rightarrow 0$, the sign choice should remain such that $-b_0v \pm |b_0v| = 0$, and consequently the sign choice should again be $-\text{sign}(v)$.

Thus, we conclude that the sign choice is the same in all cases, and we can incorporate it in the expression Eq. 105 through the $|v|$ -term, resulting in the final expression for y :

$$y = v \frac{-b_0 - [b_0^2 - 4az^2]^{1/2}}{2a}. \quad (107)$$

B.2 ENSURING NUMERICAL ACCURACY

When evaluating Eq. 107 numerically, it is important to realize the critical sensitivity in the ABC-formula to rounding errors when $4ac \ll b$, in which case the numerator contains a subtraction of two large numbers of nearly equal magnitude. We therefore follow the approach suggested in [168] to rewrite Eq. 107 into an expression that avoids such numerical instabilities:

$$y = \frac{-2vz^2}{b_0 - [b_0^2 - 4az^2]^{1/2}} \quad (108)$$

Finally, an expression for x as a function of u , v and y is obtained by rearranging Eq. 93:

$$x = \frac{y}{v} \frac{\lambda u + \sin(\theta)}{\lambda \cos(\theta)} - z \tan(\theta). \quad (109)$$

The inverse transformation for both coordinates is now given by Eqs. 108 and 109

B.3 ILLUSTRATION OF MAPPING PROCEDURES

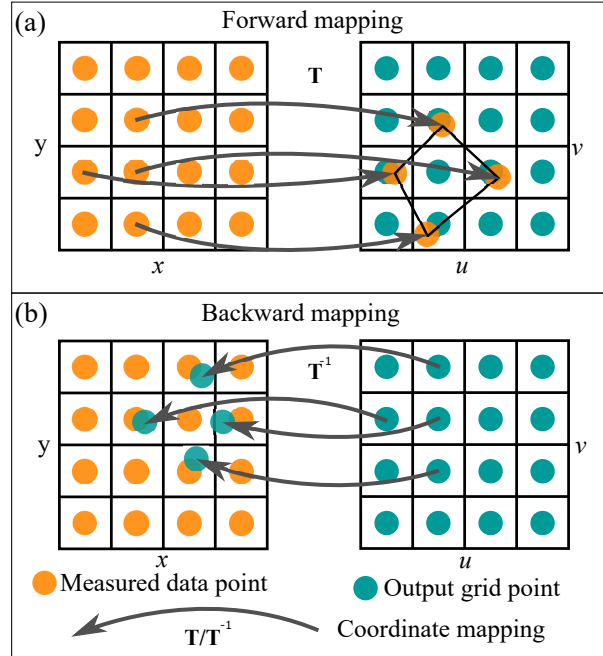


Figure 36: Illustration of the mapping procedures discussed in the main article, (a) forward mapping, the detector space grid (orange) is transformed to a warped spatial frequency space grid through a forward transformation $(x, y) \rightarrow T(x, y)_{\text{regular}} = (u, v)_{\text{warped}}$. The intensities on a uniformly spaced (u, v) output grid (cyan) are found through interpolation from the warped spatial frequency grid that results from the previous operation. (b) Backward mapping, The inverse transformation $(x, y) \rightarrow T^{-1}(u, v)_{\text{regular}} = (x, y)_{\text{warped}}$ is applied to a uniform grid in spatial frequency space to find the associated coordinates in detector space. Then the intensities in those detector space points are approximated through interpolation from the values measured on the regular detector grid. These interpolated intensity values are copied to the corresponding u, v grid points.

B.4 ERROR CONVERGENCE WITH AND WITHOUT TILT-ANGLE REFINEMENT

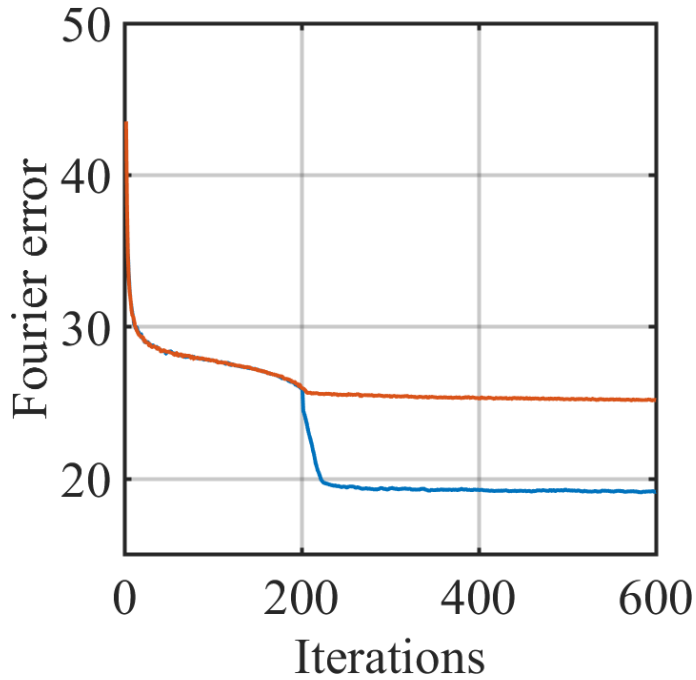


Figure 37: Comparison of the error convergence (as defined in Eq. 6 in the main article) between a reconstruction with ePIE (orange) that is tilt-corrected at a fixed tilt angle estimate of 45° , and a reconstruction in which the tilt-angle is calibrated with aPIE (blue). The aPIE algorithm is initiated after 200 iterations of ePIE. In this calibration, the estimate is refined from an initial tilt angle estimate of 45° to a final estimate of 43.3° . These reconstructions start from identical initial estimates for both the probe and the object. The dataset for these reconstructions was recorded with a structured beam.